SPECTRAL AND SPATIAL ANOMALIES IN WHITE-LIGHT INTERFEROMETRY

A Thesis Submitted for the Degree of

DOCTOR OF PHILOSOPHY

By

MARUTHI MANOJ BRUNDAVANAM

School of Physics

University of Hyderabad

Hyderabad - 500 046

India

March 2010

To my parents

and brother

DECLARATION

I here by declare that the matter embodied in the thesis entitled "**Spectral and spatial anomalies in white-light interferometry**" is the result of investigation carried out by me in the School of Physics, University of Hyderabad, India, under direct supervision of Prof. D. Narayana Rao.

Place: Hyderabad
Date: 31-03-2010

(B. Maruthi Manoj)

To my parents

and brother

DECLARATION

I here by declare that the matter embodied in the thesis entitled "**Spectral and spatial anomalies in white-light interferometry**" is the result of investigation carried out by me in the School of Physics, University of Hyderabad, India, under direct supervision of Prof. D. Narayana Rao.

Place: Hyderabad
Date: 31-03-2010

(B. Maruthi Manoj)

CERTIFICATE

This is to certify that the work described in this thesis entitled "**Spectral and spatial anomalies in white-light interferometry**" has been carried out by **Brundavanam Maruthi Manoj**, under my direct supervision and this has not been submitted for any degree or diploma at this or any other University.

Place: Hyderabad

Date: 31.03.2010

(Prof. D. Narayana Rao)

Dean

School of Physics

DEAN
School of Physics
University of Hyderabad
Hyderabad-500 046, INDIA

ACKNOWLEDGEMENTS

I am very grateful to my thesis supervisor, Prof. D. Narayana Rao, for giving me an opportunity to work in his group. I express my gratitude and profound thanks to him for his inspirational and though provoking guidance. I am indebted to him for teaching me how to think innovatively in setting up the experiments. His guidance goes even beyond science and helped me to grow as a strong individual.

I am very much thankful to Dr. Nirmal K. Viswanathan, for his patience and thought provoking discussions on the subject of singular optics. I have learnt the art of presenting the results in better way.

I wish to thank Dr. Suneel Singh for many discussions I had with him to clarify the fundamentals of optics. I wish to thank Prof. S. P. Tewari, Prof. S. Dutta Gupta and Dr. Anantha Lakshmi for their constant support and inspiring discussions. I also thank Dr. V. Ashok for teaching me how to work with Lab View.

I thank all my lab seniors, Dr. S. Venugopala Rao, Dr. Prem Kiran, Dr. Naga Srinivas, Dr. Manoj, Dr. G. Vijay Prakash, Dr. Bhakta, Dr. Chaitanya and Dr. Venkatram for encouraging and supporting me throughout my time here. Special thanks to Dr. Sai Santosh for encouraging and supporting me during my time with him. Thanks to my present lab members Dr. Satyavathi, Ali, Deepak, Balamurali Krishna, Sekhar, Praveen, Sriram and Sreeramulu for creating friendly and pleasant lab atmosphere. Without the support of these guys this thesis work wouldn't have been successful.

Special thanks to my friends Srinivas, Vijaya Lakshmi, Baba, Govardhan, Sudha Nirmala, V. Srinivas, Chalapathi, Suryanarayana, Ramakrishna, Mubeen and others for their encouragement and moral support during my thesis work.

Without the support and encouragement from my parents, grandparents and my brother this dream of mine would have remained so. With a deep sense of gratitude I must acknowledge my family members and relatives for their moral support and guidance.

Finally I would like to thank everybody who has helped me at different stages of my research carrier and my stay at the University of Hyderabad.

Table of Contents

CHAPTER 1

Abstract

A brief overview on the singular optics which has lead to the observed spectral and spatial anomalies is presented. The motivation for the current work is briefly discussed. A brief introduction to spectral interferometry and some elementary concepts of the coherence properties of the optical fields are also presented. Introduction to filamentation in optical media is given briefly which has lead to the formation of spatial anomalies. An overview of the thesis is presented at the end of the chapter.

Introduction

1.1 Overview on singular optics

Now a days there has been a considerable interest in the optical field structure in the vicinity of the zero intensity regions. This has become a new branch of modern physical optics named as *singular optics*. This new branch deals with a wide class of effects associated with phase singularities where the phase of the wave fields is indeterminate, as well as with the topology of wavefronts. Singular optics has been recognized as separate important branch of modern physics about fifteen years ago. Actually, along this period it has been developed as coherent singular optics. Fundamental properties of phase singularities and the most important regularities governing the formation of singularities of the field (such as sign principles) have been established both for scalar (uniformly polarized) and for vector (spatially non-uniformly polarized) monochromatic optical fields. Development of coherent singular optics continues. The most interesting and promising event of the last few years, especially since 2002, consists in the tendency to expand the singular optical principles on the field of partially coherent light fields. In this context, physically new singular optical concepts are derived, new experimental instrumentation is developed, and new promising applications of the singular optical approaches are elucidated. Analysis of last achievements in the field of singular optics leads to the conclusion on coming into being of new branch of this area of investigation, which can be referred to as the correlation singular optics. It is remarkable that fruitfulness of this new R&D direction is essentially determined by the concepts and results of classical wave optics, which were developed irrespective of the singular optical paradigm.

Phase of a wave gives visual perception of wave propagation and transformation along its path. An important relevant conception to singular optics is wave front, or surface of equal phase, usually associated with a crest of a wave, where the field strength attains its highest value. The wave fronts follow each other with spatial separation of one wavelength, and between two neighboring

wave fronts there are two surfaces where the field strength becomes zero, and one surface where the field reaches minimum (negative) value (trough). This perfect regular motion, being true for a plan wave can some times be violated for real waves. In brief, phase of a wave can experience a "π-jump", corresponding to a step on half of a wavelength in a wave train, producing a phase defect of a wave front along a continuous line in space. Some physical reasons can be responsible for local retardation or acceleration of the phase velocity across a wave front, resulting wavefront bending leadings to a tear of the wavefront, and the phase becomes indeterminate, or singular along the tear. The necessary condition for a phase singularity to appear is the vanishing of the field amplitude.

In this section, we briefly discuss different singular optical effects observed due to different fields.

1.1.1 Coherent singular optics

The development of singular optics has been exclusively performed under approximation of completely coherent optical field [1, 2]. For that, phase singularities have been associated with the complex amplitude of a monochromatic field alone. It has been clear only recently that any (arbitrary) complex parameter of an optical field can be singular [3, 4]. Singular optics operates with phase parameters of correlation functions, polarization parameters and spectral components of the field. Adequate description of phase singularities has been given already [1] where the singularities that are possible in scalar fields are classified into screw dislocations (vortices), edge and mixed (edge-screw) dislocations, as well as singularities kind of non-localized dark interference fringe. Wavefront dislocations are generally curvilinear singularities. The main (and unique) experimental technique for revealing and diagnosis of phase dislocations in coherent singular optics is the interferometric technique [5]. In this technique, an off-axis interference of the vortex-supporting wave with the reference wave is introduced to detect the optical vortices. Typical bifurcation of an interference fringe (forklet) occurs in the vicinity of amplitude zero. The direction of forklet enables determination of twirling of a phase helicoids

(clockwise or counterclockwise), if one knows the direction of propagation of reference wave.

1.1.2 Singular optics on polychrome-diffraction induced spectral shifts

On the other hand, new direction in development of singular optics is considerably extending its framework in connection with the study of the induced spectral shifts (Wolf's spectral effect [6, 7]) in polychromatic radiation as the singular optic effect. These spectral shifts are produced by the correlation properties of the fluctuating source [6]. The spectral characteristics in the near zone when a certain class of partially coherent light is incident on a circular aperture are also studied [8]. Later, remarkable spectral changes taking place in the neighborhood of phase singularities near the focus of a converging spherical wave [9] are shown as singular optical effect. Understanding this structure may be relevant to fluorescence microscopy, in which exciting field can have a spectrum that varies strongly in the volume that is probed, leading to a high resolution. These spectral changes will also take place in the neighborhood of phase singularities in other kinds of fields [10, 11]. Some of these theoretical predictions are also verified experimentally [12]. Spectral anomalies such as spectral shifts and spectral switches also take place in the interference field, both in the near field and in the far field, when the double-slit is illuminated by polychromatic completely coherent light or polychromatic partially coherent light [13, 14]. Using interference measurements of a polychromatic partially coherent light source, the existence of a temporal correlation vortex (TCV) is verified experimentally and it is observed that the TCV becomes unstable when the effective topological charge is varied across the spectrum [15].

The spectral anomalies observed in the focal plane of apertured beams are of different nature compared to those inherent to ultra-broadband radiation. Moreover, the appearance of multiple bandgaps in the diffracted field is responsible for the cease in the spectral switch effect with increasing bandwidth [16]. The temporal coherence length, spatial correlation parameter and diffraction

angle strongly affects the spectral shifts and spectral switches of spatially and spectrally partial coherent pulsed beams in Young's interference experiment [17]. The spectral anomalies such as spectral shifts and spectral switches around the phase singularities due to the diffraction of partially coherent polychromatic light (white-light) source described in the above studies have been using the spectrum of white-light in the frequency (or wavelength) domain. Whereas the visualization of such phase singularities present in the diffraction pattern due to white-light source are explained by Berry [18, 19].

All the above mentioned studies are based on diffraction-induced or spatial coherence induced spectral anomalies using partially coherent polychromatic radiation. The main analytical instrument for investigation of diffraction-induced spectral changes is so called 'spectral modifier' [9]. Spectral modifier is associated with any (integral) diffraction equation always including the ratio of the radius of a diffraction aperture and the wavelength of the probing radiation. Spectral modifier is the function of both temporal frequency and spatial coordinates. As the amplitude zeros are not coinciding in space for different spectral components of polychromatic radiation, the resulting spectrum is found as the product of the initial spectrum and the spectral modifier. This results in the observation of drastic changes of the initial spectrum at points or lines where the magnitude of the spectral modifier vanishes for any spectral component or in other words where the spectral modifier undergoes phase singularity for given temporal frequency.

1.1.3 Singular optics on scattering induced spectral shifts

When a polychromatic light impinges onto a colorless rough surface comparable with the wavelength of any spectral component of the probing radiation, the scattered radiation (zero diffraction order) occurs to be colored. These spectral changes in the polychromatic radiation that is caused by singularities of quite different nature, which can be referred as the singularities of spectral strength of scattering of rough surface [3]. The principles and the practical conditions for registration of phase singularities, such as optical vortices in the spectral

components of white-light speckle-field, and their diagnosis are reported [20-23]. These phase singularities present in the complex analytical signal of a speckle pattern are used to measure the displacements [24, 25].

1.1.4 Nonlinear singular optics

The large group of interesting effects with singular-beam self-action in nonlinear media is based on the refractive index dependence on the light intensity determined by the material third-order nonlinearity ($\chi^{(3)}$). As a result the laser beam can self-focus, self-defocus, self-guide and form solitary waves. Experimental observations [26] and theory of singular beam propagation in a self-focusing medium with saturated nonlinearity [27] demonstrate the break up of the singular beam into separate bright solitary waves after reaching the instability threshold.

The natural birth of the phase singularities on a smooth wavefront of an ordinary coherent beam via its self-action in $LiNbO_3$: Fe crystal due to the anisotropy of the crystal electro-optic tensor is observed experimentally [28]. Optical singularities are also observed using a SBN: Cr (strontium-barium niobate) crystal whose refractive index increases with temperature resulting in the self-focusing of the input laser beam [29]. The physical mechanism of the observed optical singularities in a laser beam passed through nonlinear media is explained using the self-induced refractive index variation by a thin astigmatic Gaussian lens or an equivalent phase transparent lens [30].The main effect is the loss of the inherent self-similarity of the Gaussian beam after this lens, due to the phase modulation of the wave front by the lens. Recently, it has been shown that same scenario of the origin and evolution of optical singularities is also valid for laser beam self-action inside a Kerr-like defocusing medium [31].

1.2 Motivation

The spectral and spatial anomalies studied in the above subsections are all based on either diffraction induced effects or spatial coherence induced effects using monochromatic and polychromatic light radiation. The practical applications

using the above studies are limited due to complexity involved in them to make the system compact. In order to make the system compact and good signal to noise ratio of the measurements we demonstrate the temporal coherence induced spectral anomalies such as spectral shifts and spectral switches using a Michelson interferometer illuminated by a polychromatic light operated in the spectral domain (spectral interference) [32]. These temporal coherence induced spectral anomalies are used to measure the nano-scale displacements using the spectral shifts around the spectral switch position [33]. The effect of input source spectral characteristics on these spectral shifts and spectral switches are studied experimentally [34]. The spatial anomalies (forklets) present in the far-field spatial emission pattern due to nonlinearities of the material and the spectral interference of the white-light continuum generated during the formation of the filaments in BK7 glass using a femtosecond laser pulses are also presented [35].

1.3 Spectral interferometry

Coherence-induced spectral changes [36] predicted by Wolf increased the interest in studying the phenomenon of the spectral changes and the formation of spectral interference fringes in the framework of optical coherence theory [37]. The spectrum of the interfering fields is affected by the coherence properties of the optical field. The spectral modulations observed in the spectrum depend on the spectral bandwidth of the light source and the change in the degree of spectral coherence between the interfering fields. The spectral changes thus observed can be used to study the field cross-correlation [38], path difference between the interfering beams [39], size of the source [40] and the intensity distribution across it [41]. The affect of degree of coherence in the space-frequency domain and its applications are investigated thoroughly using spectral interference [42].

Spectral interferometry using a broadband white-light source is a potential technique to overcome the most of the difficulties such as phase ambiguities which limit the test surface height measurement to half the wavelength of the monochromatic source [43]. The white-light sources are cheap, efficient and can give an illumination which is free of speckle noise. In optical information

processing, white-light interferometer has potential applications due to achromatic interference effects [44, 45]. The main advantage of the spectral interferometry is that the whole spectrogram can be recorded in a single shot using a dispersion element like a prism or a grating and a CCD array detector. As most of the information is stored in the periodicity of the fringes and not in their contrast, small vibrations do not invalidate the information. This spectral interference phenomenon can be applied to the synthetic aperture imaging technique [46], using the space-frequency equivalence theorem [47]. Spectral interferometry has been applied to the measurement of the spectral phase introduced by optical fibers [48], absolute distance [49], simultaneous measurement of the refractive index and thickness of the transparent materials [50] and high resolution profilometry [51].

Spectral-domain OCT [52], also known as Fourier-domain OCT, based on spectral interference, carried out using a broadband superluminescent diode has become a promising technology due to its practical use in obtaining sample images with ultra-high resolution and at higher speeds than possible with conventional time-domain OCT [53, 54]. This spectral interferometry has also been extended to determination of direct electric field reconstruction of ultrashort pulses [55-57]. Recently, spectral interferometry has been used for the complete space-time characterization of few-cycle near-infrared femtosecond pulses and extreme ultraviolet (XUV) attosecond pulses produced via high harmonic generation (HHG) [58].

1.4. Some elementary concepts of coherence:

(a) Analytical signal representation:

The electromagnetic field can be represented by a complex quantity in coherence theory due to its mathematical simplicity [59]. The complex representation of real polychromatic field is a natural generalization of the complex representation of monochromatic fields used in the classical optics. The real part of the field amplitude for a typical monochromatic component of the field is given by

$$\varepsilon^{(r)}(r,v) = \varepsilon_0(r)\cos[\phi(r) - 2\pi vt] \tag{1.1}$$

where $\varepsilon_0(r)$ is the magnitude of the field and $\phi(r)$ is the phase. For the ease of manipulation, it is conventional to work with the complex field amplitude of the type

$$\varepsilon(r,v) = \varepsilon_0(r)\exp[i\phi(r)] \tag{1.2}$$

The time dependent complex analytical signal can be obtained using Fourier transform of Eq. (1.2), i.e.

$$\varepsilon(r,t) = \int_0^{\infty} \varepsilon(r,v)\exp(-2\pi vt)dv \tag{1.3}$$

The real part of the analytical signal gives the actual field component.

(b) Intensity, I(r, t):

Intensity is usually considered an observable quantity and is defined in coherence theory as the time averaged square magnitude of the analytical signal (Eq. (1.3)).

$$I(r,t) = \lim_{T\to\infty} \frac{1}{2T} \int_{-T}^{+T} \varepsilon^*(r,t)\varepsilon(r,t)dt \tag{1.4}$$

If the analytical signal is assumed to be an ergodic random process, the above equation can also be written in terms of ensemble averages of the form

$$I(r,t) = \left\langle \varepsilon^*(r,t)\varepsilon(r,t) \right\rangle \tag{1.5}$$

This averaged field intensity at point 'r' is useful in normalizing the mutual coherence function which will be defined in the following subsection, 1.2 (e).

(c) Temporal coherence and coherence time (τ_c):

Temporal coherence is the measure of the average correlation of the fluctuations of an optical field at a point in space for any pair of times. The temporal coherence can be explained using a Michelson interferometer. A beam of light from a small quasi-monochromatic source σ, divided into two beams in a Michelson interferometer (Fig. 1.1) and these two beams are then recombined at the same beam splitter after introducing a path difference Δl = cτ (c is the

velocity of light in vacuum). For a sufficiently small path difference Δl, interference fringes are formed in the observation plane $\mathscr{P}$. These fringes are manifestation of the temporal coherence between the two interfering beams. The ability of the two beams to form fringes can be explained using the concept of correlation that exists between the fluctuations of the two beams reaching $\mathscr{P}$ as a function of time delay τ introduced between them [60]. Interference fringes will be observed only if

$$\tau_c \, \Delta\nu \leq 1 \tag{1.6}$$

and hence the limiting time delay given by $\tau_c \approx 1/\Delta\nu$ is known as the *coherence time* of the light and the corresponding path length

$$l_c = c\tau_c = c/\Delta\nu \tag{1.7}$$

is called the *coherence length* or more precisely termed as *longitudinal coherence length*. Here $\nu = c/\lambda$, where λ is the wavelength, the coherence length may be written as $l_c \approx \lambda_0^2/\Delta\lambda$, where λ_0 is the mean wavelength and $\Delta\lambda$ is the full width at half maximum spectral bandwidth.

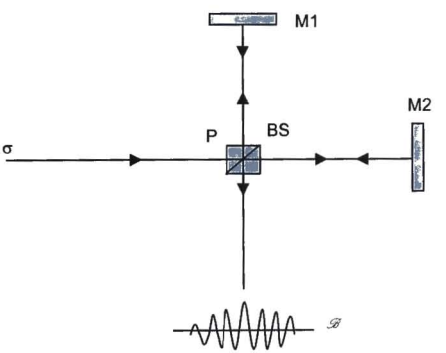

Figure 1.1: *Michelson interferometer. BS: cubic beam splitter, σ · source; M_1&M_2 mirrors; $\mathscr{P}$ observation plane*

(d) Spatial coherence and coherence area, ΔA:

Spatial coherence is the measure of the average correlation of the fluctuations of an optical field for any pair of points in space at a particular time. In order to explain this, consider the Young's interference experiment with a quasi-

monochromatic light from an extended source σ (Fig. 1.2). The source is with square sides δa and the pinholes P_1 and P_2 sufficiently close to the symmetric axis. The resultant interference fringes are observed on the screen $\mathscr{B}$ near the axial point P. The appearance of these fringes is manifested due to the spatial coherence existing between the beams reaching the screen $\mathscr{B}$ from P_1 and P_2 Since the visibility of the interference fringes depends on the spatial separation of the pinholes and can be explained as arising from the correlation that exists between them. Interference fringes are generally observable only if

$$(\delta\theta)(\delta a) \leq \lambda_0 \tag{1.8}$$

where δθ is the angle that the distance P_1P_2 between the pinholes subtends at the source and λ_0 is the mean wavelength of the light. If 'r' is the distance between the source plane and the plane containing the pinholes $\mathscr{A}$ to observe the fringes near P, the pinholes must be situated within an area around their midpoint of size

$$\Delta A \approx (r\,\delta\theta)^2 \approx (r\,\lambda_0/\delta a)^2 \tag{1.9}$$

This region is called the coherence area of the light in the plane of the pinholes around their midpoint. The square root of the coherence area is also known as the *transverse coherence length*. The formation of the interference fringes at the observation plane $\mathscr{B}$ can be explained as due to the addition of the intensities of the individual interference patterns produced by different mutually independent point sources. A deeper understanding of this phenomenon is possible in terms of the concept of correlation [60], which sums up to the fact that even statistically independent sources will give rise to correlation in the fields that are generated in the process of propagation and super position.

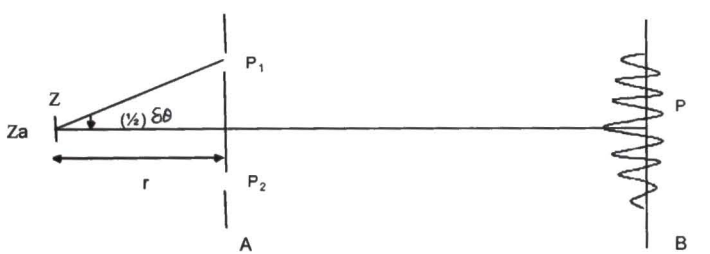

Figure 1.2: *Young's double slit experiment. σ: source, P_1 and P_2: pinholes, $\mathscr{A}$: plane of double slit; $\mathscr{B}$: plane of observation*

(e) Mutual coherence function, $\Gamma(r_1, r_2, \tau)$:

The mutual coherence function is a central quantity in the elementary theory of optical coherence and gives cross-correlation between the light vibrations at two space-time points (r_1,t_1) and (r_2,t_2) [61]. This mutual coherence function is defined by

$$\Gamma(r_1,r_2,\tau) = \lim_{T\to\infty} \frac{1}{2T} \int \varepsilon^*(r_1,t)\varepsilon(r_2,t+\tau)dt \tag{1.10}$$

The correlation function depends on the two time arguments only through their difference $\tau = t_2-t_1$ and $\varepsilon(r,t)$, the complex analytical time dependent signal at some point 'r' and time 't' defined in Eq. (1.3). For ergodic and stationary fields Eq. (1.10) becomes

$$\Gamma_{12}(\tau) = \left\langle \varepsilon^*(r_1,t)\varepsilon(r_2,t+\tau) \right\rangle \tag{1.11}$$

The intensity of the field at point 'r' can also be written in terms of the mutual coherence function, i.e.

$$I(r,t) = \lim_{T\to\infty} \frac{1}{2T} \int_{-T}^{T} \varepsilon^*(r,t)\varepsilon(r,t)dt = \Gamma_{11}(0) \tag{1.12}$$

(f) Cross-spectral density function, $W(r_1, r_2, \nu)$:

The ensemble averaged correlation function between typical monochromatic components of the field disturbance at a point r_1 with the complex conjugate of the same component at some other point r_2 at frequency ν gives the cross spectral density or the cross power spectrum and is defined by

$$\left\langle \varepsilon^*(r_1,\nu)\varepsilon(r_2,\nu') \right\rangle = W(r_1,r_2,\nu)\delta(\nu-\nu') \tag{1.13}$$

where δ is the Dirac delta function and the ensemble average is taken over the different realization of the fields. The field amplitude $\varepsilon(r,\nu)$ is taken to be a random variable of arbitrary coherence. According to the generalized Wiener-Khintchine theorem, the two correlation functions, the mutual coherence function and cross-spectral density function form a Fourier transform pair i.e.

$$\Gamma(r_1,r_2,t) = \int_0^\infty W(r_1,r_2,\nu)\exp(-2\pi i\nu\tau)d\nu \tag{1.14}$$

$$W(r_1,r_2,\nu)=\int_{-\infty}^{+\infty}\Gamma(r_1,r_2,\tau)\exp(2\pi i\nu\tau)d\tau \tag{1.15}$$

The cross-spectral density function is Hermitian in the sense that $W(r_1, r_2,\nu) = W^*(r_1, r_2, \nu)$ and is non-negative and definite.

(g) Spectrum, S(r,ν) and normalized spectrum, s(r,ν):

When the two points r_1 and r_2 coincide, the cross spectral density function given by Eq. (1.13) reduces to a function which depends only on the location of one point 'r' and on the frequency ν. This function is known as the spectral density or the power spectrum of light which is the trace of the cross-spectral density function and is defined as

$$S(r,\nu)=\left\langle \varepsilon^*(r,\nu)\varepsilon(r,\nu)\right\rangle = W(r,r,\nu) \tag{1.16}$$

The power spectrum can be normalized according to the equation

$$s(r,\nu)=\frac{S(r,\nu)}{\int_0^{\infty}S(r,\nu)d\nu} \tag{1.17}$$

and the normalized spectrum has the property $\int_0^{\infty}s(r,\nu)d\nu=1$, which is independent of the total intensity. However, the intensity of the spectrum is equivalent to the intensity of a single monochromatic component of the field defined by Eq. (1.5). Since different monochromatic components of the field are mutually incoherent and can not interfere, the intensity of the total field is calculated as the sum of intensities of all the monochromatic components, i.e.

$$I(r,\nu)=\int_0^{\infty}S(r,\nu)d\nu \tag{1.18}$$

(h) Complex degree of spectral coherence, μ (r_1, r_2, ν):

As the cross-spectral density function contains information about both the spectrum and the coherence of the field, a new function that depends only on the

coherence properties of the field is introduced known as complex degree of spectral coherence and is defined as [62]

$$\mu(r_1,r_2,\nu)=\frac{W(r_1,r_2,\nu)}{\sqrt{W(r_1,r_1,\nu)W(r_2,r_2,\nu)}}=\frac{W(r_1,r_2,\nu)}{\sqrt{S(r_1,\nu)S(r_2,\nu)}} \tag{1.19}$$

where S(r,ν) is the spectral density or the power spectrum of the light. μ (r_1, r_2,ν) is referred to as the spectral degree of coherence at frequency, ν of the light at two different points r_1 and r_2. It is also known as the complex degree of spatial (or spectral) coherence at frequency ν [63, 64]. It should also satisfy the inequality

$$0\le|\mu(r_1,r_2,\nu)|\le 1 \tag{1.20}$$

for all values of the arguments r_1, r_2, ν. If the magnitude of the complex degree of spectral coherence is zero, the field amplitudes at two points are completely incoherent and if it is unity, the monochromatic field components of frequency ν are perfectly coherent between the points. If magnitude of this function is less than unity, it indicates less than perfect coherence. As can be seen this function depends only on the positions of the points and the single frequency ν that the field components at the two points share. Field components of different frequency are always uncorrelated, even at the same point.

1.5. Introduction to filamentation in optical media

When a powerful femtosecond laser pulse propagates in an optical medium, the primary process that occurs is self focusing. Normally, it is the most powerful part (slice) of the pulse that self-focuses first during its propagation. It is balanced by the self generated plasma in the self-focal volume which defocuses the pulse. This dynamic balance between self-focusing and self-defocusing leads to the formation of 'filament' and limitation of the peak intensity (intensity clamping) in the self-focal volume. The series of self-foci from different slices of the front part of the pulse undergoes self-phase modulation and self-steepening resulting in a strong spectral broadening. The final pulse is a white-light laser pulse (supercontinuum).

Fundamentally, the physics of filamentation is based upon Kerr self-focusing. The phenomenon of Kerr self-focusing dates back to the 60s [65, 66]; filamentation and spectral (red) broadening have been observed by Reintjes et al. [67] while the limitation of the laser intensity at the self-focus (intensity clamping) in glass has been proposed already [68]. So, what is really new now that makes it so interesting? It is the femtosecond laser pulse, being very short and powerful that makes a huge difference. Optical breakdown (a collision process) resulting in the total ionization of the interaction zone in the medium [69] could not be induced to its completion by such short pulses (nanosecond down to picoseconds) masked many interesting filamentation phenomenon which were not even foreseen at that time. Now a days powerful femtosecond laser pulses can self-focus and propagate over a long distance in air in the form of an apparent long filament [70]. This phenomenon encompasses what is more recently known as supercontinuum generation [71]. The supercontinuum is a broad spectrum extending from the near UV (~350 nm) to the infrared (~4 microns). The spectral width depends on the ionization potential (gases) or the band gap energy (condensed matter). The main aspects of ultrashort filamentation in various optical media, their properties and their applications are reviewed recently [72].

1.6 Organization of the thesis

Chapter 2 involves the study of spectral shifts and spectral switches due to temporal correlation of the input beam using a white-light Michelson interferometer operated in the spectral domain. An unusual behavior in the number of spectral fringes observed within the spectral bandwidth of the source as a function of optical path difference within the coherence length of the source is presented.

Chapter 3 shows the experimental demonstration of the measurement of nano-scale displacements using the spectral shifts around and crossing through the spectral switch. We propose two methods to measure the nano displacements and

the results are compared to investigate the higher sensitivity of the proposed methods.

Chapter 4 is dedicated to study the effect of the spectral characteristics such as spectral bandwidth, peak wavelength and symmetry of the input spectrum on the spectral switch characteristics such as spectral switch position, spectral switch amplitude and its symmetry. In order to see the combined effect of the spectral characteristics, we study the effect of fractional bandwidth on the spectral switch amplitude and symmetry of the spectral switch.

Chapter 5 presents the experimental demonstration of the formation of filaments in BK7 glass due to femtosecond laser pulses. The spectral modulations observed in the output transmission spectrum are recorded as a function of the input laser power and studied the temporal separation of the refocused filaments formed in the glass sample. The spatial anomalies (forklets) in the far-field spatial emission pattern are observed due to the shear in one of the wavefronts of the multiple filaments. A simple model using geometrical calculations and interference is proposed to demonstrate the spatial anomalies observed.

Chapter 6 summarizes the results obtained in this dissertation work and future implications and directions are discussed in brief.

References

1. J. F. Nye and M. V. Berry, Proc. R. Soc. A **336**, 165 (1974).
2. M.S. Soskin and M.V. Vasnetsov, Prog. in Optics, ed. E. Wolf (Amsterdam: Elsevier) **42**, 219 (2001).
3. V. K. Polyanskii, O. V. Angelsky, P. V. Polyanskii, " Scattering-induced spectral shifts as the singular optical effect", Opt. Appl. **32**, 843 (2002).
4. G. V. Bogatyryova, Ch. V. Felde, P. V. Polyanskii, S. A. Ponomarenko, M. S. Soskin, E. Wolf, Opt. Lett. **28**, 878 (2003).
5. N. R. Baranova, B. Ya. Zel'dovich, A. V. Mamaev, N. F. Philipetskii, V. V. Shknov, Sov. Phys.. JETP, **56**,983 (1982).
6. E. Wolf, D. F. V. James, Rep. Prog. Phys. **59**, 721(1996).
7. I. V. Tatarskii, Pure Appl. Opt. **7**, 953 (1998).
8. J. Pu, H. Zhang and S. Nemoto, Opt. Commun. **162**, 57(1999); J. Pu and S. Nemoto, IEEE J. Quantum Electron. **34**, 1082(1998); J. Pu and S. Nemoto, J. Opt. Soc. Am. A **19**, 339 (2002).
9. G. Gbur, T. D. Visser and E. Wolf, Phy. Rev. Lett. **88**, 013901-1(2001).
10. G. Gbur, T. D. Visser and E. Wolf, J. Opt. Soc. Am. A **19**,1964 (2002).
11. J. T. Foley and E. Wolf, J. Opt. Soc. Am. A **19**, 2510 (2002).
12. G. Popescu and A. Dogariu, Phys. Rev. Lett., **88**, 183902-1 (2002).
13. J. Pu, C. Cai and S. Nemoto, Opt. Express **12**, 5131 (2004).
14. S. Anand and M. N. Kamalasanan, Opt. Commun. **266**, 469 (2006).
15. G. A. Swartzlander Jr., J. Schmit, Phys. Rev. Lett. **93**, 093901-1(2004).
16. C. J. Zapata-Rodríguez, Opt. Commun. **263**, 131 (2006).
17. C. Ding, B. Lü, L. Pan, Opt. Commun. **282**, 413 (2009).
18. M. V. Berry, New. J. Phys. **4**, 66.1 (2002).
19. M. V. Berry, New. J. Phys. **4**, 74.1 (2002).
20. O. V. Angelsky, A. P. Maksimyak, P. P. Maksimyak and S. G. Hanson, Opt. Express **13**, 8179 (2005).
21. O. V. Angelsky, A. P. Maksimyak, P. P. Maksimyak and S. G. Hanson, Opt. Express **14**, 7299 (2006).
22. O. V. Angelsky, S. G. Hanson, P. P. Maksimyak, A. P. Maksimyak, and A. L. Negrych, J. Europ. Opt. Soc. Rap. Public. **3**, 08029 (2008).

23. M. Dashtdar and M. T. Tavassoly, J. Opt. Soc. Am. A **26**, 2134 (2009).
24. W. Wang, T. Yokozeki, R. Ishijima, M. Takeda and S. G. Hanson, Opt. Express **14**,10195 (2006).
25. W. Wang, T. Yokozeki, R. Ishijima, A. Wada, Y. Miyamoto, M. Takeda and S. G. Hanson, Opt. Express **14**, 120 (2006).
26. V. Tikhonenko, J. Christou and B. Luther-Davies, J. Opt. Soc. Am. B **12**, 2046 (1995).
27. I. V. Kruglov, A. Yu Logvin and V. M. Volkov, J. Mod. Opt. **39**, 2277 (1992)
28. A. Raeurber, Current topics in Material Science **1**, 481 (1978).
29. A. V. Ilyenkov, L. V. Kreminskaya, M. S. Soskin and M. V. Vasnetsov, J. Nonlin. Opt. Phys. Mater. **6**,169 (1997).
30. L.V. Kreminskaya, M. S. Soskin and A. I. Khizhnyak, Opt. Commun. **145**, 377 (1997).
31. A. Deykoon, G. Swartzlander Jr., M. S. Soskin, 1st Int. Conf. on Singular Optics (Crimea, Ukraine) (1997).
32. M. M. Brundavanam, Nirmal K. Viswanathan and N. R. Desai, Opt. Lett. **32**, 2279 (2007).
33. M. M. Brundavanam, Nirmal K. Viswanathan and D. Narayana Rao, Appl. Opt. **47**, 6334 (2008).
34. M. M. Brundavanam, Nirmal K. Viswanathan and D. Narayana Rao, J. Opt. Soc. Am. A **26**, 2592 (2009).
35. M. M. Brundavanam, Nirmal K. Viswanathan and D. Narayana Rao, Opt. Lett. (Manuscript under preparation).
36. E. Wolf, Phy. Rev. Lett. **58**, 2646 (1987).
37. L. Mandel and E. Wolf, in Optical coherence and Quantum optics, (Cambridge Press, 1995), Chapter 5; E. Wolf, in Recent developments in quantum optics, Edited by R. Ingua, (Plenum, NY,1993), 369.
38. H. C. Kandpal, K. Saxena, D. S. Mehta, J. S. Vaishya and K. C. Joshi, J. Mod. Opt. **42**, 447 (1995).
39. D. Narayana Rao and V. Nirmal Kumar, J. Mod. Opt. **41**, 1757 (1994).
40. S. Vicalvi, G. S. Spagnolo and M. Santarsieo, Opt. Commun. **130**, 241 (1996).

41. H. C. Kandpal, J. S. Vaishya, K. Saxena, D. S. Mehta and K .C. Joshi, J. Mod. Opt. **42**, 445 (1995).
42. V. Nirmal Kumar, "Spectral interferometry: A study of the degree of coherence in the space-frequency domain and its applications", Ph.D. thesis (University of Hyderabad, India, 1997).
43. K. Creath, Phase measurement interferometry techniques, in Progress in optics, Edited by E. Wolf (North-Holland, 1988), vol. **26**.
44. E. N. Leith and J. Upatnieks, J. Opt. Soc. Am. **57**, 975 (1967).
45. B. J. Chang, R. Alferness and E. N. Leith, Appl. Opt. **14**, 1592 (1975).
46. D. F. V. James and E. Wolf, Radio. Sci. **26**, 1239 (1991).
47. W. E. Kock and J. L. Stone, Proc. IRE, **46**, 499 (1958).
48. J. Piasecki, B. Colombeau, M. Vampouille, C. Froehly and J. A. Arnaud, Appl. Opt. **19**, 3749 (1980).
49. U. Schnell, E. Zimmermann and R. Dandliker, J. Pure Appl. Opt. **4**, 643 (1995).
50. V. Nirmal Kumar and D. Narayana Rao, J. Opt. Soc. Am. B **12**, 1559 (1995).
51. P. Sandoz, G. Tribillon and H. Perrin, J. Mod. Opt. **43**, 701 (1996).
52. J. Kim, C. Choi and K. S. Soh, J. Korean Phys. Soc. **47**, 375 (2005).
53. T. H. Ko, D. C. Adler , J. G. Fujimoto, D. Mamedov, V. Prokhorov, V. Shidlovski and S. Yakubovich, Opt. Exp. **12**, 2112 (2004).
54. R. Leitgeb, C. K. Hitzenberger and A. F. Fercher, Opt. Express **11**, 889 (2003).
55. C. Iaconis and I. A. Walmsley, Opt. Lett. **23**, 792 (1998).
56. L. Gallmann, D. H. Sutter, N. Matuschek, G. Steinmeyer, U. Keller, C. Iaconis, I. A. Walmsley, Opt. Lett. **24**, 1314 (1999).
57. M. Lelek, F. Louradour, A. Barthelemy and C. Froehly, Opt. Commun. **261**, 124 (2006).
58. Thesis: "Spectral interferometry for the complete characterization of near infrared femtosecond and extreme ultraviolet attosecond pulses", Adam S. Wyatt (University of Oxford) (2007).
59. L. Mandel, J. Opt. Soc. Am. **57**, 613 (1967).

60. L. Mandel and E. Wolf, in Optical coherence and Quantum optics, (Cambridge Press, 1995), Chapter 4 and 5.
61. L. Mandel and E. Wolf, Rev. Mod. Phys. **37**, 231 (1965).
62. L. Mandel and E. Wolf, J. Opt. Soc. Am. **66**,529 (1976).
63. E. Wolf and W. H. Carter, Opt. Commun. **16**, 297 (1976).
64. M. J. Bastiaans, Opt. Acta **24**, 261 (1977).
65. M. Hercher, J. Opt. Soc. Am. **54**, 563 (1964).
66. R. Y. Chiao, E. Garmir and C. H. Towns, Phys. Rev. Lett. **13**, 479 (1964).
67. J. Reintjes, R. L. Garman and F. Shimizu, Phys. Rev. A **8**, 1486 (1973).
68. E. Yablonovitch and N. Bloembergen, Phys. Rev. Lett. **29**, 907 (1972).
69. C. G. Morgan, Rep. Prog. Phys. **38**, 621 (1975).
70. A. Braun, G. Korn, X. Liu, D. Du, J. Squier and G. Mourou, Opt. Lett. **20**, 73 (1995).
71. R. R. Alfano, *The supercontinuum laser source*, 2nd edition, Springer publications (USA) (2006).
72. A. Couairona and A. Mysyrowicz, Phys. Reports **441**, 47 (2007).

CHAPTER 2

Abstract

This chapter explains the experimental demonstration of the spectral shifts and spectral switches around the intensity minima (phase singularities) due to temporal correlation of the input optical field using dispersion compensated Michelson interferometer illuminated by a broadband white-light source operated in the spectral domain. Unusual behavior in the number of spectral fringes, measured within the source spectral bandwidth is shown as a function of optical path difference between the interfering beams.

Spectral shifts and spectral switches using a white-light Michelson interferometer

2.1 Introduction

There has been a considerable interest in the spectral anomalies such as spectral shifts and switches occurring around the phase singularities in various classes of scalar waves [1-3]. In particular, diffracted waves near intensity zero regions exhibit dramatic spectral shifts resulting in a number of interesting spectral characteristics [1-5]. In addition, use of interferometric techniques for mixing of two or more spectral colors [6] and for generating electric field components with different spectral densities using waves with different wave vectors [7] are also reported in the literature. Anomalous spectral behavior in the interference field of Young's double slit experiments illuminated by spatially completely and partially coherent polychromatic light is reported [8] considering its applications in information encoding and information transmission in free space.

All the above studies are based on the modulation of spatial coherence, bandwidth of the source spectrum [8] and diffraction angles [9]. The measurements mentioned in the above studies deal with on-axis and off-axis measurements which are manifestation of the real and imaginary parts of the complex degree of spectral coherence respectively [10]. In this chapter we experimentally demonstrate the spectral shifts and spectral switches around the intensity minima (Phase singularities) due to the temporal correlation of the input optical fields and unusual behavior in the number of spectral fringes observed within the spectral bandwidth of the source spectrum. In our studies, we use dispersion compensated Michelson interferometer (DC-MI) which is manifestation of the temporal coherence of the optical field due to the real part of the complex degree of spectral coherence. Throughout our experiment, the measurements are done at the center of the output beam. Characteristics of the

spectra calculated using interference law in the spectral-domain are compared with the experimental measurements.

It is important to note that understanding the spectral evolution in a DC-MI around phase singularities will be useful in shaping the spectral density of the wave, in optical correlation diagnostics of rough surfaces [11] and in vortex lattice appearance in the interference pattern due to three or more plane waves [12]. However, such a setup cannot produce a temporal correlation vortex (TCV), which may allow an understanding of zero coherence points of polychromatic partially coherent light source [13].

2.1.1 Advantages of optical system that produces temporal coherence induced spectral shifts and spectral switches

- The techniques mentioned in the previous studies using spatial coherence and diffraction induced spectral shifts and switches might be difficult in realization due to complexity involved in them. While in our present measurements using DC-MI, we can produce spectral shifts and spectral switches just by changing the position of one of the two mirrors which is relatively easy and accurate.

- In the optical systems based on the spatial coherence, compromise between intensity and visibility of the fringes is unavoidable and it is difficult to make the system compact. On the other hand temporal coherence based systems can be made more compact.

- In temporal coherence based systems, the interference fringes obtained are sharper than the spatial coherence based systems. This leads to a good signal to noise ratio for the measurements based on the temporal correlation effects.

2.2 Theory of spectral interference

The measurement of the degree of temporal coherence can be achieved using a dispersion compensated Michelson interferometer (DC-MI), where the degree of correlation is varied with the help of optical path difference (OPD) between the interfering beams [14].

Let $\{\varepsilon_{in}(\nu)\}$ represents the frequency dependent ensemble [15] of the field input into the interferometer, which satisfies all the usual conditions for a random fluctuating field. This beam is amplitude divided by a cubic beam splitter into $\{\varepsilon_1(\nu)\}$ and $\{\varepsilon_2(\nu)\}$. These beams are directed into the two arms of the interferometer. According to the principle of conservation of energy and assuming that the beam splitter is non-absorbing, the Stoke's relationship between the reflectivity 'r' and transmissivity 't' can be written as [16]

$$|r|^2 + |t|^2 = 1 \text{ and } rt^* + r^*t = 0 \tag{2.1}$$

The output beam of the interferometer monitored at a point P(r) in the observation plane is equal to the sum of the two fields after passing through the two arms of the interferometer, i.e.,

$$\varepsilon(\nu) = \varepsilon_1(\nu) + \varepsilon_2(\nu) \tag{2.2}$$

Where $\varepsilon_1(\nu)$ and $\varepsilon_2(\nu)$ are the fields emerging from the two arms of the MI and are related to the frequency dependent input field $\{\varepsilon_{in}(\nu)\}$ as

$$\begin{aligned} \varepsilon_1(\nu) &= a(\nu)\, \varepsilon_{in}(\nu) \text{ and} \\ \varepsilon_2(\nu) &= b(\nu)\, \varepsilon_{in}(\nu) \end{aligned} \tag{2.3}$$

Where $a(\nu)$ and $b(\nu)$ are the frequency dependent coefficients, which depend on the properties of the beam-splitter, on the path lengths the two beams traveling in the two arms of the DC-MI and are given by

$$a(\nu) = \text{rt exp}(ikL_1) \quad \text{and}$$
$$b(\nu) = \text{tr exp}(ikL_2) \tag{2.4}$$

Where k= $2\pi\nu/c$ and L_1 and L_2 are the total path lengths the light beams traveling in the two arms of the DC-MI. Using the Eq. (2.1), the two frequency dependent coefficients given by Eq. (2.4) can be shown to satisfy the relation

$$|a(\nu)+b(\nu)|^2 = 1 \tag{2.5}$$

The spectrum of the output field is given by

$$S(\nu) = \langle \varepsilon^*(\nu)\varepsilon(\nu) \rangle \tag{2.6}$$

Using Eq. (2.2), (2.3) and (2.4), the spectrum of the output field given by Eq. (2.6) can be simplified and written as

$$S(\nu) = |a(\nu)|^2 S_0(\nu) + |b(\nu)|^2 S_0(\nu) + 2a^*(\nu)b(\nu)S_0(\nu)\mu_{12}(\nu) \tag{2.7}$$

Where the S_0 (ν) is the input spectrum given by the ensemble average of the input field i.e.

$$S_0(\nu) = \langle \varepsilon_{in}^*(\nu)\varepsilon_{in}(\nu) \rangle \tag{2.8}$$

And the cross-spectral density of the two interfering beams is given by

$$\left\langle \varepsilon_1^*(\nu)\varepsilon_2(\nu)\right\rangle = \left\langle \varepsilon_2^*(\nu)\varepsilon_1(\nu)\right\rangle \propto S_0(\nu)\mu_{12}(\nu) \tag{2.9}$$

Assuming the beam-splitter to be r/t = 50/50, the reflectivity and the transmissivity are equal to

$|r| = |t| = 1/\sqrt{2}$. Using this value and the Eq. (2.4) and (2.5), it can be shown that

$$|a(\nu)|^2 = |b(\nu)|^2 = |r|^2 |t|^2 = 1/4$$

$$a^*(\nu)b(\nu) = |r|^2 |t|^2 \exp[ik(L_2 - L_1)] = (1/4)\exp(ik\Delta l) \tag{2.10}$$

Where $\Delta l = L_2 - L_1$ is the path difference between the interfering beams. Substituting the Eq. (2.8), (2.9) and (2.10) into the Eq. (2.7), the spectrum of the output field is given by the expression

$$S(\nu) = (1/2)S_0(\nu)\{1 + \mathrm{Re}[\mu_{12}(\nu)]\cos(k\Delta l)\} \tag{2.11}$$

Eq. (2.11) can be rewritten in terms of the wavelength 'λ' as

$$S(\lambda) = (1/2)S_0(\lambda)\{1 + \mathrm{Re}[\mu_{12}(\lambda)]\cos(k\Delta l)\} \tag{2.12}$$

Where 'Re' is the real part and $\mu_{12}(\lambda)$ is the complex degree of spectral coherence between the two interfering beams in the DC-MI and can be written in terms of the modulus and argument as [17]

$$\mu_{12}(\lambda) = |\mu_{12}(\lambda)|\exp[i\beta_{12}(\lambda)] \tag{2.13}$$

Where $|\mu_{12}(\lambda)|$ is the modulus and $\beta_{12}(\lambda)$ the phase of the complex degree of spectral coherence of the white-light. For spatially coherent optical field, Re $[\mu_{12}(\lambda)] = |\mu_{12}(\lambda)| \cos[\beta_{12}(\lambda)]$. The modulus of the degree of spectral coherence

$|\mu_{12}(\lambda)| = V$, the visibility of spectral interference fringes , assumed to be equal to one here. Then Eq. (2.12) becomes

$$S(\lambda) = \frac{1}{2} S_0(\lambda)\{1 + \cos[k\Delta l]\} \tag{2.14}$$

Here $\{1+\cos[k\Delta l]\}$ is the 'modifier function' and is a function of the OPD between the interfering arms. It changes the input spectrum as OPD changes. Adjusting the path difference between the interfering beams, $\Delta l = 0$ is critical so that the interference spectrum matches with the lamp spectrum, to begin with. This is achieved by moving one of the interferometer arms with respect to the other in air. If the OPD is increased from zero, the output spectrum coinciding with the source spectrum shifts towards red, splits in to two spectral lines of equal intensity and then is blue shifted. The output spectrum having two peaks of equal intensity is referred as *'spectral switch' position.* At spectral switch position the spectral intensity at wavelength corresponding to lamp spectral maximum is zero and modifier function at this wavelength becomes zero as given below

$$S(\lambda_0) = \frac{1}{2} S_0(\lambda_0)\left\{1 + \cos\left[\frac{2\pi}{\lambda_0}\Delta l\right]\right\} = 0 \tag{2.15}$$

$$\left\{1 + \cos\left[\frac{2\pi}{\lambda_0}\Delta l\right]\right\} = 0$$

$$\cos\left[\frac{2\pi}{\lambda_0}\Delta l\right] = -1$$

$$\Delta l = \frac{\lambda_0}{2\pi}(2m+1)\pi = \frac{2m+1}{2}\lambda_0 \tag{2.16}$$

Where m=0, 1, 2 .....

2.3 Experimental details

Schematic of the experimental setup shown in Fig. 2.1 consists of a dispersion compensated Michelson interferometer, illuminated by a white-light source (fiber-coupled, collimated 50 W quartz tungsten-halogen lamp). A fiber-coupled spectrometer (SD2000, Ocean Optics, USA) is kept at the output of the interferometer to measure the spectral modifications arising due to varying temporal correlation. One of the interferometer mirrors (M_2) is mounted on a nano-positioner (NanoPZ, Newport, USA) and is capable of a minimum path difference between the interfering beams of 10 nm. A personal computer is used to control the nano-positioner movement and for acquisition of corresponding spectral data from the spectrometer. The spectral characteristics of the white-light source measured in the range from 300 – 1000 nm by closing one of the interferometer arms is fitted to $I = A\exp(-\exp(-z) - z + 1)$ with $z = (\lambda-\lambda_0)/\Delta\lambda$ (The above equation is adopted from one of the peak functions of the Origin software called, *Extreme* as the source spectrum does not fit to any standard functions). Here A is the amplitude, λ_0 is the center and $\Delta\lambda$ is the width of the spectral peak. The FWHM spectral bandwidth ($\Delta\lambda$) is found to be 238 nm with peak wavelength (λ_0) at 612 nm. Using these values the coherence length ($l_c \sim \lambda_0^2/\Delta\lambda$) of the source is calculated to be 1.57 μm. When the characteristic of the interference spectrum is similar to that of the lamp spectrum the corresponding OPD between the interfering beams is zero.

By increasing the path difference between the two interfering beams in steps of 10 nm from zero using the computer controlled nano-positioner the corresponding spectral modifications are recorded up to OPD (Δl) of 2 μm, corresponding to $\Delta l > l_c$. From the measured modified spectra we calculate the intensity corresponding to the spectral maximum ($I(\lambda_i)$), the corresponding wavelength (λ_i), and the number of spectral fringes (m) as a function of path difference between the interfering beams.

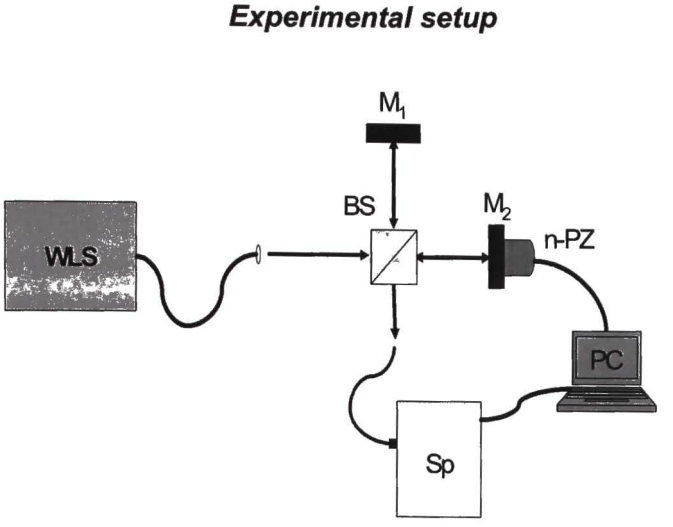

Figure 2.1: *Schematic of the experimental setup. WLS. White light source; BS· 50-50 Beam splitter; M_1, M_2: Mirrors, n-PZ: Nano positioner; Sp: Spectrometer, PC: Personal computer.*

2.4 Results and discussions

As we increase the OPD between the interfering beams from Δl = 0 μm, the spectral peak starts to shift towards red wavelength and splits into two asymmetric peaks – one red shifted and one blue shifted. Such an asymmetric split upon further increase in OPD leads to spectral peaks of almost equal intensity when Δl = 0.28 μm, corresponding to a phase difference between the interfering beams of $\Delta\phi = \pi$. This position is referred to as spectral switch [1], due to the sudden change from red shift to blue shift of the lamp spectrum. This change from a gradual spectral shift to rapid spectral switch is due to the temporal correlation in our experiment. Further increase in Δl results in an increasing dominance of the blue shifted spectral line over the red shifted one until the two spectral peaks merges into one and coincides with that of the lamp spectrum when Δl = 0.62 μm. At this point the interference spectrum is almost

the same as the lamp spectrum and that corresponding to $\Delta l = 0$ μm but for ~ 70 nm reduction in the spectral bandwidth. The reduction in $\Delta\lambda$ is attributed to the redistribution of the optical power into the reflected spectrum of the interferometer. This is confirmed by recording the reflection (R) and transmission (T) spectra of the interferometer at the same time in the two channels of the spectrometer. The transmission and reflection spectrum for OPD $\Delta l = 0.62$ μm is shown in Fig. 2.2. It is clearly seen from the figure that the missing spectral content in the transmission spectrum is restored in the reflection spectrum. Fig. 2.3 is a grey scale plot of the spectral behavior in measured in transmission due to temporal correlation, discussed above.

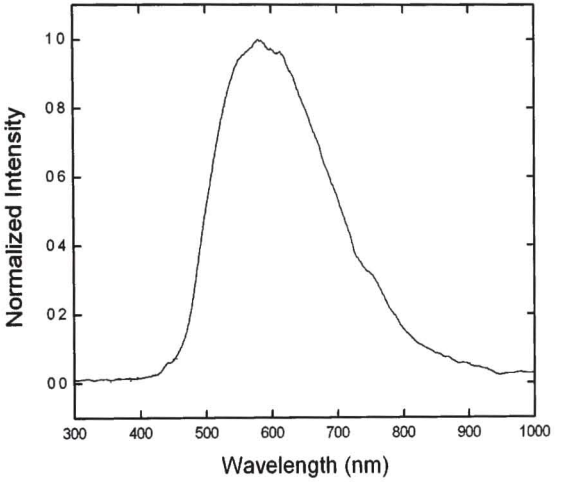

Figure 2.2: *Transmission and reflection spectra of the output spectrum for Δl = 0 62 μm Continuous line represents transmission spectrum and dotted line represents reflection spectrum*

Also shown in Fig. 2.3 are the line plots for five different path delays (indicated by arrows) and the corresponding spectra are calculated using the interference law in the spectral domain as given by Eq. (2.14). The behavior of the spectrum of interfering beams discussed above is somewhat similar to the behavior of focused waves on a circle centered at a singular point [2].

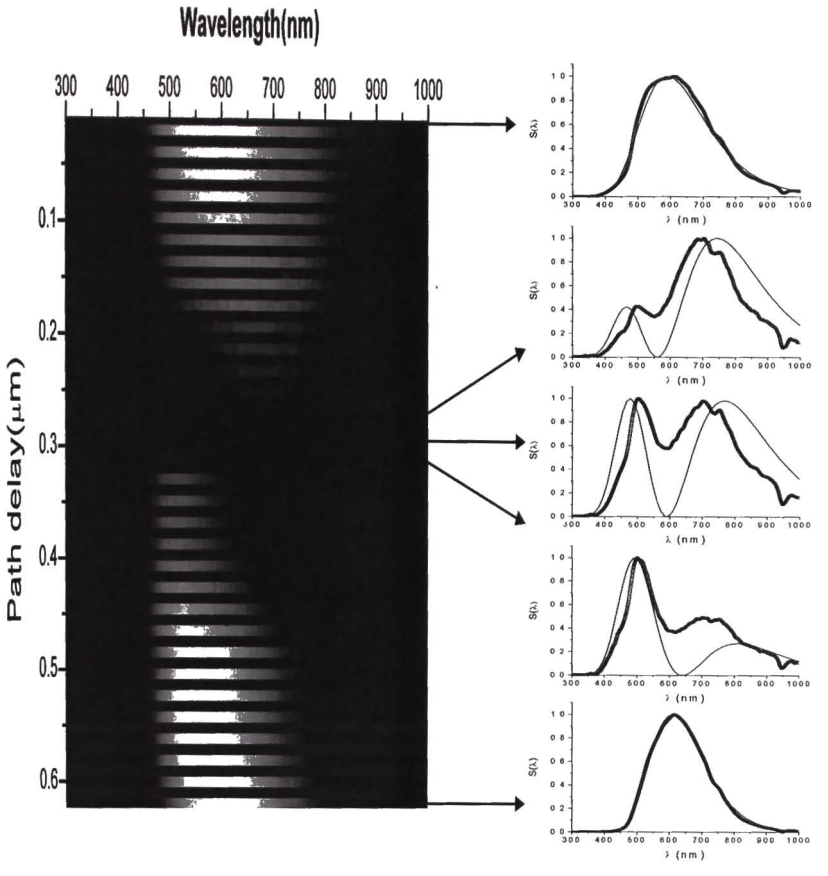

Figure 2.3: *2-D plot of the spectral changes as a function of path delay around the first intensity minimum Also shown are line plots of the spectra (open circles) for path delays Δl = 0, 0 26, 0.28, 0 30 and 0.62 μm respectively (as indicated by arrows) and the corresponding calculated curve (continuous line) using Eq (2 14)*

The normalized peak spectral intensity for increasing OPD between the interfering beams is plotted in Fig. 2.4. It is seen from Fig. 2.4 that the minima in peak spectral intensity occur at OPD of Δl = 0.28, 0.9 and 1.48 μm and the contrast in peak spectral intensity decreases with increasing OPD. This confirms the observation that the spectral intensity is almost zero at λ_0 only when Δl = 0.28 μm and the sharp, colored interference fringes gets blurred with increasing OPD.

The behavior of peak spectral intensity with OPD matches well with the curve generated using Eq. (2.14), shown using continuous line in Fig. 2.4. We have plotted in Fig. 2.5 the OPD dependence of normalized spectral shift (NSS), calculated using $\delta\lambda/\lambda_0 = (\lambda_0 - \lambda_1) / \lambda_0$, where λ_0 is the lamp spectrum maximum and λ_1's are the wavelength at which the spectral intensity has the highest value. Normalize spectral shift, $\delta\lambda/\lambda_0 = 0$ corresponds to the position at which we observe the interference spectrum resembles the lamp spectrum with single maximum at λ_0. Measured behavior of the NSS shows that spectral switches occur at OPDs corresponding to the minima in peak spectral intensity. Also shown in Fig. 2.5 is the curve corresponding to the behavior of NSS versus Δl, calculated using Eq. (2.14). The asymmetry in the plot with respect to zero NSS arises from the asymmetry in the lamp spectrum with respect to λ_0 and the dependence of the asymmetry of the NSS values on the input spectrum are discussed in more detail in chapter 4. The small deviations in the spectral switch positions between the experimental and calculated curves are attributed to the instability of the interferometer.

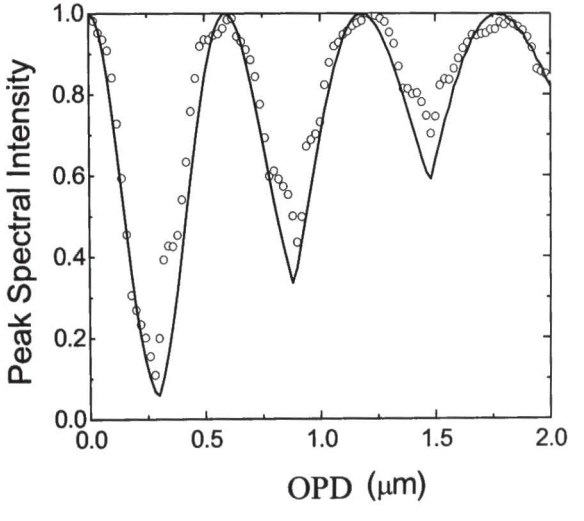

***Figure 2.4**: Plot of normalized peak spectral intensity as a function of optical path difference (OPD) between the interfering beams. Open circle: experimental data, continuous line data simulated using Eq. (2.14).*

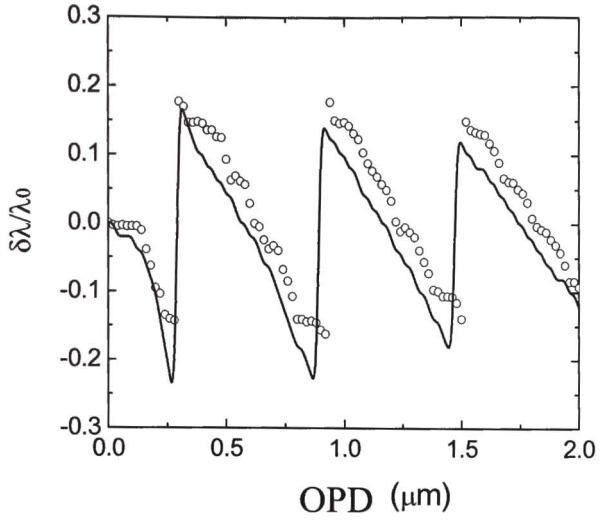

Figure 2.5: *Normalized spectral shift ($\delta\lambda/\lambda_0$) as a function of optical path difference (OPD) between the interfering beams. Open circle: experimental data, continuous line: data simulated using Eq. (2.14).*

In Fig. 2.6 we plot the number of spectral fringes measured, which corresponds to the number of spectral maxima in the interference spectrum within the wavelength range from 300 – 1000 nm, as a function of optical path difference between the interfering arms. The number of interference fringes in the spectral domain (m), when calculated using $m = (2\Delta l \Delta\lambda)/\lambda_0^2$, where $\Delta\lambda$ and λ_0 are the spectral bandwidth (FWHM) and peak wavelength of the source and Δl is the optical path difference between the interfering beams [18], increases linearly with Δl, as shown by the dotted line in Fig. 2.6.

For a lamp with fixed spectral characteristics, instead of a linear increase in m with Δl every time $\Delta\phi$ increases by 2π (shown as dotted line in Figure 2.6), we observe that m increases from one to two fringes around the first spectral switch position ($\Delta\phi = \pi$) but becomes one fringe just beyond that. The number of fringes upon further increase in Δl becomes two ($\Delta\phi = 2\pi$) and then to three fringes before coming back to two fringes again. This unusual behavior in m –

versus – Δl follows the expected behavior of increase by one fringe every time $\Delta\phi$ increases by 2π beyond $\Delta l \sim 1.5$ μm, and was verified experimentally. In this context it is important to emphasize that the behavior of number of fringes with optical path difference within the first two spectral switch points is unusual and is observed here for the first time.

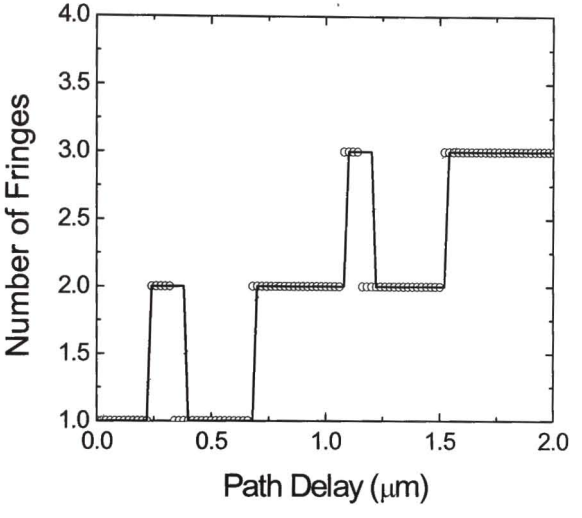

Figure 2.6: *Number of fringes as a function of path delay between the interfering beams Open circles. experimental data, continuous line data calculated from simulated spectra and dotted line data calculated using* $m=2\Delta l/l_c$

2.5 Conclusions

In this chapter we experimentally demonstrated the temporal correlation induced spectral shifts and spectral switches using white-light dispersion compensated Michelson interferometer. The normalized peak spectral shift and corresponding normalized peak intensity are studied as a function of optical path difference between the interfering arms. If the normalized spectral shift (NSS) is positive then the spectral peak of the interference spectrum is blue shifted, if it is negative then the spectral peak is red shifted with respect to the input source spectrum.

Zero value of the NSS corresponds to the spectral peak of the output interference spectrum coinciding with the input source spectral maximum. The anomalous behavior in the number of spectral fringes observed within the spectral bandwidth of the input spectrum is also presented.

References

1. J. Pu, H. Zhang, and S. Nemoto, Opt. Commun. **162**, 57 (1999).
2. G. Gbur, T. D. Visser, and E. Wolf, Phys. Rev. Lett. **88**, 013901 (2002).
3. G. Popescu and A. Dogariu, Phys. Rev. Lett. **88**, 183902 (2002).
4. G. Gbur, T. D. Visser, and E. Wolf, J. Opt. Soc. Am. A **19**, 1694 (2002).
5. J. T. Foley and E. Wolf, J. Opt. Soc. Am. A **19**, 2510 (2002).
6. T.E. Kiess and R.E. Berg, Am. J. Phys., **64**, 928 (1996).
7. L. E. Helseth, Phys. Rev. E **73**, 026602 (2006).
8. J. Pu, C. Cai and S. Nemoto, Opt. Express **12**, 5131 (2004).
9. B. K. Yadav, N. S. Bisht, R. Mehrotra, H. C. Kandpal, Opt. Commun. **277**, 24 (2007).
10. V. N. Kumar and D. N. Rao, J. Mod. Opt. **48**, 1455 (2001).
11. O.V. Angelsky, A. P. Maksimyak, P. P. Maksimyak, and S. G. Hanson, Opt. Express **14**, 7299 (2006).
12. J. Masajada, A. Popiołek-Masajada, and M. Leniec, Opt. Express **15**, 5196 (2007).
13. G. A. Swartzlander and J. Schmit, Phys. Rev. Lett., **93**, 093901 (2004).
14. G. S. Agarwal and D. F. V. James, J. Mod. Opt. **40**, 1431 (1993); D. Narayana Rao and V. Nirmal Kumar, J. Mod. Opt. **41**, 1757 (1994); D. S. Mehta, H. C. Kandpal, K. Saxena, J. S. Vaishya and K. C. Joshi, Opt. Commun. **119**, 352 (1995).
15. E. Wolf, J. Opt. Soc. Am. **72**, 343 (1982).
16. Z. Y. Ou and L. Mandel, Am. J. Phys. **57**, 66 (1989).
17. M. Santarsiero and F. Gori, Phys. Lett. A **167**, 123 (1992).
18. J. Calatroni, A. L. Guerrero, C. Sainz and R. Escalona, Opt. Laser Technol. **28**, 485 (1996).

CHAPTER 3

Abstract

This chapter explains the novel experimental method we developed to measure nanometer displacements using wavelength shifts of spectral peaks around spectral switch or singular phase points in the interference spectra due to temporal correlation in dispersion compensated Michelson interferometer illuminated by a broadband white-light source. Dramatic changes in the spectral characteristics are recorded as a function of optical path difference between the interfering beams around the spectral switch position occurring with in the coherence length of the source. These are then compared with measurements far from the coherence length in order to demonstrate the higher sensitivities involved in the proposed method.

Measurement of nano-scale displacement using spectral shifts around spectral switches in a white-light Michelson interferometer

3.1 Introduction

There is an ever increasing need for novel techniques for metrology applications including measurement of displacements in the nanometer scale, to augment the on-going nano-technology revolution. Several approaches have been reported in recent times like the use of phase singularity in the complex analytic signal of a speckle pattern as indicators of displacement in nanometer scales [1], an interferometric phase-meter based on attenuated total internal reflection as nano-scale linear sensor [2], and spectral domain phase microscopy for detection of nanometer-scale motions in living cells [3], among others. Of the different tools available for nano-metrology, optical interferometric techniques are widely used for most accurate measurement of displacements as they are simple and highly sensitive compared to other techniques [4 – 6].

Among the different interferometer designs available for the measurement of displacement, Michelson Interferometer (MI) is an overwhelming favorite for many practical applications [4, 5]. Different fringe analysis procedures were introduced to extract more information from the recorded interferogram, leading to higher sensitivities and accuracies [7]. Instead of working with a single wavelength source, techniques were developed for accurate measurement of displacements through the study of spatial interference pattern using more than one wavelength or even a broadband white light source [5].

Alternately, spectral-domain white-light interferometric technique has also been developed for accurate measurement of displacement, where the minimum measurable optical path difference (OPD) is determined by the central

wavelength (λ_0) and the spectral width ($\Delta\lambda$) of the white light source and the maximum measurable OPD is determined by the central wavelength of the source and the spectral resolving power ($\delta\lambda$) of the spectrometer [8 - 14]. Spectral-domain interference method [15] is of particular interest here as it overcomes the limitation of path length measurement range due to coherence length of conventional laser-based interferometry with the advantage of longer measuring range and higher sensitivities for displacement measurements than those achievable using time-domain methods.

In the previous chapter we have explained the anomalous spectral behavior due to temporal correlation in a white-light interferometer, where we attributed the spectral shifts, spectral switches and unusual behavior in the number of spectral fringes to operating the Michelson interferometer around phase singularities [16]. During our experiments it was noticed that around the spectral switch position, occurring as a result of phase singularity in the interference spectra, the sensitivity of the interferometer is very high and the observed spectral shifts can be used to accurately measure nanometer displacements. In this chapter, we report the experimental measurement of nanometer displacements using spectral shifts around spectral switch positions occurring within the coherence length (spectrum with two spectral peaks) and far away from the coherence length (spectrum with nine spectral peaks) of the source with given spectral bandwidth using dispersion compensated Michelson interferometer (DC-MI).

Initially, the measurements were made using two fringes, with the initial optical path difference (OPD) of the interferometer kept such that it is on one side of the spectral switch position. An appropriate displacement of one of the interferometer mirror resulted in the spectral peak shifting from the red to the blue side of the lamp spectral maximum or vice-versa through the spectral switch position. This measurement was compared with the spectral shifts measured using the conventional spectral interferometric technique, where the optical path difference (OPD) between the interfering beams is more than the coherence

length of the source, resulting in nine fringes within the spectral bandwidth. Based on our measurements we suggest that the proposed method of using the spectral interferometer around the spectral switch position with two fringes results in high-sensitivity measurement of nanometer displacement.

3.2 Spectral interference law

The spectral interference law for a dispersion compensated MI is given by [15, 16]

$$S(\lambda) = \frac{1}{2} S_0(\lambda)\{1 + \mathrm{Re}[\mu_{12}(\lambda)]\cos[\kappa \Delta l]\} \tag{3.1}$$

where $S_0(\lambda)$ is the lamp spectrum, $\kappa=2\pi/\lambda$ and Δl is the OPD between the two arms of the interferometer. Re $[\mu_{12}(\lambda)]$ is the real part of the complex degree of the spectral coherence. $\mu_{12}(\lambda)$ is assumed to be equal to one and its phase assumed to be zero. Eq. (3.1) then becomes

$$S(\lambda) = \frac{1}{2} S_0(\lambda)\{1 + \cos[\kappa \Delta l]\} \tag{3.2}$$

Here $\{1+\cos[(2\pi/\lambda)\Delta l]\} = \{1+\cos(\Delta\phi)\}$ is the spectral modifier function, where $\Delta\phi$ is the phase difference between the interfering beams.

3.3 Experimental Details

Details of the experimental setup shown in Fig. 3.1 are given in the previous Chapter. Briefly, it consists of a DC-MI with one of the mirrors (M_2) mounted on a nano-positioner (NanoPZ, Newport, USA) capable of a minimum step size of 10 nm. The white light source used is a 50 W tungsten-halogen lamp coupled to an optical fiber with collimating lens and the spectral modifications at the interferometer output are measured using a fiber-coupled spectrometer (SD2000, Ocean Optics, USA). A personal computer is used to control the nano-positioner movement and acquiring corresponding spectral data from the spectrometer.

The spectrum of the white light source is recorded first in the range from 300 – 1000 nm by closing either one of the interferometer arms. As the measured spectrum is a complex convolution of emission from the lamp, optical components used in the interferometer and spectral response of the CCD camera, it does not fit to any standard spectral profiles and so is fitted to a peak function of the form given by $I = A\exp(-\exp(-z) - z + 1)$, with $z = (\lambda - \lambda_0)/\Delta\lambda$. Here A is the amplitude, λ_0 is the center and $\Delta\lambda$ is the width of the spectral peak. The FWHM spectral bandwidth ($\Delta\lambda$) is found to be 238 nm with peak wavelength (λ_0) at 612 nm. Using these values, the coherence length (l_c) of the source is calculated to be 1.57 μm. The experiment is carried out both within the coherence length ($\Delta l < l_c$) of the source and for longer distances ($\Delta l > l_c$) with the path difference between the two interfering beams changed in different step sizes using the computer controlled nano-positioner.

Experimental setup

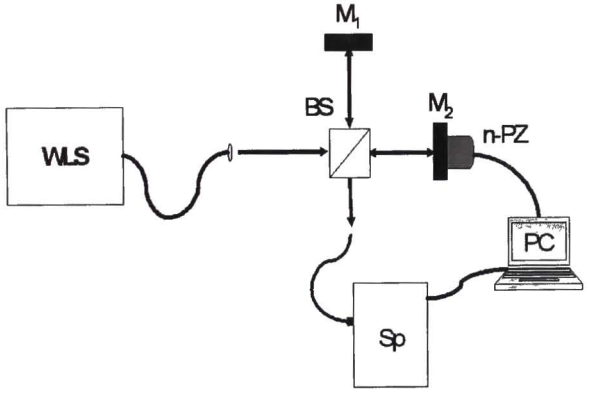

Figure 3.1: *Schematic of the experimental setup. WLS. White light source; BS. 50-50 Beam splitter; M_1, M_2: Mirrors; n-PZ: Nano positioner; Sp. Spectrometer; PC. Personal computer*

3.4 Results and discussion

First the optical path difference between the two interfering beams (Δl) is made zero so that the spectrum after interference coincides with the lamp spectrum. When Δl increases, the spectrum first shifts towards the red-side with decrease in the intensity of the peak and then splits into two spectral maxima of equal intensity, one on either side of the lamp spectrum maximum. Around this position a rapid transition of the spectral maximum from red side to blue side and blue side to red side occurs with further increase or decrease in the OPD. The blue side peak increases in intensity with a corresponding change in peak wavelength for still longer OPDs but well below the coherence length (l_c) of the source. When two peaks are observed in the spectrum, we define the spectral peak as the one with higher intensity. Interference spectrum with more than two spectral maxima appears for OPDs beyond the coherence length of the source [17, 18]. A change in the number of spectral maxima with increase in OPD is also reported in Ref 16. The above-mentioned situation corresponding to two spectral peaks designated as the blue and the red peaks and having equal intensity is referred to spectral switch position [16]. As the rapid transition of the spectral intensity maximum from red peak to blue peak or vice-versa around the spectral switch position is highly sensitive to the OPD between the two interfering arms, we carried out the measurements in this configuration first.

Two distinctive methods were adopted here to measure the displacements around the spectral switch position, details of which are discussed in the following sections. Briefly, in the first method, the initial position of the mirror starts on one side of the spectral switch position and crosses onto the other side depending on the mirror displacement with respect to the spectral switch position. This method uses the first spectral switch with just two fringes in the interference spectrum. In the second method, the interfering beams are delayed by more than the coherence length of the source. This results in nine spectral fringes and they are used to measure the small displacements by measuring the spectral peak shift. Results from the two methods are compared to estimate the sensitivities involved in the measurement of nanometer displacement.

3.4.1 Method–1: Nano-displacement measurement using the spectrum with two spectral peaks

In this method accurate displacement measurements are done using the spectral shifts around the spectral switch position (occurring at 280 nm for the present setup) with two fringe spectrum occurring with in the coherence length of the source. Depending on the measurement magnitudes, the initial position of the spectrum is set on one side of the spectral switch position and the mirror M_2 is moved into a position such that the displacement results in the spectrum crossing through the spectral switch position. As the minimum step size of the nano-positioner used in our experiment is 10 nm and to measure the displacements around and crossing through the spectral switch, we consider the spectral shift from the spectrum at Δl= 260 nm (Fig. 3.2(a)) to the spectrum at Δl= 300 nm (Fig. 3.2(c)) resulting in the spectral peak shift from red to blue side crossing through the spectral switch position (Fig. 3.2(b)) at Δl= 280 nm. The open circles in Fig. 3.2 are experimental data and the continuous lines are from numerical calculations, using Eq. (3.2).

The spectral shift normalized to the lamp spectrum is calculated using $(\lambda_0 - \lambda_{peak}) / \lambda_0$ as a function of OPD between the interfering arms around the spectral switch position (with two fringes) is shown in Fig. 3.3. Open circles are the experimental data and continuous line is the data calculated using Eq. (3.2). The negative and positive values of the spectral shift correspond to the red and blue shift of the spectrum respectively with respect to the lamp spectrum and zero value corresponds to the spectrum with spectral peak coinciding with the lamp spectrum. The rapid transition in the spectral shift values from negative (red) to positive (blue) in Fig. 3.3 occurs around the spectral switch position.

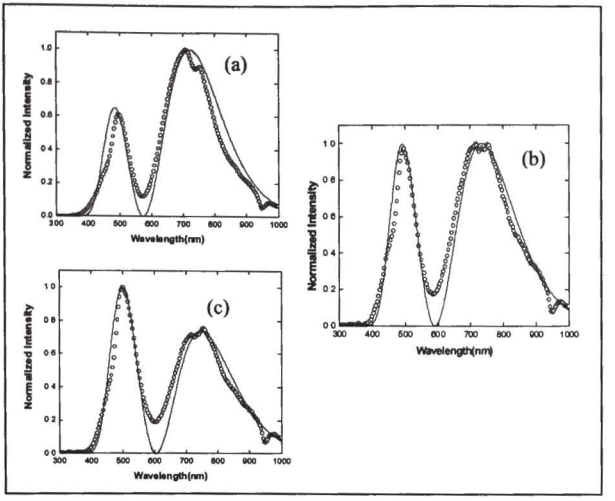

Figure 3.2: *Spectral modulations around the spectral switch position with two spectral fringes (Method 1); (a) and (c) correspond to the spectra around the spectral switch position for OPDs of 260 and 300 nm respectively; (b) corresponds to the spectrum at the spectral switch position for the path difference 280 nm. Open circles are experimental data and continuous lines are the spectra calculated using Eq. (3.2).*

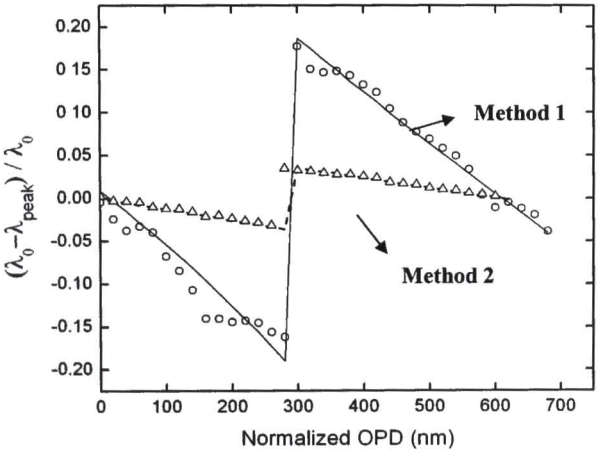

Figure 3.3: *Plot of $[(\lambda_0 - \lambda_{peak}) / \lambda_0]$ as a function of OPD around the spectral switch position with two fringe spectrum(Method 1) and nine fringe spectrum (Method 2)*

3.4.2 Method-2: Nano-displacement measurement using the spectrum with nine spectral peaks

Next, we consider the situation where the OPD between the interfering beams is Δl = 8.26 μm, far from coherence length (l_c=1.57 μm) of the source resulting in interference spectrum with nine fringes and the displacement measurements are done using the spectral shifts around the spectral switch occurring between the two central peaks. Fig. 3.4 shows the experimental spectra with nine spectral interference fringes for two OPDs of Δl = 8.26 μm and 8.28 μm between the interfering arms around the spectral switch position. The arrow in the Fig. 3.4 shows the spectral shift from red peak (continuous line) to the blue peak (dotted line) for 10 nm displacement of the mirror M_2 crossing through the spectral switch position. Fig. 3.3 shows the spectral shift normalized with lamp spectrum calculated using $(\lambda_0 - \lambda_{peak}) / \lambda_0$ as a function of normalized path difference (by normalization, the path difference at which the spectral switch occurs is made same for both the methods for comparison) between the interfering arms around the spectral switch position far from the coherence length. Open triangles are the experimental data and dashed line is the curve corresponding to numerical calculations using Eq. (3.2). It can be observed from Fig. 3.3 that the spectral shift from red to blue around the spectral switch with nine peaks is much smaller than that of the spectral switch with two peaks.

3.5. Discussion

3.5.1 Spectral switch amplitude (SSA)

To evaluate the sensitivities involved in the measurement suitable for nanometer displacements, we calculate and compare the Spectral switch amplitudes (SSAs) for the above-mentioned methods. The SSA, a measure of the displacement around the spectral switch position is defined as

$$\begin{aligned} SSA &= \{[(\lambda_0 - \lambda_{bluepeak}) / \lambda_0] - [(\lambda_0 - \lambda_{redpeak}) / \lambda_0]\} \\ &= (\lambda_{redpeak} - \lambda_{bluepeak}) / \lambda_0 \end{aligned} \qquad (3.3)$$

where, $\lambda_{redpeak}$ is the peak wavelength of the initial spectrum, $\lambda_{bluepeak}$ is the peak wavelength of the spectrum after each displacement crossing through the spectral switch position. The SSA is also defined as the magnitude of the rapid transition around and crossing the spectral switch position which is different for different displacements of the mirror M_2. Once the SSA values are calculated for different displacements of the mirror M_2 for a given lamp spectrum, any unknown displacement can be inferred from the SSA values that are obtained. In addition, as long as the displacement of the mirror M_2 causes the peak shift from red to blue or vice versa, the spectral shifts can be either symmetric or asymmetric around the spectral switch position.

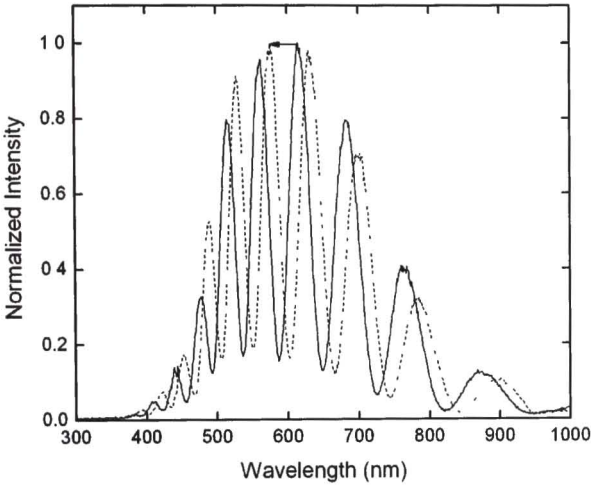

Figure 3.4: *Experimental spectra with nine spectral fringes. Continuous line Initial position of the spectrum (red shifted); dotted line: blue shifted spectrum for 10 nm displacement of the mirror M_2 crossing through the spectral switch position*

3.5.2 Comparison between the two proposed methods

In the first method, displacements were measured independent of the initial position of the two-fringe spectrum, provided the mirror displacement takes the fringes through the spectral switch position. In this case the SSAs are calculated

to be 0.344, 0.339, 0.333, 0.306 and 0.299 respectively for d = 10 to 50 nm in steps of 10 nm. A plot of the variation of SSA as a function of the mirror displacement'd' for the above two methods are given in Fig. 3.5. In this figure, open circles and continuous line represent the experimental data and the corresponding linear fit for Method 1. The second method, corresponding to $\Delta l > l_c$, the shift in spectral fringes are measured for different displacements of the mirror M_2 and the SSAs are calculated to be 0.066, 0.064, 0.060, 0.059 and 0.057 respectively for the d = 10 to 50 nm in steps of 10 nm. Open triangles (in Fig. 3.5) are the experimental data and dotted line is the corresponding linear fit when the displacements are measured from nine fringe interference spectra. The slopes of the linear fits corresponding to Methods 1 and 2 are $-10.9\text{x}10^{-4} \pm 2.79\text{x}10^{-5}$ and $-3.84\text{x}10^{-4} \pm 1.83\text{x}10^{-5}$ nm^{-1} respectively.

From Fig. 3.5 it is observed that the measured SSA values and the slope of the corresponding linear fit using the Method 1 are comparatively larger than those of the Method 2. Thus it can be inferred that the sensitivity of the spectral shifts at the spectral switch position with two spectral peaks for $\Delta l < l_c$ is higher than that measured using normal spectral interferometric technique which is usually carried out at distances far from the coherence length of the source. The high values of SSA for small displacements using Method 1 imply that this method has higher sensitivity for the measurements of small displacements. Small variations in the experimental data from the calculated behavior can be attributed to the instability of the interferometer system, as our interferometer was not mounted on any vibration isolation table and other precautions such as temperature stability, etc were not taken. The stability can however be improved by performing the experiment in a more controlled environment.

References

1. W. Wang, T. Yokozeki, R. Ishijima, A. Wada, Y. Miyamoto, M. Takeda and S.G. Hanson, Opt. Express **14**, 120 (2006).
2. H. Stoyanov, Proc. SPIE, **6604**, 66040R 1 (2007).
3. M.A. Choma, A.K. Ellerbee, C. Yang, T.L. Creazzo and J.A. Izatt, Opt. Lett. **30**, 1162 (2005).
4. J. Lawall, Opt. Photon. News p-40, October (2004).
5. P. Hariharan, *Optical Interferometry*, 2nd edition, Academic Press (2003).
6. K. Nakayama, M. Tanaka, F. Shiota and K. Kuroda, Metrologia, **28**, 483 (1991/92).
7. H. J. Tiziani, Opt. Quantum Electron. **21**, 253 (1989).
8. L. M. Smith and C.C. Dobson, Appl. Opt. **28**, 3339 (1989).
9. U. Schnell, E. Zimmermann and R. Dändliker, Pure Appl. Opt. **4**, 643 (1995).
10. P. Sandoz, G. Tribillon and H. Perrin, J. Mod. Opt. **43**, 701 (1996).
11. I. Verrier, G. Brun and J.P. Goure, Appl. Opt. **36,** 6225 (1997).
12. P. Hlubina, Opt.Commun. **212**, 65 (2002).
13. S. Costantino, O.E. Martinew and J.R. Torga, Opt. Express. **11**, 952 (2003).
14. H. Chen, T. Liu and Z. Meng, Proc. SPIE, **6831**, 6831108 (2007).
15. V. Nirmal Kumar and D. Narayana Rao, J. Opt. Soc. Am. B **12**, 1559 (1995).
16. M. M. Brundavanam, N. K. Viswanathan and D. N. Rao, Opt. Lett., **32**, 2279 (2007).
17. P. Hlubina, J. Mod. Opt. **44**, 1049 (1997).
18. V. Nirmal Kumar, "PhD thesis: Spectral interferometry: A study of the degree of coherence in the space-frequency domain and the applications," (1997).

CHAPTER 4

Abstract

In this chapter, a detailed experimental study is carried out to demonstrate the effect of the input lamp spectral characteristics such as spectral bandwidth, peak wavelength and shape of the spectrum on the spectral shifts and spectral switches due to temporal correlation in a white light Michelson interferometer operated in the spectral domain. The behavior of the switch position, spectral switch amplitude and the symmetry of the spectral shifts at the switch position are discussed in detail as a function of optical path difference between the interfering beams. The experimental results are compared with the numerical calculations carried out using interference law in the spectral domain. Based on our results we feel that our study is of critical importance in the selection of source spectral characteristics to further improve the longitudinal resolution or the measurement sensitivity in spectral-domain optical coherence tomography and microscopy.

Effect of input spectrum on spectral switch characteristics in a white-light Michelson interferometer

4. 1. Introduction

There has been a significant effort put in investigating a source with well defined spectral characteristics as the spectral characteristics play an important role in the optical coherence tomography (OCT) [1]. The spectral characteristics such as spectral bandwidth ($\Delta\lambda$), peak wavelength (λ_0) and shape of the input spectrum characterize the power spectral density (PSD) which has critical importance in OCT and microscopy especially to estimate and improve the longitudinal resolution [2, 3]. The PSD of the source sets the temporal width of the interference signal which consequently sets an upper bound on the longitudinal resolution of the OCT in a low coherence interferometer [1]. Spectral-domain OCT[4], also known as Fourier-domain OCT, carried out using a broad band superluminescent diode has become a promising technology due to its practical use in obtaining sample images with ultra high resolution and at high speed than possible with conventional time-domain OCT [5,6].

Extensive theoretical and experimental studies have been carried out on spectral anomalies such as spectral shifts and spectral switches observed in various class of polychromatic scalar fields, owing to the spatial coherence of the source [7-11]. In particular, dramatic spectral changes in the vicinity of intensity zeros due to diffraction of spatially coherent polychromatic waves at a circular aperture [10] and in the focal region due to converging spherical waves [11] are studied. Many theoretical studies have demonstrated that these dramatic spectral shifts, due to modified spatial coherence of the source can be used to generate new types of filters which might find applications in optical signal processing and cryptography [12, 13]. Interferometric techniques to mix two or more colors for the generation of electric field components using waves with different wave

vectors are also reported [14, 15]. More recently, the influence of the spatial coherence on the spectral anomalies in the Young's double slit experiment illuminated with polychromatic light for free space communication is also reported [16]. It has also been reported in literature that the diffraction-induced spectral switch effect fades away for ultra-broad band spectra unlike narrow-band spectra in the focal plane of apertured focused beams [17]. The dependence of the spectral shifts and switches on the obscuration ratio, temporal coherence length, spatial correlation parameter and diffraction angle in Young's double slit experiment are illustrated numerically taking the spatially and spectrally partial coherent Gaussian Schell-Model Pulsed (GSMP) beam [18].

We have already demonstrated the spectral shifts and switches due to temporal correlation properties of the source using a white light Michelson interferometer in spectral domain in chapter 2. In particular, we have shown that as the optical path difference (OPD) is increased from zero, the output interference spectrum coinciding with the lamp spectrum first shifts towards red splits into two spectral lines of equal intensity and then is blue shifted. The OPD at which the interference spectrum having two peaks of equal intensity is referred as spectral switch position. At this spectral switch position, the spectral peak shift from red to blue or vice versa is very sensitive to the OPD in the interferometer and was used for the measurement of nano-scale displacements with high accuracy and sensitivity [20].

In our earlier studies we observed asymmetry in the spectral shifts at the spectral switch position which changes dramatically with the OPD, possibly due to the PSD of the source. In this chapter we present here a systematic experimental study to investigate the dependence of the spectral switch characteristics on the source PSD characteristics such as the spectral bandwidth ($\Delta\lambda$), peak wavelength (λ_0) and spectral shape due to temporal correlation of the interfering beams in a white-light dispersion-compensated Michelson interferometer (DC-MI). The behavior of the switch position, spectral switch amplitude and symmetry of the spectral switch are studied in detail as a function

of the OPD between the interfering beams. To render our study useful for spectral-domain OCT and singular beam microscopy [21] related research we also present the behavior of the spectral switch amplitude and symmetry of the spectral shifts at the switch position as a function of fractional bandwidth (f_{bw}) of the input spectrum, which is related to the measurement sensitivity and longitudinal resolution of the imaging system. The experimental results were found to match well with the numerical calculations carried out using the interference law in spectral-domain with modified source spectral characteristics.

4. 2. Theoretical background

The spectral interference law for DC-MI is given by

$$S(\lambda) = \frac{1}{2} S_0(\lambda)\{1 + \mathrm{Re}\,[\mu_{12}(\lambda)]\cos[\kappa \Delta l]\} \tag{4.1}$$

Where $S_0(\lambda)$ is the lamp spectrum, $\kappa=2\pi/\lambda$ and Δl is the OPD between the two arms of the interferometer. Re $[\mu_{12}(\lambda)]$ (= 1) is the real part of the complex degree of the spectral coherence. Eq. (4. 1) then becomes

$$S(\lambda) = \frac{1}{2} S_0(\lambda)\{1 + \cos[\kappa \Delta l]\} \tag{4.2}$$

Here $\{1+\cos[(2\pi/\lambda)\Delta l]\} = \{1+\cos(\Delta\phi)\}$ is the spectral modifier function, where $\Delta\phi$ is the phase difference between the interfering beams. The spectral modulations in the output spectrum, $S(\lambda)$ depends on the input spectrum, $S_0(\lambda)$ and the modifier function, $\{1+\cos(\Delta\phi)\}$ which depends on the OPD between the two arms of the interferometer. We use here a general form for the input spectrum ($S_0(\lambda)$) given by the modified Grubner equation [22] to achieve any shape and spectral content.

$$S_0(\lambda) = H \exp\left[-\frac{(\lambda - \lambda_0)^2}{2(\Delta\lambda)^2}\right] g(\lambda) \tag{4.3}$$

Where $g(\lambda) = 1 + \frac{A}{6}\left[\left(\frac{\lambda-\lambda_0}{\Delta\lambda}\right)^2 - 3\left(\frac{\lambda-\lambda_0}{\Delta\lambda}\right)\right] - \frac{C}{24}\left[\left(\frac{\lambda-\lambda_0}{\Delta\lambda}\right)^4 - 6\left(\frac{\lambda-\lambda_0}{\Delta\lambda}\right)^2 + 3\right]$

Where H is the peak height, λ_0 is the peak wavelength of the spectrum, $\Delta\lambda$ is the full width at half maximum (FWHM) spectral bandwidth, A is the asymmetry factor (skewness) and C is the excess. For symmetrical peak shapes like Gaussian, both the skewness and excess are equal to 0.

Using Eq. (4. 3), Eq. (4. 2) can be rewritten as

$$S(\lambda) = \frac{1}{2} H \exp\left[-\frac{(\lambda - \lambda_0)^2}{2(\Delta\lambda)^2}\right] g(\lambda)\{1 + \cos[\kappa \Delta l]\} \qquad (4.4)$$

Eq. (4.4) is used here both to simulate spectra with characteristics of interest in this study and to fit the experimentally generated lamp spectra. As mentioned before, the effect of spectral characteristics on the spectral shifts and switches in the vicinity of the intensity minima due to temporal correlation of the optical fields using a white light MI are studied.

4. 3. Experimental details

The schematic of the experimental setup is shown in Fig. 4.1. It consists of a DC-MI with one of the mirrors (M2) mounted on a nano-positioner (NanoPZ, Newport, USA) capable of linear movement with a minimum step size of 10 nm. The white light source used is a 50 W tungsten-halogen lamp coupled to an optical fiber with a collimating lens at the output. The spectral modifications at the interferometer output are measured using a fiber-coupled spectrometer (SD2000, Ocean Optics, USA). A personal computer is used to control the nano-positioner movement and to acquire the corresponding spectral data from the spectrometer. The spectral characteristics of the white light source measured in the range from 300 – 1000 nm by closing one of the interferometer arms and is fitted using Eq. (4.3) to give a FWHM bandwidth ($\Delta\lambda$) of 238 nm and a peak wavelength (λ_0) of 612 nm. Using these values the coherence length (l_c) of the source is calculated to be 1.57 μm. When the characteristics of the interference spectrum are the same as that of the lamp spectrum the corresponding path

difference between the interfering beams is taken to be zero. The path difference between the two interfering beams is increased using the computer controlled nano-positioner from 0 to 4 μm in steps of 10 nm. The spectral characteristics of the lamp spectrum can be changed using a linear variable filter (LVF) (LVF-HL, Ocean Optics) which is placed in front of the MI as shown in Fig. 4.1. As the LVF is a combination of two coated plates, the desired spectral bandwidth can be obtained by sliding one plate over the other where as the central wavelength can be changed by adjusting the position of the entire LVF with respect to the input beam.

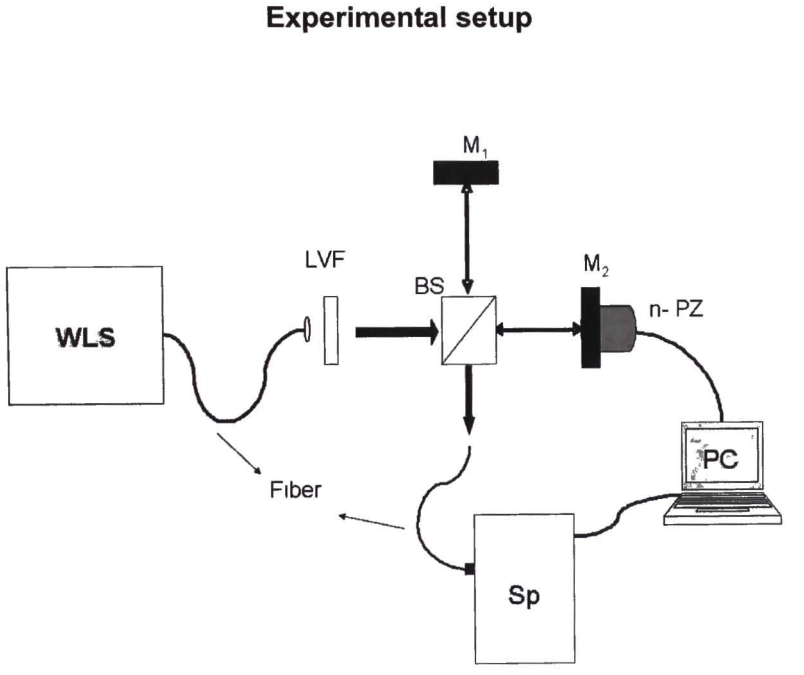

Figure 4.1: *Schematic of the experimental setup. WLS White-light source; BS. 50-50 Beam splitter; M1, M2: Mirrors, LVF: Linear Variable Filter, n-PZ Nano-positioner, Sp: Spectrometer; PC: Personal computer*

4. 4. Results and discussion

The simulated results obtained using Eq. (4.4) and the experimental results using the setup shown in Fig. 4.1 to quantify the effect of important spectral characteristics such as the spectral bandwidth ($\Delta\lambda$), peak wavelength (λ_0) and shape of the input beam on the behavior of the spectral shifts as a function of OPD between the two interfering beams are presented here. The spectral switch characteristics include the spectral switch position, spectral switch amplitude (SSA) and the symmetry characterized by the symmetry parameter (β) at the switch position due to temporal correlation of the input optical fields using the white light DC-MI operated in spectral domain.

4. 4. 1 Effect of Spectral bandwidth ($\Delta\lambda$)

In this section, the dependence of the spectral switch characteristics on the FWHM spectral bandwidth ($\Delta\lambda$) of the input spectrum using the white light DC-MI is investigated. In order to show the effect of the spectral bandwidth($\Delta\lambda$) on the spectral switch characteristics as a function of OPD (Δl) between the interfering beams, Gaussian spectra are simulated using Eq. (4.3) with fixed peak wavelength (λ_0) at 600 nm and varied spectral bandwidth ($\Delta\lambda$) from 10 to 300 nm in steps of 10 nm. For each input spectrum the OPD is increased from 0 to 4 μm in steps of 10 nm and simulated its effect on the output interference spectrum using Eq. (4.4). Normalized spectral shift (NSS) is calculated from the spectral measurements using $\delta\lambda/\lambda_0 = (\lambda_0-\lambda_1)/\lambda_0$ for each OPD, where λ_0 is the peak wavelength of the input spectrum and λ_1 is the wavelength at which the spectral intensity has the maximum value. The simulated NSS results are shown as a 3D plot in Fig. 4.2 as a function of OPD for different spectral bandwidths. Negative and positive values of NSS imply red and blue shift of the spectrum respectively with respect to λ_0 of the input spectrum.

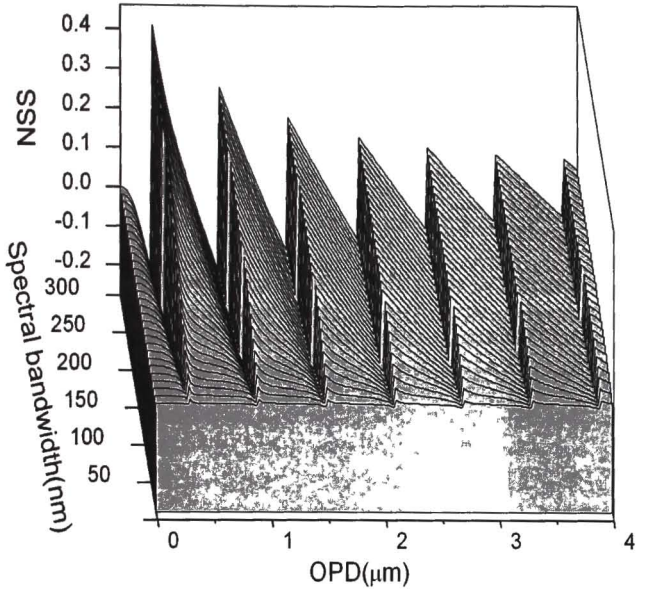

Figure 4.2: *3D plot of the variation of NSS as a function of OPD for the different input spectra with* λ_0 *=600 nm and* $\Delta\lambda$*'s varied from 10 to 300 nm*

The spectral switch amplitude (SSA) is defined in our earlier work as [20]

$$SSA = \{[(\lambda_0 - \lambda_{bluepeak}) / \lambda_0] - [(\lambda_0 - \lambda_{redpeak}) / \lambda_0]\} = (\lambda_{redpeak} - \lambda_{bluepeak}) / \lambda_0 \qquad (4.5)$$

where, $\lambda_{redpeak}$ is the peak wavelength of the spectrum on red-side, $\lambda_{bluepeak}$ is the peak wavelength of the spectrum on blue-side with respect to λ_0 of the original spectrum at the spectral switch position. It is seen from Fig. 4.2 that within the OPD of 0 to 4 μm there are seven spectral switches appearing for all $\Delta\lambda$ values and also the SSA value decreases with increase in the switch number. For the first spectral switch, the switch position is same for all the $\Delta\lambda$ values, SSA value increases and symmetry of the spectral shifts with respect to λ_0 of the input spectrum decreases with increase in the $\Delta\lambda$ value.

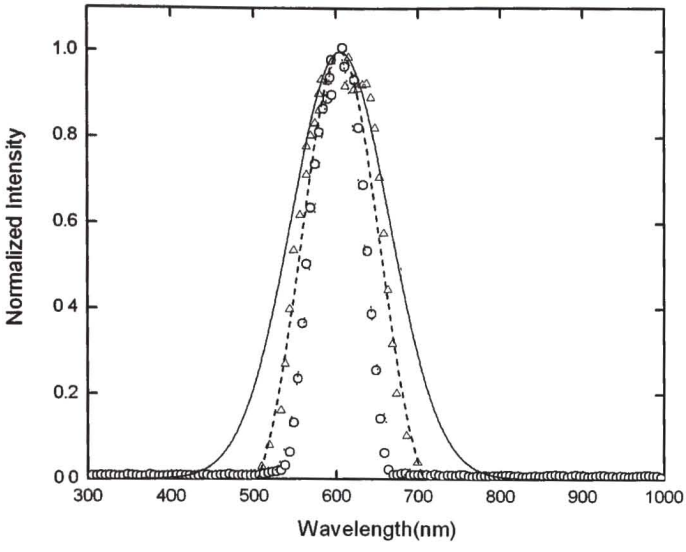

Figure 4.3: *Spectra with different spectral bandwidth (Δλ). Open circle and Dotted line; open triangles and dashed line are experimental and their corresponding Gaussian fits for spectral band widths 50 nm; 100 nm. Continuous line is the computer generated Gaussian spectrum with spectral band width 150 nm using Eq. (4.3).*

To experimentally verify the above results simulated for the Gaussian spectrum of the input beam to study the effect of $\Delta\lambda$ on the spectral switches, the LVF placed at the input end of the DC-MI is adjusted to get a symmetric Gaussian spectrum with λ_0 = 600 nm and different $\Delta\lambda$ values of 50 and 100 nm as shown in Fig. 4.3 (open symbols). As the maximum spectral bandwidth ($\Delta\lambda$) that can be achieved using the LVF is 100 nm we have simulated a Gaussian spectrum (continuous line in Fig. 4.3) with λ_0 = 600 nm and $\Delta\lambda$ = 150 nm using Eq. (4.3). To compare the spectral switch characteristics obtained for the three $\Delta\lambda$ values, 50, 100 and 150 nm, we first choose the spectrum with $\Delta\lambda$ = 50 nm as the input beam and increased the OPD between the interfering beams from 0 to 4 μm in steps of 10 nm using the nano-positioner. For each OPD NSS is calculated as mentioned above. A plot of the variation of NSS as a function of OPD for $\Delta\lambda$ =

50 nm is shown in Fig. 4.4(a). It is seen from Fig. 4.4(a) that within the OPD of 0 to 4 μm seven spectral switches occurred as obtained in our simulations. The measurements are repeated for $\Delta\lambda$ = 100 nm and the results are compared with those of the simulated spectrum of $\Delta\lambda$ = 150 nm. The plots of the variation of NSS as a function of OPD for $\Delta\lambda$ = 100 and 150 nm are shown in Fig. 4.4(b) and (c) respectively. A plot of the variation of switch position as a function of switch number is shown in Fig. 4.5. It is seen from Fig. 4.5 that for each spectral bandwidth the switch position varies linearly with the switch number and the slope of the linear fit is same for all three spectral bandwidths i.e. the spectral switch position for a particular switch number is the same for all the three $\Delta\lambda$ values. The slope of the linear fit measured for the experimental data is calculated to be 0.59 ± 0.003 μm per switch.

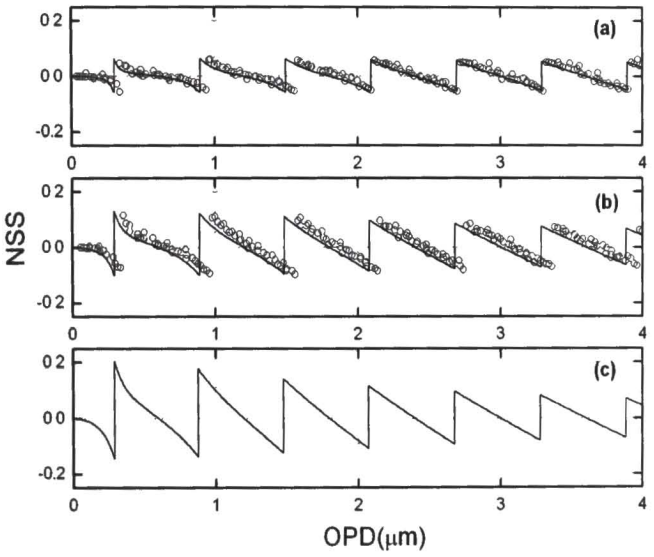

Figure 4.4: *Normalized Spectral Shift (NSS) as a function of OPD for spectral band widths (a) 50 nm (b) 100 nm and (c) 150 nm. Open circles are the experimental data and continuous line is the calculated data using Eq. (4.4).*

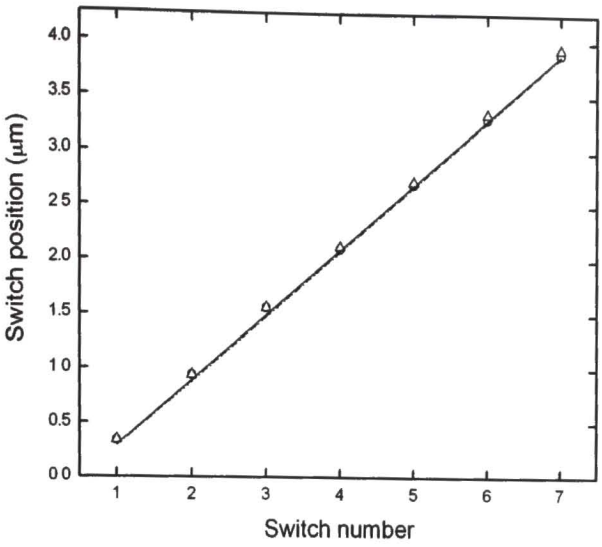

Figure 4.5: *Switch position as a function of switch number for different spectral bandwidth (Δλ) Open circles and dotted line; open triangles and dashed line are the experimental and calculated data using Eq. (4.4) for the spectral band widths 50 nm; 100 nm respectively Continuous line is the calculated data using Eq. (4.4) for Gaussian spectrum with spectral band width 150 nm.*

The spectral switch amplitude (SSA), magnitude of the spectral shift from red side to blue side at the switch position is calculated using Eq. (4.5) for all the three Δλ values. A plot of the variation of SSA as a function of switch number for the Δλ values under investigation is shown in Fig. 4.6. It is seen from Fig. 4.6 that for a fixed Δλ value, SSA value decreases with increase in switch number. This is due to decrease in the effective spectral content of the input beam responsible for the spectral switch with increase in OPD. Also, for a fixed switch number the SSA increases with Δλ due to an increase in the PSD of the input beam.

To illustrate the dependence of the symmetry of the spectral shifts at the spectral switch position on the switch number we define the spectral symmetry parameter β as follows

$$\beta = (\lambda_{red}-\lambda_0) / |(\lambda_{blue}-\lambda_0)| \qquad (4.6)$$

Where, λ_0 is the peak wavelength of the input spectrum, λ_{red} and λ_{blue} are the peak wavelengths on red side and blue side of the spectrum at the spectral switch position.

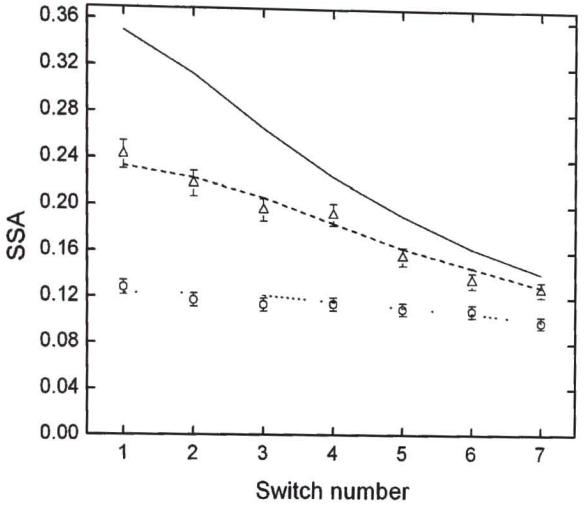

Figure 4.6: *Spectral Switch Amplitude (SSA) as a function of switch number. Open circles and dotted line; Open triangles and dashed line are the experimental data and values calculated using Eq. (4) for $\Delta\lambda$ = 50 nm; 100 nm respectively. The continuous line represents the calculated data for $\Delta\lambda$ = 150 nm.*

When the symmetry parameter is equal to one, the spectral shift at the switch is symmetric, if it is greater than one, the spectral shift is more towards the red side and if it is less than one, the spectral shift is more towards the blue side. Fig. 4.7 shows the variation of the symmetry parameter (β) of the spectral switch as a function of switch number for different $\Delta\lambda$ values. From Fig. 4.7 it can be seen that for the first spectral switch, β decreases with increase in $\Delta\lambda$ value i.e. the asymmetry of the first spectral switch towards blue side increases with $\Delta\lambda$.

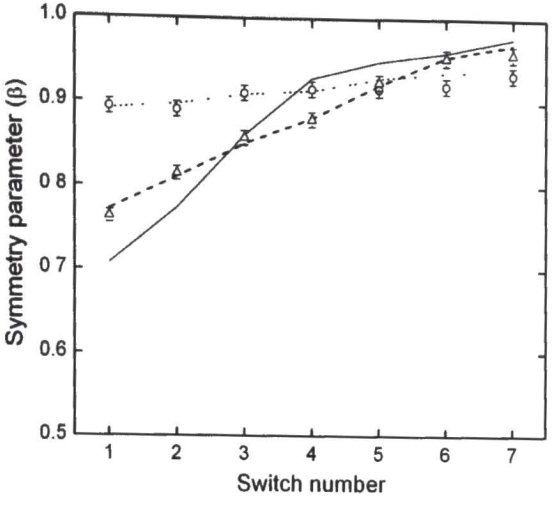

Figure 4.7: *Symmetry parameter (β) of spectral switches as a function of switch number for different Δλ's. Open circles and dotted line, Open triangles and dashed line are the experimental data and calculated data using Eq (4) for the spectral bandwidths 50 nm, 100 nm respectively The continuous line represents the calculated data using the Eq (4) for spectral bandwidth 150 nm.*

To understand the asymmetry of the spectral shifts at the first spectral switch position we calculate the spectral phase as a function of wavelength using the error-compensating five-frame algorithm [23]. Fig. 4.8(a) shows the wrapped spectral phase as a function of wavelength calculated using the five step phase-shifting algorithm. The wrapped phase thus obtained is unwrapped using the algorithm proposed in Ref [24]. The unwrapped spectral phase is plotted as a function of wavelength as shown in Fig. 4.8(b). From Fig. 4.8 it is observed that the spectral phase varies rapidly in the lower wavelength (blue) region than in the higher wavelength (red) region resulting in a large spectral shift and hence the asymmetry towards the blue region than the red region for the same OPD.

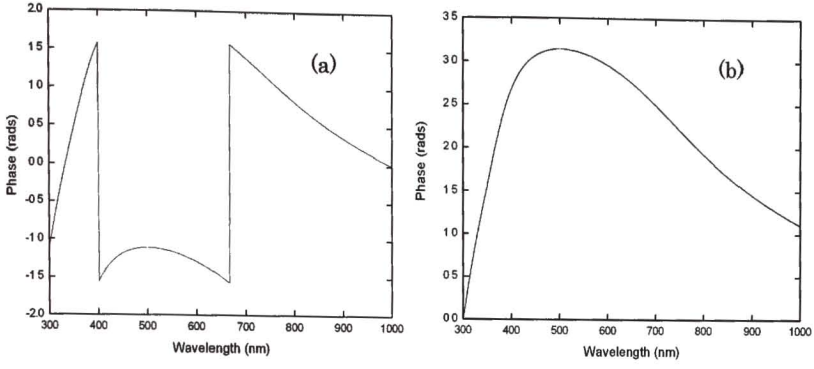

Figure 4.8: *(a) Wrapped spectral phase calculated using five-frame algorithm (b) Unwrapped spectral phase using the algorithm proposed in Ref [24]*

From the above results it can be inferred that increasing the $\Delta\lambda$ value of the input beam increases the SSA and the asymmetry of the spectral switch which have significant importance to increasing the sensitivity of the measurements that rely on the spectral shifts at the switch position [20].

4. 4. 2 Effect of peak wavelength (λ_0)

In this section, the effect of peak wavelength (λ_0) of the input lamp spectrum with fixed spectral bandwidth ($\Delta\lambda$) on the spectral switch characteristics obtained using the DC-MI is studied in detail. To investigate the effect of λ_0, as before Gaussian spectra are simulated with λ_0 varying from 400 to 700 nm for a fixed $\Delta\lambda$ of 50 nm. A 3D plot of the variation of NSS as a function of OPD for different λ_0 values is shown in Fig. 4.9. From Fig. 4.9 it is seen that the number of spectral switches when the OPD is varied from 0 to 4 μm for a fixed $\Delta\lambda$ = 50 nm and for λ_0 = 400 nm is 10 where as it is 6 for λ_0 = 700 nm with OPD and $\Delta\lambda$ remaining the same.

A plot of the variation of number of switches as a function of λ_0 is shown in Fig. 4.10. It is seen from Fig. 4.10 that as λ_0 increases, the switch number decreases within the OPD of 0 to 4 μm. From Fig. 4.9 it is also seen that the slope of the envelope of variation of the switch position decreases with increase in the switch number, implying that the OPD for which a particular switch number occurs increases with the λ_0. The variation of switch position as a function of λ_0 for different switches is shown in Fig. 4.11. For each switch the slope of variation of the switch position with λ_0 is measured and plotted as a function of switch number for the simulated spectra as shown in Fig. 4.12. It is seen from Fig. 4.12 that the variation of the slope increases linearly with switch number for different λ_0's with a slope of $9.98 \times 10^{-4} \pm 7.31 \times 10^{-7}$ per switch.

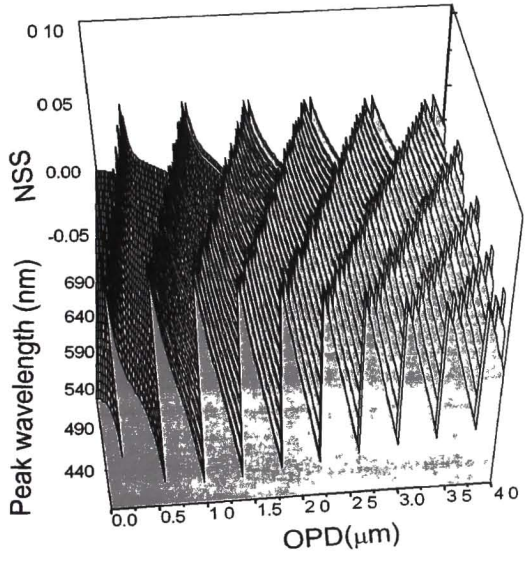

Figure 4.9: *3D plot of the variation of NSS as a function of OPD for different input spectra with* $\Delta\lambda$ *= 50 nm and* λ_0*'s varied from 400 to 700 nm.*

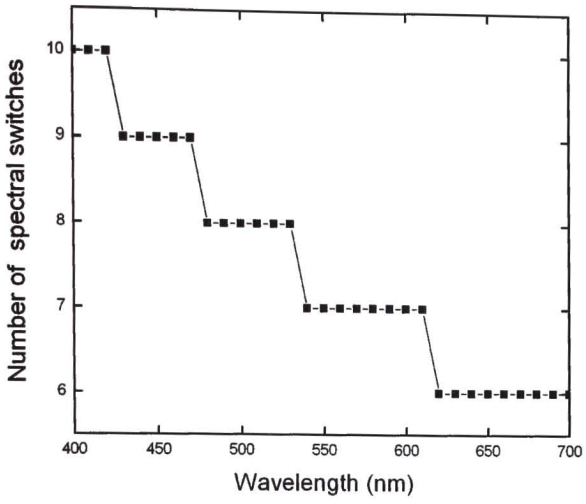

Figure 4.10: *Number of spectral switches as a function of peak wavelength (λ_0)*

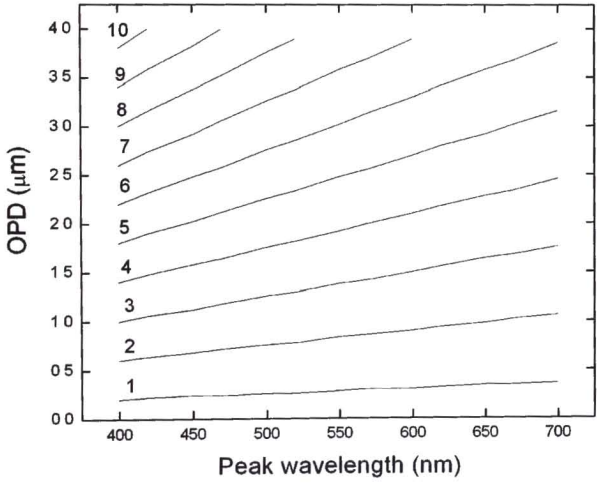

Figure 4.11: *Switch position as a function of peak wavelength (λ_0)*

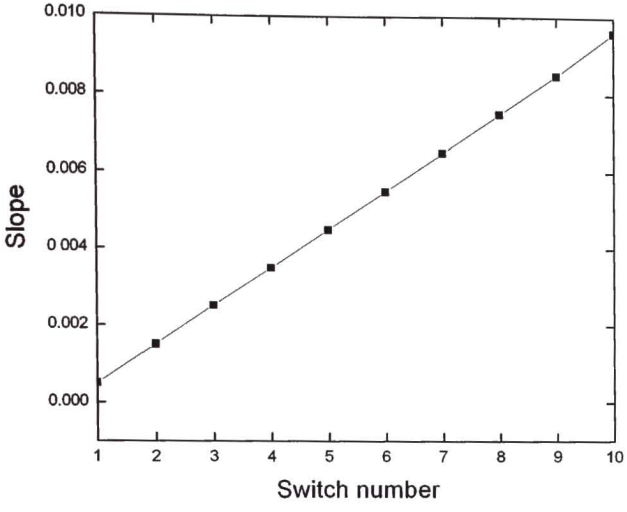

Figure 4.12: *Slope of the variation of switch position with peak wavelength (λ_0) as a function of switch number*

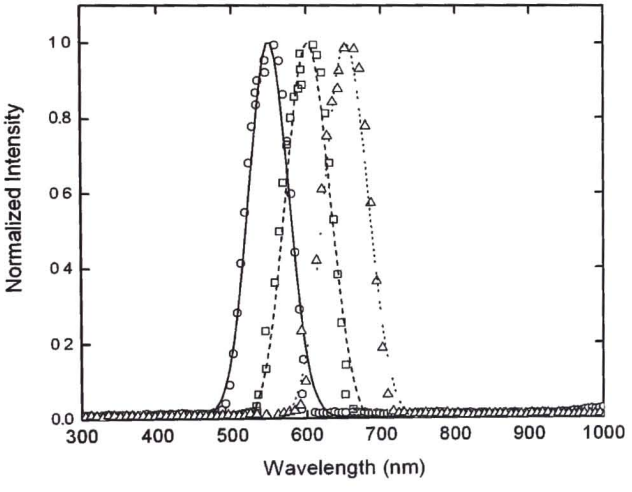

Figure 4.13: *Input spectra with different peak wavelengths. Open circles and continuous line; open squares and dashed line; open triangles and dotted line are the experimental and calculated data using Eq. (4.3) for λ_0 = 550 nm; 600 nm; 650 nm respectively.*

In order to study experimentally the above discussed effect of the variation of switch position, SSA and symmetry parameter with λ_0, we consider three spectra with peak wavelengths λ_0= 550, 600 and 650 nm with all having the same $\Delta\lambda$ of 50 nm as shown in Fig. 4.13. This is achieved by moving the LVF across the input beam for a fixed separation between them. First, the effect of λ_0 on the spectral switch characteristics due to temporal correlation between the interfering beams of the DC-MI is carried out for input spectrum with λ_0= 550 nm. By moving the mirror M_2 to increase the OPD between the interfering beams from 0 to 4 μm in steps of 10 nm using the nano-positioner, NSS is calculated for each step using the equation mentioned in the previous section. The experiment is then repeated for λ_0= 600 and 650 nm. A plot of the variation of NSS as a function of OPD between the interfering arms for different λ_0 values is shown in Fig. 4.14. It is seen from Fig. 4.14 that the number of spectral switches occurred with the observed OPD of 0 to 4 μm is 7, 7 and 6 for λ_0= 550, 600 and 650 nm respectively. It is also seen from Fig. 4.14 that for a particular switch number the switch position increases with λ_0.

In order to show the variation of the switch position with λ_0, we plotted the switch position as a function of switch number for different λ_0 values as shown in Fig. 4.15. From Fig. 4.15 the slopes of the linear fit of the experimental data are measured to be 0.55 ± 0.002, 0.59 ± 0.003 and 0.65 ± 0.002 μm per switch for λ_0 = 550, 600 and 650 nm respectively. The variation of slope of the plot of switch position with switch number for λ_0= 550, 600 and 650 nm is plotted as shown in Fig. 4.16. It is seen from Fig. 4.16 that the slope increases linearly with λ_0 with a slope of $1\text{x}10^{-3}$ ± $1.2\text{x}10^{-4}$ per nm. From these measurements it is observed that as λ_0 increases the separation between the successive spectral switches also increases.

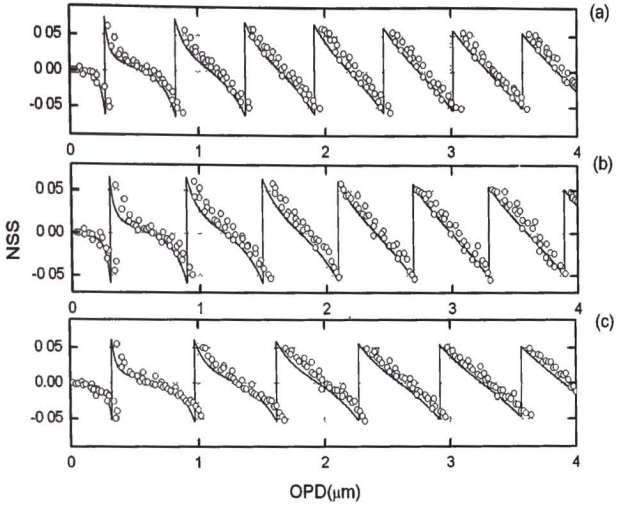

Figure 4.14: *NSS as a function of OPD for peak wavelengths (a) 550 nm (b) 600 nm and (c) 650 nm. Open circles are the experimental data and continuous line is the calculated data using Eq (4.4).*

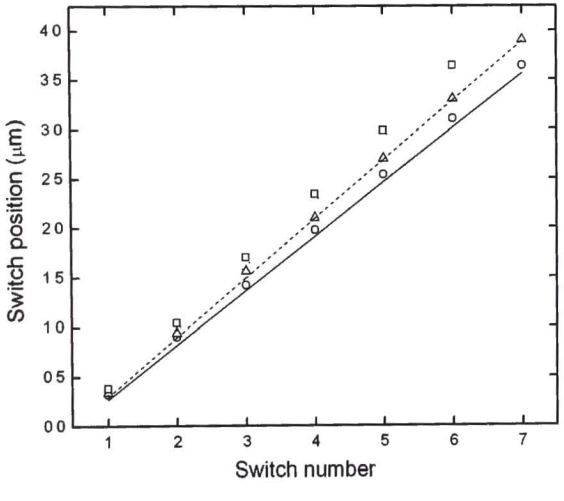

Figure 4.15: *Switch position as a function of switch number. Open circles and continuous line; open squares and dashed line; open triangles and dotted line are experimental and calculated data using Eq. (4.4) for λ_0 = 550 nm; 600 nm; 650 nm respectively.*

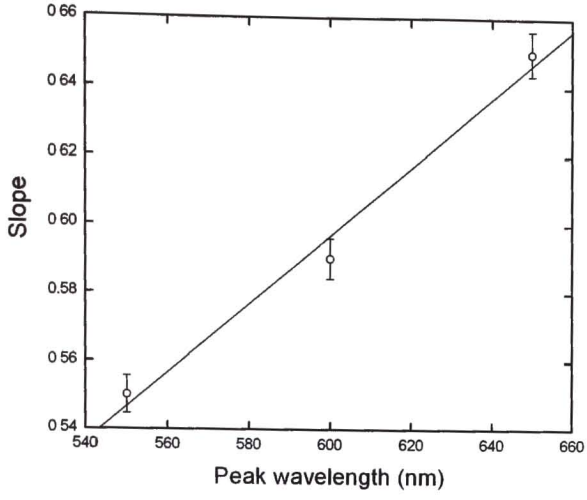

Figure 4.16: *Slope of the variation of switch position as a function of peak wavelength (λ_0). Open circles are the experimental data and continuous line is the linear fit.*

The SSA values at the spectral switch position are calculated using Eq. (4.5) and plotted as a function of switch number for different λ_0 values as shown in Fig. 4.17. From Fig. 4.17, the SSA values for the first spectral switch are 0.14, 0.125 and 0.115 and for the sixth spectral switch are 0.10, 0.09 and 0.09 for λ_0 = 550, 600 and 650 nm respectively. From these measurements it can be observed that the SSA value decreases with increase in the switch number for a particular λ_0. This behavior is attributed as due to decrease in the effective spectral content of the input spectrum contributing to the spectral switch. Also for a particular switch number, the SSA value decreases with increase in λ_0 value and can be attributed to the fact that as λ_0 increases, the spectral content of the input spectrum contributing to the spectral switch is more in the higher wavelength region that has slow variation of the spectral phase as mentioned before. The variation in the SSA values for different λ_0 values is very small with in the observed OPD of 0 to 4 μm in comparison with the SSA values as measured in the previous section.

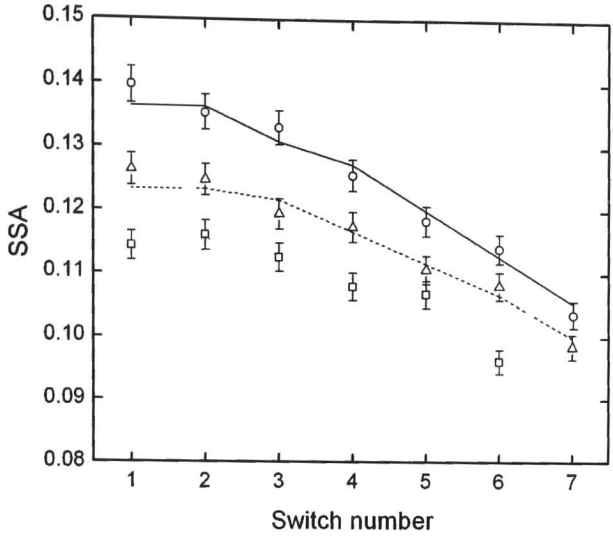

Figure 4.17: *SSA as a function of switch number for different values of λ_0 of the input spectrum Open circles and continuous line; open triangles and dashed line, open squares and dotted line are experimental and calculated data using Eq. (4 4) for λ_0 = 550 nm; 600 nm; 650 nm respectively.*

The symmetry parameter (β) calculated using Eq. (4.6) is plotted as a function of the switch number for different λ_0 values as shown in Fig. 4.18. The β values of the first spectral switch are calculated to be 0.79, 0.85 and 0.88 for 550, 600 and 650 nm respectively implying that the symmetry of the first spectral switch increases with λ_0 for a fixed spectral bandwidth and all of them asymptotically increase to their respective maximum values with increase in switch number. This increase in the symmetry of the first spectral switch with λ_0 is attributed to the slow variation of the spectral phase for the higher λ_0 values.

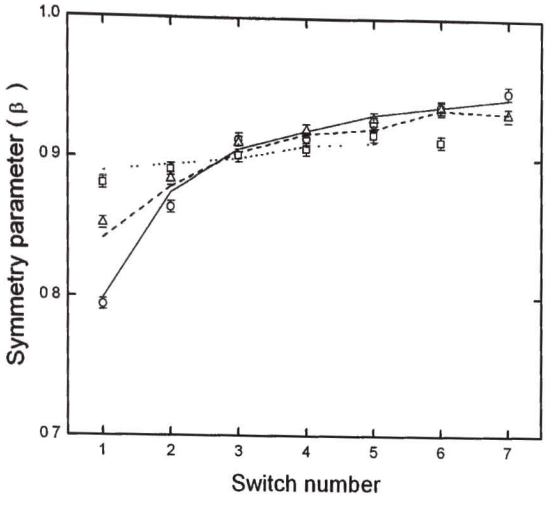

Figure 4.18: *Symmetry parameter (β) as a function of switch number for different values of λ_0 Open circles and continuous line, open triangles and dashed line; open squares and dotted line are experimental and calculated data using Eq. (4 4) for λ_0 = 550 nm; 600 nm, 650 nm respectively.*

4. 4. 3 Effect of spectral shape

In this section, the effect of the input spectral shape on the spectral switch characteristics due to temporal correlation of the interfering beams is demonstrated using DC-MI. To study the effect of spectral shape on the spectral switch characteristics such as switch position, SSA and symmetry parameter, we use a Gaussian spectrum, symmetric with respect to the peak wavelength, the original lamp spectrum and a spectrum with a band pass filter (Kodak, Rochester, USA) as input spectra.

The spectral characteristics of these spectra are shown in Fig. 4.19. Continuous line represents the computer generated Gaussian spectrum using Eq. (4.3), plus symbols represent the original lamp spectrum and Open circles represent the spectrum obtained with filter. The peak wavelength (λ_0) and spectral bandwidth ($\Delta\lambda$) of the spectrum with filter is calculated to be 600 nm and

235 nm respectively. As before to compare the experimental results with the symmetric spectrum, we simulate a Gaussian spectrum with λ_0 and $\Delta\lambda$ the same that of the spectrum with the band pass filter. The characteristics of the original lamp spectrum are λ_0 = 612 nm and $\Delta\lambda$ =238 nm and are compared with that of the two other spectra.

Because skew and excess are unfamiliar quantities to many, Eli Grushka et al [25] calculated those values numerically through easily visualized cases. They have mentioned that the Gaussian, at one end of the spectrum, has zero skew and excess and the bisected Gaussian, the highly asymmetrical half has a skew of 0.995 (Fig. 4.20(a)). By comparison a right angle triangle has the value 0.566. If the Gaussian is divided in to two equal areas by a horizontal cut (Fig. 4.20(b)), the flattened lower half is another good reference and its excess is 1.377. It may also be compared with a square profile, which has the negative value of excess, -1.200.

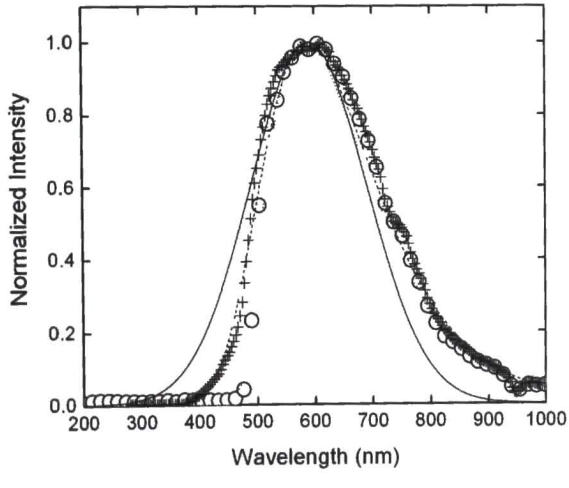

Figure 4.19: *Input spectra with different spectral shapes Open circles are the experimental data using the band pass filter (Kodak, Rochester, USA) and dotted line is corresponding numerical fit using Eq. (4.3); '+' symbols are the original lamp spectrum and dashed line is corresponding numerical fit using Eq. (4.3); continuous line is the computer generated Gaussian spectrum using Eq. (4.3).*

The shape of the different spectra is determined using Eq. (4.3). In Eq. (4.3), for symmetrical peak shapes like Gaussian spectrum, both the skewness (A) and excess (C) are equal to 0. In our case, both the experimentally generated input spectra are fitted to Eq. (4.3) to determine their skewness and excess. For the original lamp spectrum they are 0.2 (A) and -0.45 (C) and for the spectrum with filter they are 0.7 (A) and 0.34 (C) respectively. Dashed line and dotted line in Fig. 4.19 are the theoretical fit for the original lamp spectrum and the filtered spectrum obtained using the Eq. (4.3).

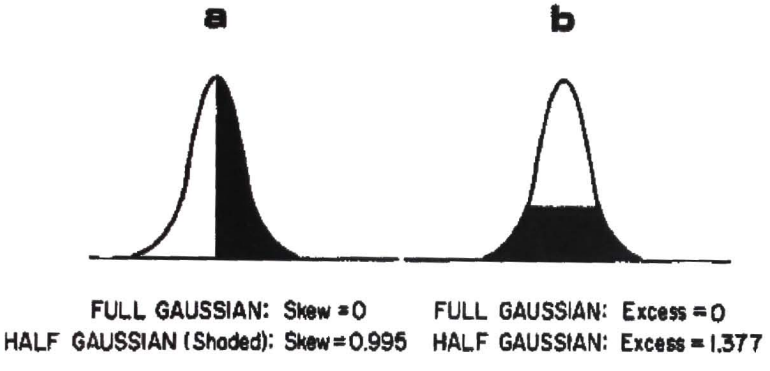

Figure 4.20: *Skew and excess for normal Gaussian peaks and bisected Gaussian peaks*

To compare the spectral switch characteristics due to different shapes of the spectrum, first we consider the simulated Gaussian spectrum and calculated the NSS values and plotted it as a function of OPD as shown in Fig. 4.21(a). Next, the experimentally generated lamp spectrum is used as the input beam to the DC- MI. For each step of the nano-positioner, NSS is calculated and plotted as a function of OPD as shown in Fig. 4.21(b). Fig. 4.21(c) shows the variation of the NSS as a function of OPD for the spectrum with filter as the input beam. In Fig. 4.21, Open circles are the experimental data and dotted line corresponds to the calculated data using Eq. (4.4). It is seen from Fig. 4.21 that the number of switches within the OPD of 0 to 4 μm is 7 for all the input spectra. A plot of the variation of the spectral switch position as a function of switch number is shown

in Fig. 4.22. From Fig. 4.22 it is seen that the switch position is found to vary linearly with the switch number with a slope of 0.59 ± 0.001 μm per switch. Though the λ_0 and $\Delta\lambda$ of the original lamp spectrum is slightly different from the other two spectra, the spectral switch position for a particular switch is almost same for all the three spectra under consideration confirming our results in Section 4.4.1 on the effect of $\Delta\lambda$ on the spectral switches.

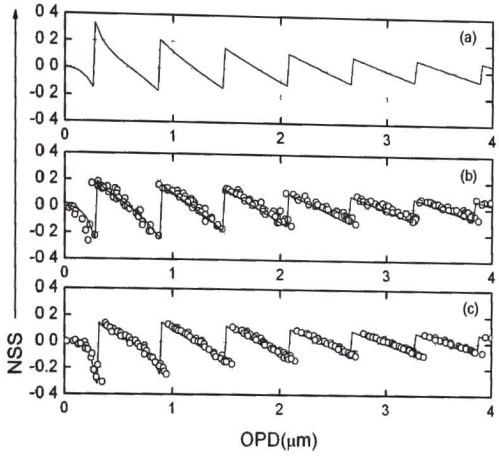

Figure 4.21: *NSS as a function of OPD (a) Gaussian Spectrum (b) original lamp spectrum and (c) using a band pass filter. Open circles are the experimental data continuous line is the calculated data using Eq. (4.4).*

The SSA values at the spectral switch positions are calculated using Eq. (4.5). The variation of SSA values as a function of switch number is shown in Fig. 4.23 and it can be seen that the SSA value decreases monotonically as the switch number increases for all the spectra and the variation in the SSA values for the three different spectra are very small mainly due to the fact that all the three spectra have almost the same spectral bandwidth ($\Delta\lambda$). The decrease in the SSA values for the different spectra is however different from that obtained in the previous sections due to the fact that the $\Delta\lambda$ is much higher in the present case than those in the previous sections.

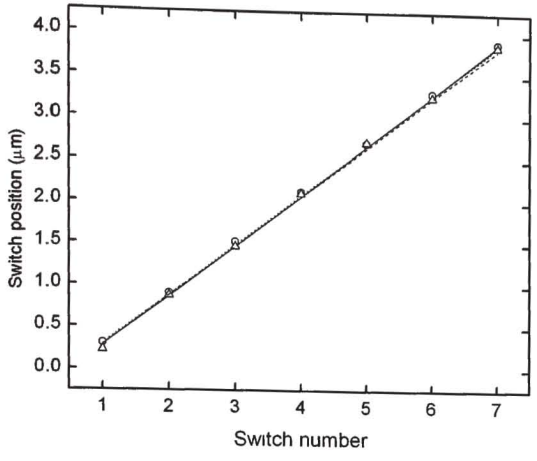

Figure 4.22: *Switch position as a function of switch number. Open circles and open triangles are the experimental data using the spectrum due to filter and the original spectrum; continuous line dotted line and dashed line are the calculated data using Eq. (4) for Gaussian spectrum, original spectrum and the spectrum due to filter respectively*

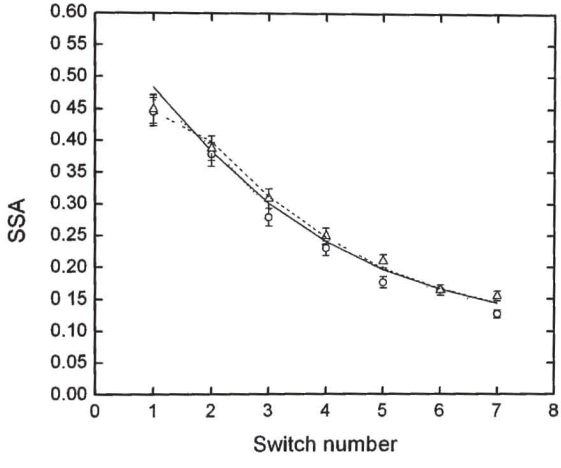

Figure 4.23: *SSA as a function of switch number for different shapes of the input spectrum. Open circles and open triangles are the experimental data with the spectrum using filter and original lamp spectrum. Continuous line, dashed line and dotted line are the calculated data using Eq (4.4) for Gaussian spectrum, original lamp spectrum and the spectrum due to filter respectively.*

The symmetry parameter (β) calculated using Eq. (4.6) at each spectral switch position for the three input spectra is plotted as a function of the switch number in Fig. 4.24. Open triangles and dashed line, open circles and dotted line are the experimental data and the calculated data using Eq. (4.4) for the original lamp spectrum and the spectrum with a band pass filter. The continuous line in Fig. 4.24 is the calculated data for the Gaussian spectrum using Eq. (4.4). It can be seen from Fig. 4.24 that the symmetry parameter, β of the first spectral switch is 0.45 for the Gaussian spectrum, 1.415 for the original lamp spectrum and 2.14 for the spectrum with the band pass filter. These values imply that the first spectral switch is shifted towards blue side for Gaussian spectrum and it is shifted towards red side for the lamp spectrum and the spectrum with band pass filter.

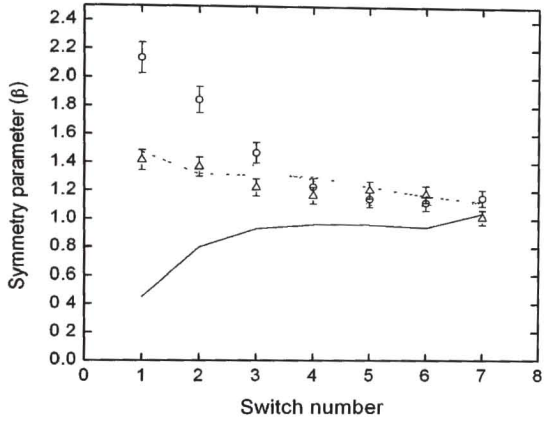

Figure 4.24: *Symmetry parameter (β) as a function of switch number for different shapes of the input spectrum. Open circles and open triangles are the experimental data with the spectrum using filter and original lamp spectrum. Continuous line, dashed line and dotted line are the calculated data using Eq. (4 4) for Gaussian spectrum, original lamp spectrum and the spectrum using filter respectively.*

For the spectrum with band pass filter the first spectral switch shifts a lot towards red side in comparison with that of the lamp spectrum due to higher spectral content in the red side of the spectrum with respect to λ_0. The shift of the spectral switch towards the red side increases with increasing asymmetry of the

input spectrum. As the switch number increases, β approaches to one in all the three cases, implying that the spectral switch attains symmetry for all the input spectra due to decrease in the effective spectral content of the spectrum causing the spectral switch for higher OPDs.

From the results presented in the previous sections, it is seen that the spectral characteristics such as spectral bandwidth ($\Delta\lambda$), peak wavelength (λ_0) and shape of the input spectrum have significant effect on spectral switch characteristics, especially on the switch position, the SSA and the symmetry parameter (β). In order to see the combined effect of the spectral characteristics, we use the fractional bandwidth defined as $f_{bw} = \Delta\lambda/\lambda_0$. It is important to note that this fractional bandwidth plays a critical role in choosing the appropriate spectra to improve the longitudinal resolution [3] of spectral-domain OCT and in singular beam microscopy [21].

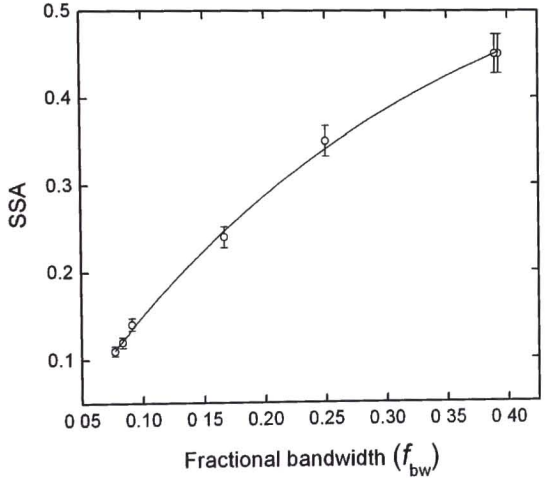

Figure 4.25: *SSA as a function of fractional bandwidth (f_{bw}). Open symbols are the experimental data and the continuous line is an exponential fit using the function SSA = a + b (1-exp (-f_{bw}/c)), where a= -0.08, b=0.6 and c=0.22*

A plot of the variation of SSA as a function of fractional bandwidth is shown in Fig. 4.25. Open circles are the experimental data and the continuous line is an exponential fit obtained using a function of the form SSA = a + b (1-exp ($-f_{bw}$ /c)), where for the best fit, a= -0.08, b=0.6 and c=0.22. From the fit, we also observe that the SSA value saturates at ~ 0.52 for larger values of f_{bw}.

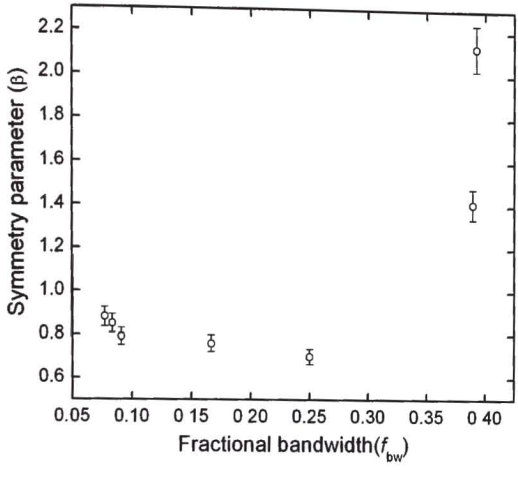

Figure 4.26: *Symmetry parameter (β) variation as a function of fractional bandwidth (f_{bw})*

Next, a plot of the variation of symmetry parameter (β) as a function of f_{bw} is shown in Fig. 4.26; the β value decreases initially and then increases as a function of f_{bw} with a minimum around 0.7 for f_{bw}= 0.25. From these analyses of the measurements we infer that the sensitivity of the spectral-domain interferometer using the SSA increases with f_{bw} whereas the longitudinal resolution of the measurements using coherence length (l_c) decreases with increase in f_{bw}.

4. 5 Conclusions

In this chapter, we present an extensive investigation of the effect of spectral characteristics of the source spectrum on the spectral switch characteristics due to temporal correlation in a DC-MI in the spectral domain. Effect of spectral

bandwidth ($\Delta\lambda$), peak wavelength (λ_0) and shape of the source spectrum on the spectral switch position, spectral switch amplitude (SSA) and symmetry parameter (β) of the switch position are studied in detail and reported here. The SSA value and the asymmetry of the first spectral switch increase with $\Delta\lambda$ for a fixed λ_0 value. For a fixed $\Delta\lambda$ as λ_0 increases, though the variation in SSA is small, the spectral switch position for a particular switch number increases and the asymmetry of the first spectral switch decreases with increase in the λ_0 of the input spectrum. Further, the dependence of the spectral shape on the spectral switch characteristics for a fixed λ_0 and $\Delta\lambda$ of the input spectrum was also studied and we observed that the symmetry of the spectral shifts for a particular switch position depends strongly on the PSD of the source spectrum. To emphasize the applicability of the above measurements for spectral-domain OCT and microscopy, we report on the important trade-off between the sensitivity and longitudinal resolution of the measurement as a function of fractional bandwidth (f_{bw}) of the source.

References

1. D. Huang, E. A. Swanson, C. P. Lin, J. S. Schuman, W. G. Stinson, W. Chang, M. R. Hee, T. Flotte, K. Gregory, C. A. Puliafito and J. G. Fujimoto, Science **254**, 1178 (1991).
2. J. A. Izatt, M. D. Kulkarni, H. Wang, K. Kobayashi and M. V. Sivak, Jr., IEEE J. Sel. Top. Quantum Electron. **2**, 1017 (1996).
3. C. Akcay, P. Parrein and J. P. Rolland, Appl. Opt. **41**, 5256 (2002).
4. J. Kim, C. Choi and K. S. Soh, J. Korean Phys. Soc. **47**, 375 (2005).
5. T. H. Ko, D. C. Adler , J. G. Fujimoto, D. Mamedov, V. Prokhorov, V. Shidlovski and S. Yakubovich, Opt. Express **12**, 2112 (2004).
6. R. Leitgeb, C. K. Hitzenberger and A. F. Fercher, Opt. Express **11**, 889 (2003).
7. J. Pu, H. Zhang, and S. Nemoto, Opt. Commun. **162**, 57 (1999).
8. J. Pu, S. Nemoto, IEEE J. Quantum Electron. **36**, 1407 (2000).
9. J. T. Foley and E. Wolf, J. Opt. Soc. Am. A **19**, 2510 (2002).
10. J. Pu, S. Nemoto, J. Opt. Soc. Am. A **19**, 339 (2002).
11. G. Gbur, T. D. Vesser and E. Wolf, Phy. Rev. Lett. **88**, 013901-1 (2002).
12. E. Wolf, T. Shirai, H. Chen and W. Wang, J. Mod. Opt. **44**, 1345 (1997).
13. T. Shirai, E. Wolf, H. Chen and W. Wang, J. Mod. Opt. **45**, 799 – 816 (1998).
14. T.E. Kiess and R.E. Berg, Am. J. Phys., **64**, 928 (1996).
15. L. E. Helseth, Phys. Rev. E **73**, 026602 (2006).
16. J. Pu, C. Cai and S. Nemoto, Opt. Express **12**, 5131 (2004).
17. C. J. Zapata-Rodríguez, Opt. Commun. **263**, 131 (2006).
18. C. Ding, B. Lü and L. Pan, Opt. Commun. **282**, 413 (2009).
19. M. M. Brundavanam, N. K. Viswanathan and N. R. Desai, Opt. Lett. **32**, 2279 (2007).

20. M. M. Brundavanam, N. K. Viswanathan and D. Narayana Rao, Appl. Opt. **47**, 6334 (2008).

21. B. Spektor, A. Normatov and J. Shamir, Appl. Opt. **47**, A78 (2008).

22. Zs. Pápai and T. L. Pap, Analyst, **127**, 494 (2002).

23. P. Hariharan, B. F. Oreb and T. Eiju, Appl. Opt. **26**, 2504 (1987).

24. M. Takeda, H. Ina and S. Kobayashi, J. Opt. Soc. Am. **72**, 156 (1982).

25. E. Grushka, M. N. Myers, P. D. Schettler and J. C. Giddings, Analytical Chem. **41**, 889 (1969).

CHAPTER 5

Abstract

In this chapter, the generation of white-light filaments in BK7 glass using focused femtosecond pulses is demonstrated experimentally as a function of the input power. We visualize the creation of multiple filaments with gradual increase of laser power by characterizing their spatial distribution of plasma luminescence and corresponding far-field spatial emission pattern. The spectral modulations observed in the output transmission spectrum are used to study the temporal-separation of the filaments during their formation. The experimental observation of the appearance of forklets in the transverse rings present in the far-field spatial emission pattern due to collinear filaments is presented. A simple model using geometrical calculations and interference is presented to understand the basic principle in observing such spatial anomalies.

Spectral interference and spatial anomalies due to multiple filaments in a BK7 glass using femtosecond pulses

5.1 Introduction

Temporal, spatial and spectral properties of a high peak power ultrashort laser pulse are strongly modified during its propagation through a transparent bulk media [1-3]. The primary process responsible for these modifications is self-focusing which causes the laser beam to be compressed in space, resulting in a corresponding catastrophic collapse [4]. This behavior is then balanced by the defocusing effect due to self generated plasma, leading to the formation of a so-called filament [5, 6]. Several scenarios have been proposed to explain the nature of the filamentation process, such as self-channeling model [7], moving focus model [8] and spatial replenishment model [9]. The filamentation process has also been observed in both near IR and UV wavelength regions [10-12]. This filamentation process has been adopted as an attractive way to develop wave guides [13], 3D optical storage and micro fabrication [14] in dielectric solids.

The interaction of intense ultrashort light pulses with matter resulting in the generation of optical radiation over an extremely broad spectral range, which is termed supercontinuum or white-light generation, has been studied extensively [15-16]. This phenomenon of supercontinuum or white-light generation has been observed in a great variety of transparent materials including gases, liquids and solids since the first discovery by Alfano in 1970 [17]. Self-phase modulation (SPM) is considered to be the dominant and triggering mechanism that leads to spectral broadening though it can not explain the complicated spectral characteristics completely. Ionization-induced SPM, four-wave mixing and self-steepening are believed to play roles as well [2, 15, 18].

The connection between white-light continuum emitted from a single filament and self-focusing was firstly discussed by Corkum *et al.* [19]. When the intensity of the focused laser pulses is increased, a group of various filaments are usually observed because of beam splitting. Recently, multiple foci processes have been investigated when a single femtosecond laser pulse was focused into different media [6, 20-24]. Although some spatial information associated with self-focusing can be obtained from these experiments, the complex physics of pulse temporal and spectral evolution during filamentation inside nonlinear dispersive materials are still not well understood. The dynamics of the self-focusing process due to femtosecond laser pulses is strongly affected by the group-velocity dispersion (GVD) of the material [2, 22, 25, 26]. It is found that above a certain threshold power, the laser pulse undergoes temporal splitting which can arrest catastrophic self-focusing using the nonlinear Schrödinger equation in the positive GVD regime. However, it is pointed out that the physical processes responsible for the initial splitting of the input pulse did not necessarily result in multiple splitting [27]. More recently, the generation dynamics of the white-light filaments and the spatial coherence properties of the transverse filaments generated in ZK7 glass using femtosecond laser pulses are studied experimentally [28].

There are several physical processes that contribute to the generation of white-light filaments in condensed matter. SPM enhanced by self-focusing and self-steepening of the pulse are the main causes of the large spectral broadening, but four-wave mixing and Raman scattering also affect the shape and structure of the white-light spectrum. The filamentation process involves a balance between Kerr self-focusing and plasma defocusing. Self-focusing persists until the threshold power for laser-induced plasma is exceeded, increasing the free electron density and reducing the refractive index causing the filament to diverge [29, 30].

5.2 Physics of nonlinear propagation of the ultra-short pulses in optical media

When a powerful femtosecond laser pulse is allowed to propagate through an optical medium, very interesting pattern is observed as shown in the Fig.5.1. Some of the physical processes that contribute to the formation of such pattern during the propagation of the laser pulses through optical media are discussed in this section.

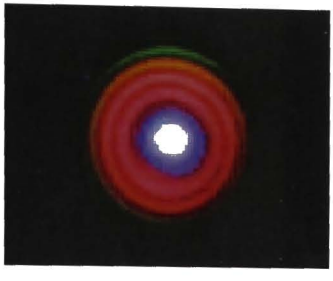

Figure 5.1: *A chirped white light laser pattern from a 5 mJ/45 fs Ti-sapphire laser pulse (at around 800 nm) after propagating a distance of 25m in air (The photograph is taken from Fig 1 (a), Can. J. Phy. **83**, 863 (2005))*

5.2.1 Self-focusing

A collimated laser pulse with a transverse Gaussian distribution in intensity propagating in an optical medium will give rise to an additional intensity dependent nonlinear Kerr index of refraction $\Delta n = n_2 I$ (where n_2 is the second order nonlinear index coefficient and I is the intensity) due to the central part of the pulse having a high intensity. The dominant process responsible for the observed increase in the refractive index is the third order nonlinear susceptibility ($\chi(3)$). As this nonlinear index of refraction is positive in most non-resonant optical materials, the total index of refraction at the central part of the pulse is higher than that at the outer zone. As a result the velocity of propagation, c/n (where c is the velocity of light in vacuum and n the total index of refraction: $n = n_0 + \Delta n$, n_0 being the linear index of refraction) of the central part of the beam

becomes slower than the outer zone. Thus, the wave front of the pulse will curve forward (concave) as it propagates; i.e. it is focusing more and more strongly during the propagation. This is called self-focusing. A non-uniform intensity distribution in the wave front of the pulse and high peak power of the pulse are responsible for self-focusing to occur.

Self-focusing is a threshold process and the laser beam undergoes self-focusing only if the peak power of beam is higher than a critical power Pcr. The critical power for Kerr self-focusing is given by [31]

$$P_{cr} = 3.77\lambda^2/8\pi\, n_0\, n_2 \qquad (5.1)$$

Here λ is the wavelength of the laser, n_0 and n_2 are the linear and nonlinear refractive indices of the medium. It was observed both experimentally [32] and theoretically [33] that the self-focusing of a powerful femtosecond laser pulse is 'slice by slice' self-focusing (moving focus model) rather than whole beam self-focusing during its propagation in optical media. A Gaussian laser pulse having its peak power much higher than the critical power for self-focusing is imagined to be subdivided into many thin slices in time (or in space along the propagation axis as shown in Fig. 5.2). The most powerful slice at the center of the pulse will self-focus first and its intensity becomes higher. This intensity is high enough to partially ionize the optical media, resulting in weak plasma density formation (~ 10^{14} to 10^{16} cm^{-3} for air and 10^{18} cm^{-3} for condensed matter) which would be sufficient to de-focus the focusing slice back to the main body of the pulse or background reservoir [34]. The process responsible for the ionization of the medium is different in different optical media. The primary process responsible for ionization in gases is through tunnel ionization [8]. In condensed matter there are two processes, one is due to multiphoton absorption [35] and the other is due to cascaded or avalanche process [36]. The highest intensity that this self-focusing slice would reach is thus limited due to the balance between self-focusing in the neutral medium and self-defocusing in the self-generated weak plasma. It is called intensity clamping [37-39]. It is a constant that depends on the

material property i.e. it depends on how easy or difficult it is to generate free electrons in the self focal zone.

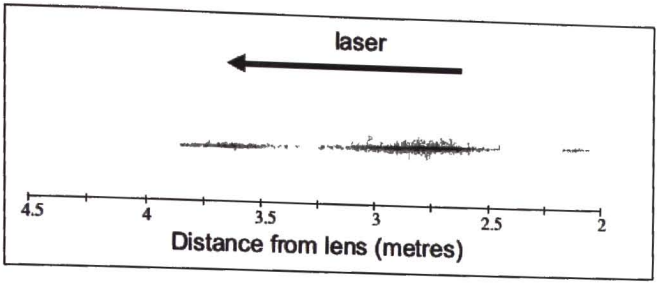

Figure 5.2: *Filament measured in air using an ICCD camera. The filament is produced after a f = 5 m focusing lens. The wavelength of the Ti-sapphire laser pulse was centered around 800 nm; the pulse energy was 13 mJ; the transform limited pulse length was 45 fs (FWHM) The diameter of the filament is of the order of 100 μm. (Picture taken from Fig 2 , Can J Phy 83, 863 (2005)).*

The front slice towards the forward direction and adjacent to the central slice will also undergo the same self-focusing, de-focusing and intensity clamping processes and will return the energy back to the main body of the whole pulse (background reservoir). But as its peak power is lower than that of the central slice, it would self focus at a later position in the propagation direction. This process will continue for successive front slices whose peak powers are higher than the critical power. Thus, the front part of the pulse would become thinner and thinner as the pulse propagates. The back slices symmetrical to the front slices would in principle also self-focus at a position slightly behind the self-foci of the front slices. However, this would never happen because it would encounter the plasma left behind by the central and successive front slices. These back slices would thus interact with the plasma giving rise to a complex intensity distribution [40]. In general, the energy in the back part of the pulse would still be confined inside the whole pulse. During the propagation, the repeated processes of Kerr self-focusing in the neutral medium and self-defocusing in the self generated weak plasma of the various slices in the front part of the pulse result in an extended series of hot spots along the propagation axis resulting in filamentation [32,41-43]. Since the energy loss in the ionization process is small,

the pulse could repeat the whole process again resulting in what we call by self re-focusing [44]. This succession of filaments is manifested by the successive sections of bright lines in Fig. 5.2.

5.2.2 White-light generation

In the self-focal regions, the interaction of the high intensity with the neutral medium and with the plasma results in the modulation of the phase of the pulse, i.e. self-phase modulation (SPM). The consequence of such modulation of the phase is spectral broadening of the output pulse towards both the red and the blue sides with respect to the input frequency. SPM in an optical medium is caused mainly due to the temporal variation of the refractive index. The equations are taken from Physics in Canada, 60, 273 (2004).

In the plane wave approximation, the plane wave front at the self-focus is given by the function

$$F(z,t) = \exp\{i[\omega_0 t - kz]\} = \exp\left\{i\left[\omega_0 t - \frac{\omega_0 n}{c} z\right]\right\} \tag{5.2}$$

Where z is the propagation distance, ω_0 is the central angular frequency of the laser and n is the intensity dependent refractive index, given by [39]

$$n \cong n_0 + \Delta n(t) \tag{5.3}$$

$$\Delta n(t) = n_2 I(t) - \frac{4\pi e^2 N_e(t)}{2 m_e \omega_0^2} \tag{5.4}$$

Here, $n_2 I(t)$ is the Kerr nonlinear refractive index of the neutral medium, I(t) being the intensity. The second term is the plasma contribution where $N_e(t)$ is the electron density generated through tunnel ionization (in gases) or multiphoton ionization (condensed matter) of the medium; e and m_e are the charge and mass of an electron, respectively. Using Eq. (5.3), Eq. (5.2) becomes

$$F(z,t) = \exp\left\{i\left[\left(\omega_0 t - \frac{\omega_0 n_0}{c} z\right) + \int_0^t \frac{\partial}{\partial t}\left(-\frac{\omega_0 \Delta n(t)}{c} z\right) dt\right]\right\} \tag{5.5.1}$$

$$= \exp\left\{ i\left[\left(\omega_0 t - \frac{\omega_0 n_0}{c} z \right) + \int_0^t (\Delta\omega) dt \right] \right\} \tag{5.5.2}$$

Where

$$\Delta\omega = \frac{\partial \phi_{NL}}{\partial t} = \frac{\partial}{\partial t}\left(-\frac{\omega_0 \Delta n(t)}{c} z \right) = -\frac{\omega_0}{c} z \frac{\partial [\Delta n(t)]}{\partial t} \tag{5.6}$$

The modulation (variation) of the phase of the wave due to the self-generated extra nonlinear phase $\phi_{NL} = -\frac{\omega_0 \Delta n(t)}{c} z$ is called SPM. It is manifested by the frequency shift $\Delta\omega$ as shown in the Eq. (5.6). Since the front part of the pulse always sees only the neutral medium (without the plasma contribution), from Eq. (5.6) and (5.4)

$$\Delta\omega = -\frac{\omega_0 z}{c} \frac{\partial [\Delta n(t)]}{\partial t} = -\frac{\omega_0 z}{c} n_2 \frac{\partial I(\textit{front part})}{\partial t} < 0 \tag{5.7}$$

The above inequality (Eq. (5.7)) shows that the front part of the pulse contributes to red (Stokes) shift/broadening due to its positive temporal slope whose value ranges continuously between zero and a maximum. But the trailing part of the pulse should also see some neutral medium since the medium is only slightly ionized. This would lead to a blue (anti-Stokes) shift/broadening but it is masked by the strong blue shift/broadening due to SPM in the plasma together with eventual SPM due to the very steep descent of the back part of the pulse (i.e. self-steepening).

When the plasma is generated at the self-focal zone, it interacts with the self-focusing slice of the pulse and with the slices coming from behind (i.e. from the back part of the pulse). Using Eq. (5.4) and (5.7), the frequency shift/broadening due to the plasma term is

$$\Delta\omega = +\frac{2\pi z e^2}{c m_e \omega_0} \frac{\partial N_e}{\partial t} \tag{5.8}$$

In order to simplify the above expression, experimental results are used to empirically state that the ionization of the medium is proportional to the intensity raised to the power of m, where m is the empirical slope of the experimental ion yield vs. intensity curve [45]. Thus, the electron density can be expressed as [39]

$$N_e \cong N_0 w \int_{-\infty}^{t} I^m(t)dt \tag{5.9}$$

Here N_0 is the density of the neutral medium, w is the effective empirical (tunnel/multiphoton) ionization rate and I^m is the empirical power law of the ionization. Using Eq. (5.9), $\Delta\omega$ can be written as

$$\Delta\omega = +\frac{2\pi z e^2 N_0 w}{c m_e \omega_0} I^m \tag{5.10}$$

This positive blue shift/broadening of the frequency is large because of the highly nonlinear dependence on the high intensity of the pulse inside the self-focal region.

Towards the end of the diffraction length (given by ka_0^2, here k and a_0 are the wave number and the radius of the beam profile at $1/e^2$ level of intensity, respectively) the back part of the intensity distribution of the pulse becomes very steep and the slope is negative. This temporal variation happens mostly in the neutral medium because it is at the end of filamentation where ionization is negligible. This would give rise to a large blue shift of the frequency which can be written in analogy to Eq. (5.7) as

$$\Delta\omega = -\frac{\omega_0 z}{c} n_2 \frac{\partial I(\textit{very steep back part with negative slope})}{\partial t} \tag{5.11}$$

This contributes for the large broadening towards the blue side of the pump frequency. This is so-called self-steepening and can be qualitatively understood as follows. As the central part of the pulse with highest intensity propagates in a medium, its velocity (c/n) is slowed down because of the increase in the index of refraction due to the nonlinear contribution (Kerr nonlinear index) which is proportional to the intensity. The back part of the pulse having a lower

intensity sees the weak plasma whose index of refraction is less than unity. As a result, the back part of the pulse would propagate faster than the peak of the pulse and almost catch up with the peak resulting in a steep rise in intensity at the back part. SPM is proportional to the derivative of this part of the pulse; hence, a very large blue shift will occur according to Eq. (5.11).

It can also be observed from Eq. (5.7) and (5.10) that the propagation distance z also plays a role in both the red and blue broadening. The spectral broadening of the pulse develops progressively as the propagation distance in the medium increases. Both numerical and experimental observations show such broadening [33, 46]. A strong broadening in air towards the red up to 4 microns was also reported [47]. The central part of the pattern of Fig. 5.1 shows such frequency broadening from the pump 800 nm towards the blue side across the whole visible frequency range, hence, it appears white. This is called self transformed white light laser pulse.

5.2.3 Conical emission

The white-light beam generated during filamentation in optical media generally consists of a white central part surrounded by a rainbow-like conical emission (Fig. 5.1). This phenomenon is a signature of filamentation. The colorful rings surrounding the central white spot in Fig. 5.1 are another manifestation of self phase modulation in the radial direction.

During the course of self–focusing of the laser pulse a large gradient of the plasma density arises not only in the longitudinal direction (temporal domain) as discussed in the previous section resulting the SPM in the z-direction but also in the in the transverse (radial) direction. This radial gradient of the plasma density gives rise to spatial SPM which is responsible for the axially symmetric spectral broadening of the angular (spatial) spectrum of the pulse resulting in conical emission. The radial order of the spectral components is inverse of diffraction with bluer frequencies appearing on the outside rings. This can be

understood qualitatively using the wave vector diagram [48] as shown in the Fig. 5.3.

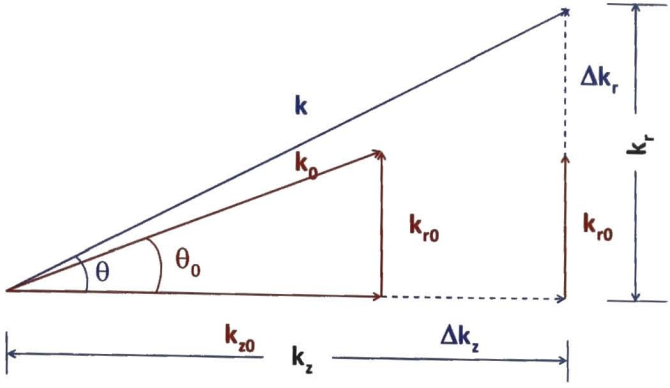

Figure 5.3: Illustration of the conical emission using wave vectors of the pulse. Initial wave vectors before SPM are shown in red color and the change in the wave vectors after SPM are shown in blue color

In Fig. 5.3, $\mathbf{k}_{z0}$ and $\mathbf{k}_{r0}$ are the initial longitudinal and radial wave vectors respectively and θ_0 is the initial small divergence angle (all are shown in red color) before SPM. $\Delta\mathbf{k}_z$ and $\Delta\mathbf{k}_r$ are the change in the initial wave vectors and θ is the angular shift due to SPM. $\mathbf{k}_0$ and $\mathbf{k}$ are the resultant wave vectors before and after SPM respectively. The relation between the above wave vectors (from Fig. 5. 3) related to the divergence angle of the conical emission is given by

$$\begin{aligned}
&\mathbf{k}_z = \mathbf{k}_{z0} + \Delta\mathbf{k}_z \\
&\mathbf{k}_r = \mathbf{k}_{r0} + \Delta\mathbf{k}_r \\
&\mathbf{k}_0 = \mathbf{k}_{z0} + \mathbf{k}_{r0} \\
&\mathbf{k} = \mathbf{k}_z + \mathbf{k}_r \\
&\theta_0 = k_{r0}/k_{z0} \\
&\theta = k_r/k_z = k_{r0}/k_z + \Delta k_r/k_z \cong \theta_0 + (\Delta k_r/k_z)
\end{aligned} \tag{5.12}$$

The increase in the width of the angular spectrum, Δk_r (where k_r is the radial wave number) due to the plasma is proportional to the absolute value of the radial

derivative of the electron density [49], i.e. $\Delta k_r = |(\partial/\partial r)N_e(r)|$. The angular spectral broadening comes from the same leading part of the pulse which gives rise to spectral blue shifting as in the case of temporal SPM. This radial part of the radiation experiences strong blue shift $\Delta\omega$ (which is proportional to the radial electron density in analogy to Eq. (5.7)) with simultaneous angular shift $\theta = \theta_0 + (\Delta k_r/k_z)$ as defined in Eq. (5.12). Qualitatively, in the plasma, the divergence of the radiation is due to the negative nonlinear contribution to the refractive index, unlike the case of Kerr medium where the nonlinear contribution to the refractive index is positive. The stronger is the plasma induced nonlinear interaction; the larger will be the divergence and spectral blue shifting. As a result, shorter (anti-stokes) wavelengths predominantly propagate at larger angles. The cone angle of each color is independent of the position along the filament and no conical emission is observed on stokes side input wavelength [49].

Though the physics of self-focusing and filamentation in condensed matter is same as that in air, the free electron generation process is different and that the filament length in all experiments reported to date is also much shorter. The free electron generation process in condensed matter is through the excitation of electrons from the valence to the conduction bands followed by inverse Bremsstrahlung and partial cascaded ionization [33, 35, 36]. Also, the pulse duration is too short to allow for a full breakdown. The electron density is estimated to reach 10^{18} cm^{-3} and is three orders of magnitude lower than the atomic density of condensed matters. Intensity clamping, self-phase modulation [39], conical emission and self-steepening [50] are identical in condensed matter.

The filament length in condensed matters is shorter compared to air due to the fact that the electron density generated in condensed matters is more than two orders of magnitude higher than that in air. This higher electron density causes much large energy loss during propagation of the pulse. Hence the peak power of the pulse would quickly go below the critical power for self-focusing and limits

the filamentation process. Another reason is probably that the critical power for self-focusing is lower (~ a few MW) than that in atmospheric air (~3-6 GW).

5.3 Experimental details

The laser system used in this work is a commercially available diode-pumped mode-locked Ti: Sapphire Laser purchased from *Spectra Physics Inc.* The laser system consists of (i) oscillator unit producing high repetition rate, nJ, fs pulses, *Mai-Tai* and (ii) regenerative amplifier producing amplified fs pulse, *Spitfire* [51]. The schematic view of the laser system is shown in the Fig. 5.4. The *Mai Tai* comprises of two lasers: a cw diode-pumped laser and a mode-locked Ti: Sapphire pulsed laser. It delivers a ~ 80 fs, 82 MHz pulse train with pulse energy of 1 nJ. The output spectrum from Mai Tai is shown in Fig. 5.5 (a).

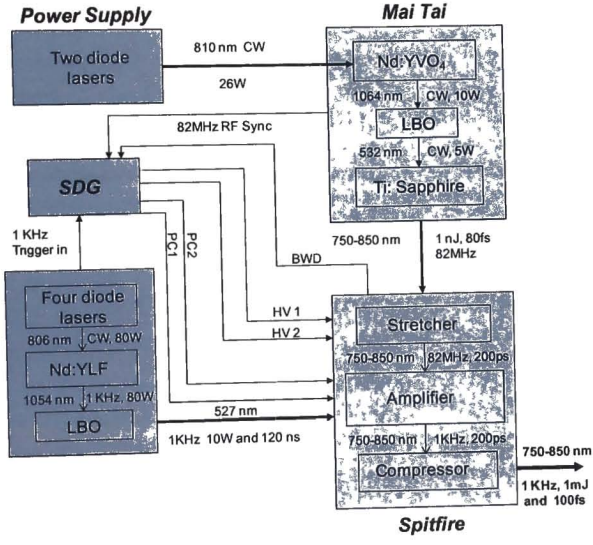

Figure 5.4: *Schematic of the femtosecond laser system*

As the output energy of the oscillator is of the order of nJ, an amplifying unit, *Spitfire*, is used to amplify the energy without introducing much temporal broadening. *Spitfire* is a regenerative amplifier (RGA) system that employs the conventional chirped pulse amplification (CPA) technique. The RGA is

pumped by the powerful nanosecond pulses (~10 W) from *Evolution*. *Spitfire* delivers amplified pulses of 100 fs of a maximum of 1mJ average energy at a repetition rate of 1 kHz. The output beam diameter from the *Spitfire* is 9 mm with a spectral bandwidth 9.4 nm and peak wavelength at 800 nm as shown in Fig. 5.5(b). The output pulse from the spitfire is characterized by intensity autocorrelation experiment and found that it is Fourier transform limited Gaussian pulse.

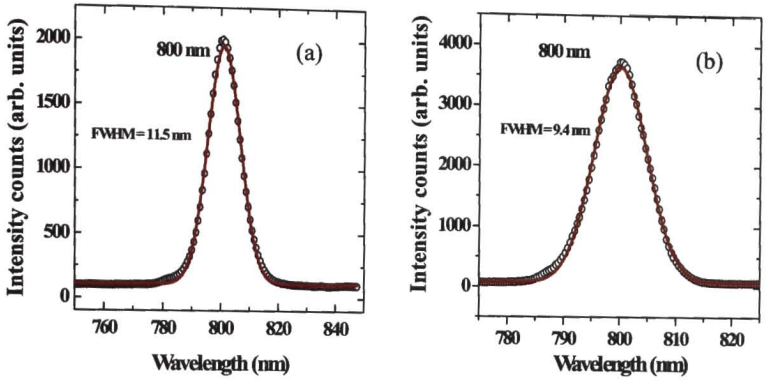

***Figure 5.5**: a) Mai Tai output spectrum, (b) Spitfire output spectrum*

The general and most important characteristics of the fs laser used for the present studies are summarized in Table 5.1.

Characteristics of fs laser	***Mai Tai***	***Spitfire***
Pulse-width	~82 fs	~100 fs
Max output energy	1 nJ	1 mJ
Rep. rate	80 MHz	1kHz
Beam diameter	3 mm	9 mm
Polarization	Horizontal	Horizontal

***Table- 5.1:** Summary of laser output characteristics of fs laser system used*

5.3.1 Experimental setup

The experimental setup used for the observation of collinear filaments formed in the bulk of BK7 glass is depicted in Fig 5.6. Femtosecond laser pulses (λ = 800 nm, repetition rate = 1 KHz, pulse width = 100 fs) after passing through a variable attenuator (VA) consisting of a half-wave plate and a polarizer are focused using a lens L_1 (f = 10 cm) into the bulk of a polished BK7 glass block (dimensions: 1x1x0.5 cm) fixed on a translation cum rotation stage. The beam diameter of the focal position is estimated to be 50 μm.

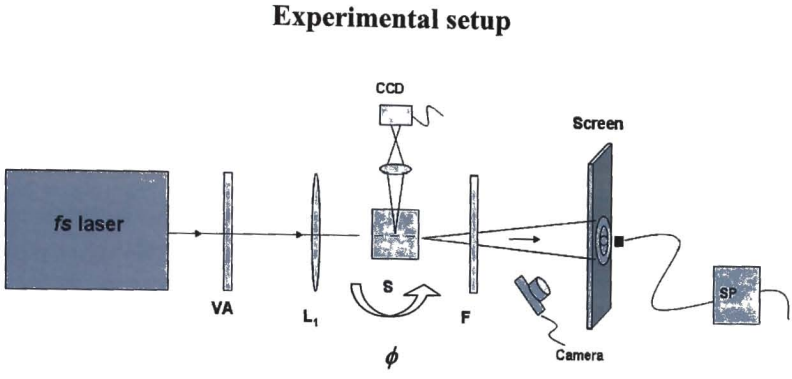

Figure 5.6: *Schematic of the experimental setup VA Variable attenuator, L_1: focusing lens, S: BK7 glass Sample, F: filter for 800 nm, SP: Spectrometer, ϕ: angle of the incident laser with respect to the sample*

The spatial distribution of white-light filaments formed inside the bulk of BK7 is imaged from the plasma luminescence by a CCD camera (Thorsight) fixed above the sample stage. The transmission spectrum of white-light filaments out of the glass sample is measured through a fiber coupled spectrometer (Ocean Optics, SD2000) connected to a personal computer. A high reflection dielectric mirror for 800 nm is inserted as a spectral filter to block the transmitted fundamental beam. A white screen is placed around 30 cm from the sample to capture the far-field conical emission pattern using a digital camera. The filaments formed in the sample, the spatial profile of the far-field emission

pattern and the spectral characteristics of the supercontinuum generated are all measured simultaneously for both normal and tilted incidence of the input beam as a function of the laser peak power.

5.4 Results and discussion

The experiment is first performed to investigate the generation of filaments during the nonlinear propagation of femtosecond laser pulses through the BK7 glass sample. In order to observe the white-light filaments, the femtosecond pulses should undergo self-focusing which depends on the power of the input laser. The threshold power for the self focusing to be started is termed as critical power (P_{cr}) and is defined as shown in Eq. (5.1). In our present case the critical power for self focusing in the BK7 glass (n_0 = 1.511and n_2 = 3x 10^{-16} cm^2/W [52]) is calculated to be ~ 2.2 MW. When the power of the input laser is set low enough than P_{cr}, white-light filaments can not be found inside the medium. The CCD images of the spatial distributions of the plasma luminescence of the filaments, far-field spatial emission pattern and corresponding transmission spectra for different input powers are shown in figures 5.7, 5.8 and 5.9 respectively.

When the input laser power is increased to $2.21P_{cr}$, a single short filament is formed inside the medium as shown in the Fig. 5.7(a). The length of the filament is estimated to be around 1mm. A typical snapshot of the far-field spatial emission pattern from the single short filament is shown in the picture of Fig. 5.8(a). From Fig. 5.8(a) it can be seen that the far-field emission pattern due to the filament contains a circular spot. The transmission spectrum of the single filament at this power is shown in Fig. 5.9(a). With gradual increase of laser power, the single short filament brightens and its far field-emission pattern seems to be enhanced as well. However, the length of this single filament is observed to remain almost same. When the input power is increased to $3.83P_{cr}$, we observe that the single filament is moved towards the laser as shown in Fig. 5.7(b). The corresponding far-field spatial emission pattern is shown in Fig. 5.8(b). From Fig.

5.8(b) it can be seen that the central spot is surrounded by an annular conical ring of red light which can be due to the diffraction of the light by the local modification of the refractive index of the medium during the filamentation process.

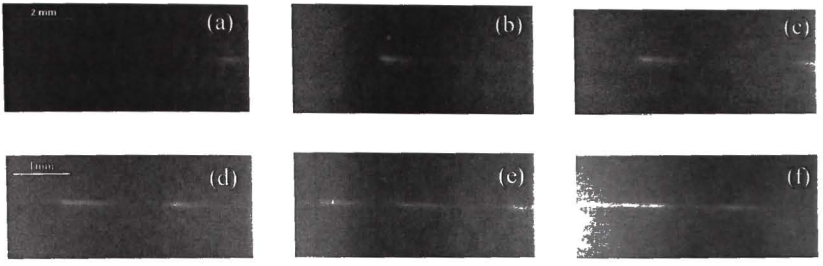

Figure 5.7: *CCD images of the plasma luminescence due to refocusing filaments in BK7 glass at different input laser power.*

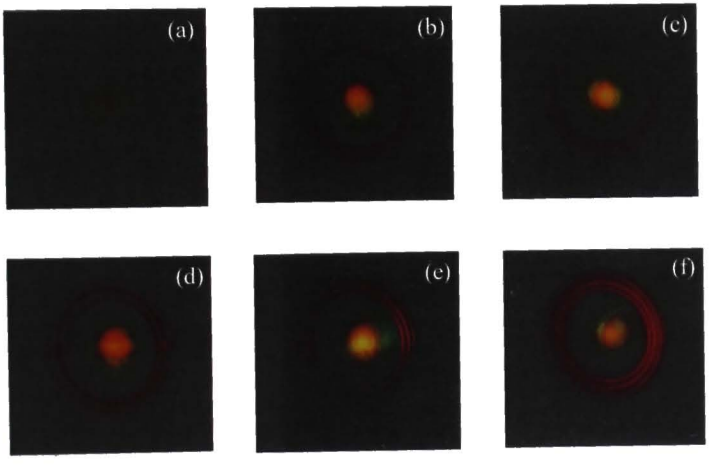

Figure 5.8: *Far-field spatial emission pattern due to refocusing filaments in BK7 glass at different input laser power.*

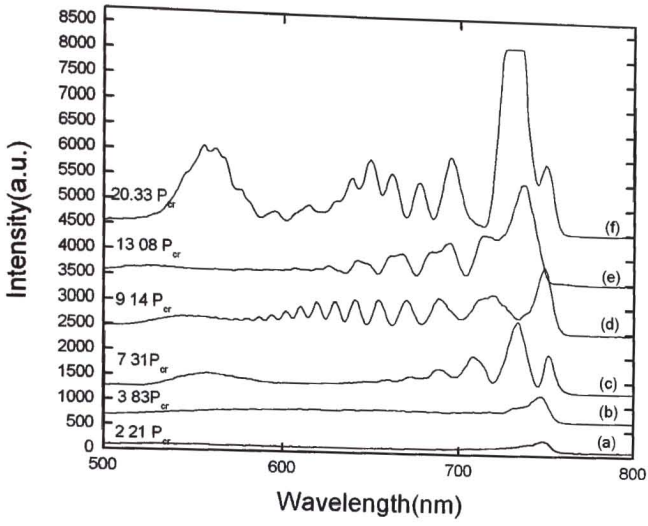

Figure 5.9: *Output transmission spectra at different input laser powers*

When the input laser power is increased up to $7.31P_{cr}$, the formation of the second short filament is observed, which is in accord with the simple self-focusing model [8]. The length of the plasma luminescence of the two distinct collinear filaments (Fig. 5.7(c)) is identical and they are almost same. This observation suggests that the higher laser power would make the beam undergo refocusing events instead of a simple extending of the original filament length. The far-field spatial emission pattern corresponding to the two collinear filaments (Fig. 5.7(c)) is shown in Fig. 5.8(c) in which the central white-spot and the conical emission are more evident and also it is clear from Fig. 5.8(c) that the conical emission consists of more annular rings. The transmission spectrum corresponding to the two collinear filaments due to refocusing of the input laser is shown in Fig. 5.9(c). It can be seen from Fig. 5.9(c) that the white-light continuum is spectrally broadened towards the shorter wavelengths with respect to the wavelength of the input laser. Also periodic spectral modulations are

observed in the transmission spectrum, identical to the spectral modulations observed in the conventional spectral interference using a white-light source [53].

From Fig. 5.9(c), though the spectrum is broadened towards the shorter wavelengths the spectral modulations are observed only up to 650 nm which can be due to the fact that the white-light continua generated by the two filaments can be different, i.e. the white-light continuum generated by the first filament can be more broader than the second filament resulting in the limited spectral modulations. The difference in the spectra of the two filaments can be due to the difference in the distribution of the power in each filament at low powers [54]. More detailed experiments and explanation on the spectral modulations in the spectrum are presented in the subsection 5.4.1. The production of multiple refocusing filaments can be visualized with progressively increased laser power as shown in the Fig. 5.7(d)-5.7(f). Corresponding far-field spatial emission patterns are shown in Fig. 5.8(d)-5.8(f) respectively. The annular rings in the far-field spatial emission pattern are more visible and the thickness of the each ring increases with input laser power. When the input laser power is $20.33P_{cr}$, it can be seen that all the multiple refocusing filaments are fused together as shown in the Fig. 5.7(f). Corresponding far-field spatial emission pattern and corresponding output transmission spectrum is shown in Fig. 5.8(f) and 5.9(f) respectively. It can be observed from the Fig. 5.9(f) that the spectral modulations are disappeared and the spectrum is arbitrary.

5.4.1 Spectral interference of the white-light continuum due to filaments

In the output transmission spectra from the glass sample for slightly high powers, we observe spectral modulations as shown in the figures 5.9(c) and 5.9(f) respectively. These spectral modulations are due to the spectral interference of the white-light continuum generated during the formation of the collinear refocusing filaments. These modulations in the spectrum are identical to the spectral modulations obtained due to the mutual coherence of the supercontinuum

pulses collinearly generated in bulk media by phase-locked and time delayed intense laser pulses [54].

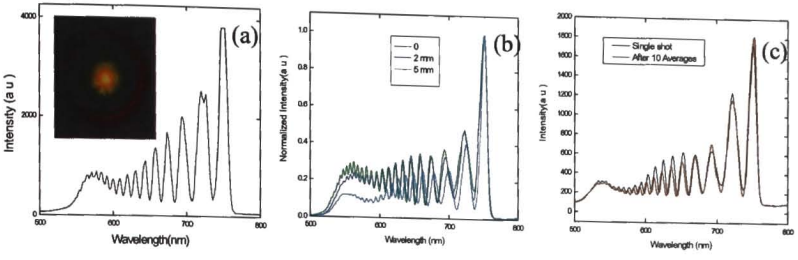

Figure 5.12: *Spectral modulations for the input laser power 11 36P_{cr}*

In Fig. 5.12(a) the spectral modulations obtained for the input power of 11.36P_{cr} and the far-field spatial emission pattern (inset) are shown. Fig. 5.12(b) shows the change in the spectral modulations across the central spot of the far-field spatial emission pattern. This can be done by moving the fiber tip from the center to the edge of the central spot. It can be seen from the Fig. 5.12(b) that the spectral modulations in the shorter wavelength side becomes weaker at the edge of the central spot in comparison with the spectral modulations at the center of the central spot. In Fig. 5.12(c) we have shown the spectra corresponding to the single and 10 averages of the output spectrum after the illumination of the laser on to the glass sample. The two spectra are almost identical except for the shorter wavelengths where the spectral modulations became weaker could be due to the fluctuations in the input laser power.

In order to study these spectral modulations, we consider the output transmission spectra for different input laser powers 8.39P_{cr}, 9.04P_{cr}, 10.9P_{cr} and 13.45P_{cr} as shown in the Fig. 5.13. It can be seen from Fig. 5.13 that as the input power increases the spectral modulations increases towards the shorter wavelength side. At higher powers the spectral periodic modulations become progressively weaker and we get arbitrary spectra. In Fig. 5.13 the spectral

modulations are doubled for the power $13.45P_{cr}$ due to the interference of the white-light continua of the three refocused filaments.

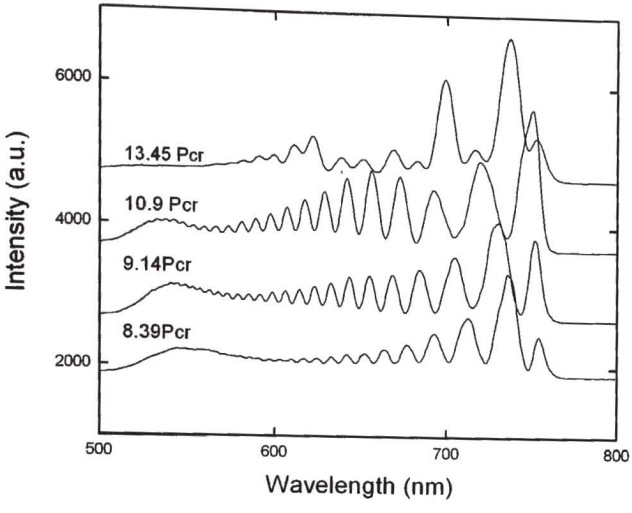

Figure 5.13: *The output transmission spectra for different input laser powers*

The change in the spectral modulations in the output transmission spectrum with the input power is due to the change in the temporal interval between the refocusing filaments. Since the BK7 glass in our experiment serves as the nonlinear dispersive medium, the characteristic spectral modulations in the measured spectrum can be understood as a result of the temporal splitting of the single pulse. Above a certain threshold power the presence of a small amount of positive GVD causes the splitting of the original input pulse into two temporally separated pulses away from the pulse center [25, 26]. The two generated continua sources, separated in time interfere with each other to form the spectral modulations and the period of these spectral modulations are inversely related to the temporal separation of the pulses. As these changes in the spectral modulations with input power are identical to the spectral modulations produced due to the time delayed supercontinuum pulses generated in the bulk media using a Michelson interferometer configuration [54] we can calculate the temporal

separation between the collinear refocusing filaments. In order to measure the temporal separation of the pulses, first we measure the fringe period ($\delta\lambda_{fp}$) of the spectral modulations in the higher wavelength region (around 750 nm) and lower wavelength region (around 600 nm). From these fringe periods we calculate the temporal separation using [54]

$$\tau = \frac{\lambda^2}{c\delta\lambda_{fp}} \tag{5.13}$$

Where τ is the temporal separation between the filaments due to refocusing of the input laser power, c is the velocity of light and $\delta\lambda_{fp}$ is the fringe period of the spectral modulations. Fig. 5.14 shows the variation of the fringe period ($\delta\lambda_{fp}$) as a function of input power. Open circles and open squares are the experimental data for 600 nm and 750 nm wavelength regions respectively. From Fig. 5.14, it can be seen that the fringe period increases linearly with input power. The temporal separation of the refocusing filaments calculated using Eq. (5.13) is plotted as a function of input laser power as shown in the Fig. 5.15. Open circles and open squares are the experimental data for 600 nm and 750 nm regions respectively. It can be seen from Fig. 5.15 that the temporal separation decreases with increase in input laser power in both 600 nm and 750 nm regions and it becomes same for both regions at higher input laser powers.

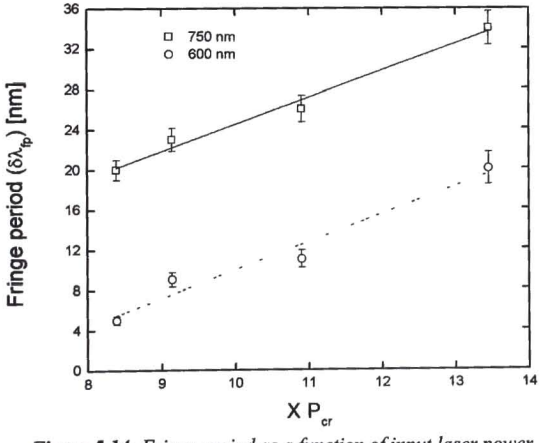

Figure 5.14: *Fringe period as a function of input laser power*

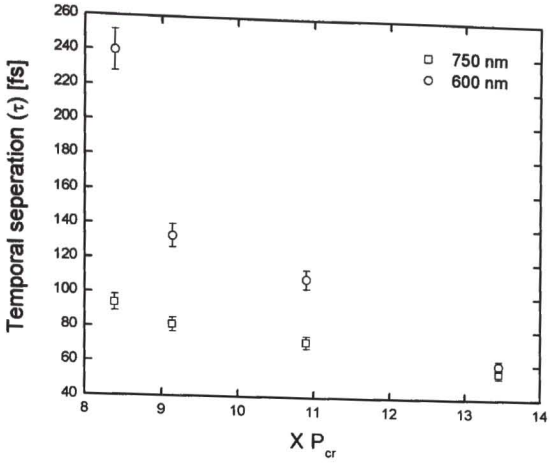

Figure 5.15: *Temporal separation between the refocusing filaments as a function of input laser power*

5.4.2 Spatial anomalies present in the far-field spatial emission pattern

The power of the input laser is adjusted to $15P_{cr}$ which results in the three filaments. The far field emission pattern (inset), corresponding transmission spectrum for $\phi \sim 0^0$ is shown in Fig. 5.10(a). The CCD image of the plasma luminescence of the three filaments is shown in the Fig. 5.10(b). The line profile of the multiple refocusing filaments is also shown in Fig. 5.10(b). At the same input power, the glass sample is rotated through an angle $\phi \sim 2^0$ with respect to the input laser. The spatial emission pattern and corresponding CCD image of the multiple filaments due to refocusing of the laser pulse are shown in the Fig. 5.11. From Fig. 5.11(a), it is observed that the color of the fringes has become more prominent and there are some discontinuities in the annular rings of the conical emission and form like 'forklets'. These forklets in the annular rings of the conical emission are manifestation of the wave front dislocations or optical vortices or phase singularities in the optical field produced by the collinear filaments.

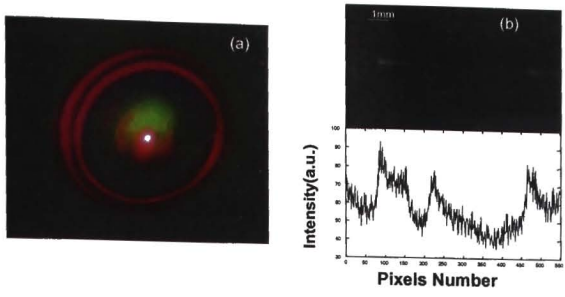

Figure 5.10: *(a) Far-field spatial emission pattern for the power around $15P_{cr}$ (b) CCD image of the refocusing filaments and corresponding line profile for $\phi \sim 0^0$.*

These discontinuities or forklets are treated as spatial anomalies. Fig. 5.12 shows the line profile of the regions (1) and (2) as shown in Fig. 5.11 (a). It can be observed from Fig. 5.12 that the fringes in the region (1) are π phase shifted with respect to the region (2) which results in spatial anomalies. As these forklets or spatial anomalies observed in our experiments are identical to the temporal correlation vortices observed in the polychromatic fields [55] and the fork like fringes observed due to the interference of the sheared waves [56], the formation of the forklets or spatial anomalies in the annular rings of the conical emission could be due to the shear in one of the wave fronts of the collinear filaments. It can also be observed from Fig. 5.11(a) is that the discontinuities are occurring only on one side of the annular rings could be due to the asymmetric shear of the wavefront of one of the filaments.

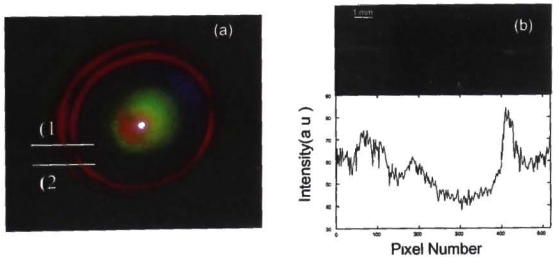

Figure 5.11: *(a) Far-field spatial emission pattern (inset) and corresponding output transmission spectrum; (b) CCD image of the refocusing filaments and corresponding line profile for $\phi \sim 2^0$*

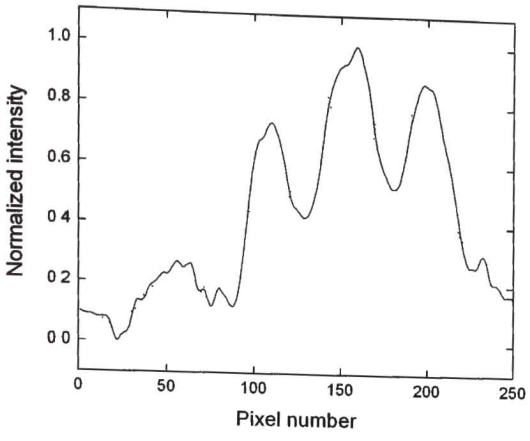

Figure 5.12: *Line profile of the regions (1) and (2) of Fig. 5 11(a). Solid line is for the region (1) and dashed line is for the region (2).*

A simple model using geometrical calculations and interference is proposed to explain the spatial anomalies observed when the glass sample is rotated through an angle with respect to the input beam. The schematic of the picture for the three filament interference when the sample is rotated through an angle is shown in the Fig. 5.13.

As the distance between the three filaments is very small, it is assumed that the shearing of the wave fronts coming from the nearest filaments is coinciding exactly same and the spatial anomalies are occurred due to the shearing of the third wave front. The rings formed in the far-field emission are resulted in due to the interference of the conical emission from different filaments. The spatial anomalies or forklets observed in the far field emission pattern are due to the shearing of the wavefronts of the filaments. Due to shearing, the wavefront is not exactly circle but is slightly elliptical depending on the shearing angle. The shape of the wavefront is described as a locus of points on the surface of a cone making an angle with respect to the circular wave front. A simple geometrical calculation is used to demonstrate the spatial anomalies observed. Fig. 5.14 shows the pictorial demonstration of the shape of the wavefront tilted at an angle with respect to the base of the cone.

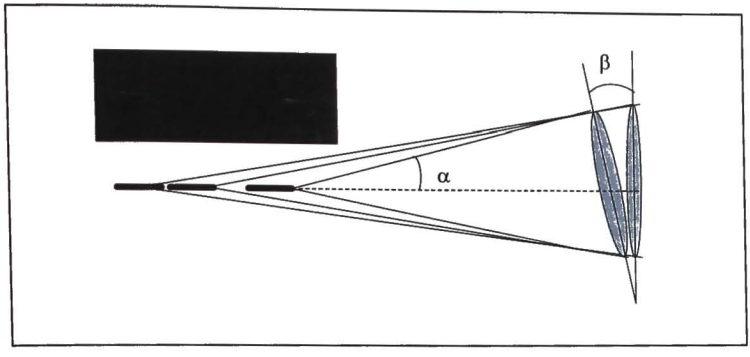

Figure 5.13: *Schematic of the three filament interference when the sample is rotated through an angle ~ 2^0. Inset also shown the original picture of the three filaments when the sample is rotated through an angle ~ 2^0*

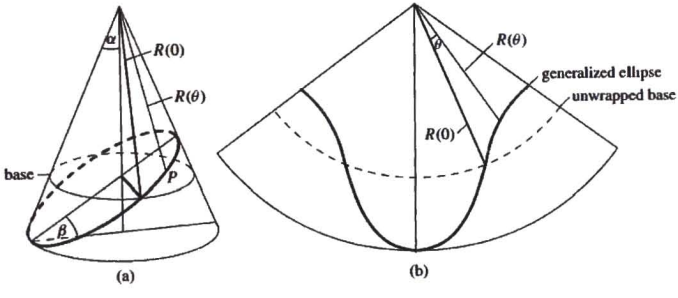

Figure 5.14: *(a) An elliptical cross section (b) its unwrapped image on a plane (Figure is adopted from Fig.15 of Ref [57])*

The polar equation of the cross section of a cone is governed by the equation [57]

$$R(\theta) = \frac{R(0)}{1 + \lambda \sin(k\theta)} \tag{5.16}$$

Where $\lambda = \tan\alpha \tan\beta$, α is the half-vortex angle and β is the tilt of the wave front with respect to the base of the cone, k = 1/sinα. Here in our case the half vortex angle α is found to be equal to 15^0 From Fig. 5.14(a), P is a point on the

elliptical cross section, R(θ) is the variable distance on the elliptical cross section from the vortex of the cone. R(0) is the distance from the vortex to the intersection of the circular base and the elliptical cross section, in our case it is the distance between the filaments, and is around 1 mm. Fig. 5.14(b) shows the unwrapped image of the cone on a plane.

We use MATLAB to simulate the interference of the wavefronts due to shearing. The simulations are done without considering the dispersion effects. Fig. 5.15 shows the computer generated picture when the tilt of the wave front is zero where we have not observed any spatial anomalies in the far-field emission pattern. In the simulations we have fixed the planes of the two wave fronts and rotated the third wave front. Fig. 2 shows the computer generated interference pattern with three waves, in which one of the waves is sheared through an angle 2^0 corresponding to the change in the OPD of 5 nm. From Fig. 5.15 it can be seen that we observe spatial anomalies in the interference similar to those of the far-field emission pattern shown in Fig. 5.11

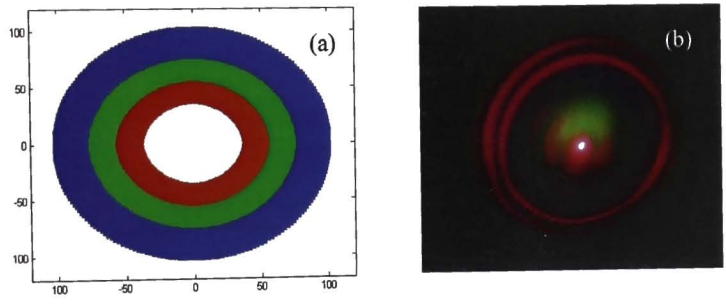

Figure 5.15: *(a) Computer generated picture for the interference of three filaments when the wave fronts are not tilted. (b) Experimentally observed far-field spatial emission pattern*

Though the simulated picture using computer calculations is slightly different from the experimental observations, the simulation shows the basic principle to understand the spatial anomalies present in the far field emission

pattern. Here in our simulations we have taken only three colors to ease our calculations.

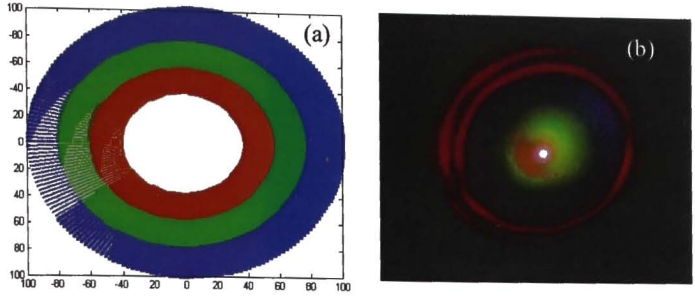

Figure 5.15: *(a) Computer generated picture for the interference of three filaments when the wave fronts are rotated through an angle 2^0 (b) Experimentally observed far-field spatial emission pattern.*

In order to investigate the effect of the tilt we simulated the picture by changing the value of β corresponding to the wave front tilt of 6^0 corresponds to the OPD of around 15 nm. We observe the complex picture with increased number of spatial anomalies as shown in the Fig. 5.16.

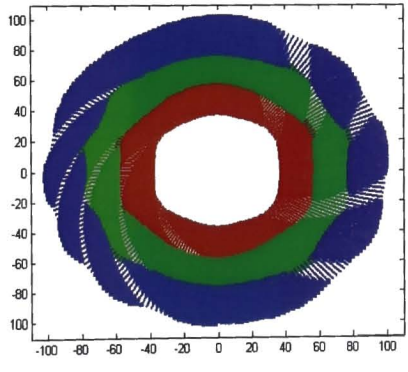

Figure 5.16: *Computer generated picture for the interference of three filaments when the wave fronts are rotated through an angle 6^0*

5.5 Conclusions

In this chapter, experimental observation of the generation of refocusing filaments in BK7 glass using femtosecond laser pulses is presented. The plasma luminescence, far-field spatial emission pattern and corresponding output transmission spectra are recoded as a function of the input laser power. The spectral modulations observed in the output transmission spectra for different input laser powers are studied to estimate the temporal separation of the refocusing filaments based on the fringe period calculations. The experimental observation of the spatial anomalies observed in the transverse rings of the far-field spatial emission pattern due to multiple filaments due to refocusing of the input laser pulse are presented. A simple model is proposed using geometrical calculations and interference to understand the observed spatial anomalies.

References

1. H. Kumagai, S. Cho, K. Ishikawa, K. Midorikawa, M. Fujimoto, S. Aoshima and Y. Tsuchiya, J. Opt. Soc. Am. **20**, 597 (2003).
2. D. Von der Linde and H. Schuler, J. Opt. Soc. Am. **13**, 216 (1996).
3. D. Faccio, P. Trapani, S. Minardi, A. Bramati, F. Bragheri, C. Liberale, V. Degiorgio, A. Dubietis and A.Matijosius, J.Opt. Soc. Am. **22**, 862 (2005).
4. R. Y. Chiao, E. Garmire and C. H. Townes, Phys. Rev. Lett. **13**, 479(1964).
5. L. Sudrie, A. Couairon, M. Franco, B. Lamouroux, B. Prade, S. Tzortzakis and A. Mysyrowicz, Phy. Rev. Lett. **89**,186601 (2002).
6. Z. Wu, H. Jiang, H. Yang and Q. Gong, J. Opt. A: Pure Appl. Opt. **5**, 102 (2003).
7. A. Braun, G. Korn, X. Liu, D. Du, J. Squire and G. Mourou, Opt. Lett. **20**, 73 (1995).
8. A. Brodeur, C. Y. Chine, F. A. Ilkov, S. L.Chin, O. G. Kosareva and V. P. Kandidov, Opt. Lett. **22**, 304 (1997).
9. M. Mlejnek, E. M. Wright and J. V. Moloney, Opt. Lett. **23**, 382 (1998).
10. A. Couairon and L. Berge, Phys. Rev. Lett. **88**, 135003 (2002).
11. A. Saliminia, S. L. Chin and R. Vallée, Optics Express **13**, 5731 (2005).
12. A. Couairon, L. Sudrie, M. Franco, B. Prade and A. Mysyrowicz, Phys. Rev. B **71**, 125435 (2005).
13. E. Miura, J. Qiu, H. Inouge, T. Mitsayu and K. Hirao, Appl. Phys. Lett. **71**, 3329 (1997).
14. E. N. Glezer, M. Milosavljevic, L. Huang, R. J. Finlay, T. H. Her, J. P. Callan and E. Mazur, Opt. Lett. **21**, 2023 (1996).
15. A. Dharmadhikari, F. Rajgara and D. Mathur, Appl. Phys. B **80**, 61 (2005).
16. N. T. Nguyen, A. Saliminia, W. Liu, S. L. Chin, R. Vallee, Opt. Lett. **28**, 1591 (2003).
17. R. R. Alfano and S. L. Shapiro, Phys. Rev. Lett. **24**, 584 (1970).

18. S. Tzortzakis, L. Sudrie, M. Franco, B. Prade and A. Mysyrowicz, Phys. Rev. Lett. **87**, 213902 (2001).
19. P. B. Corkum, C. Rolland and T. Srinivasan-Rao, Phy. Rev. Lett. **57**, 2268 (1986).
20. Z. Wu, H. Jiang, L. Luo, H. Guo, H. Yang and Q. Gong , Opt. Lett. **27**, 448 (2002).
21. W. Liu, S. L. Chin, O. Kosareva, I. S. Golubtsov and V. P. Kandidov, Opt. Commun. **225**, 193 (2003).
22. Z. Wu, H. Jiang, Q. Sun, H. Yang and Q. Gong, Phys. Rev. A **68**, 063820 (2003).
23. S. Juodkazis, V. Mizeikis, E. Gaizauskas, E. Vanagas, V. Jarutis, H. Misawa, L. Bohn and S. Golubev, Proc. SPIE **6063**, 6053R (2006).
24. A. Q. Wu, I. H. Chowdhury and X. Xu, Appl. Phys. Lett. **88**, 111502 (2006).
25. J. K. Ranka, R. W. Shcirmer and A. L Gaeta, Phys. Rev. Lett. **77**, 3783 (1996).
26. J. E. Rothenberg, Opt. Lett. **17**, 583 (1992).
27. A. A. Zozulya, Phys. Rev. Lett. **82**, 1430 (1999).
28. J. Yang and G. Mu, Optics Express **15** 4943 (2007).
29. K. Cook, A. K. Kar and R. A. Lamb, Optics Express **13**, 2025 (2005).
30. A. L. Gaeta, Phys. Rev. Lett. **84**, 3582 (2000).
31. J. H. Marburger, Prog. Quantum Electron. **4**, 35 (1975).
32. A. Brodeur, C.Y. Chien,; F. A. Ilkov, S. L. Chin, O. G. Kosareva, V. P. Kandidov, Opt Lett. **22**, 304 (1997).
33. V.P. Kandidov, O.G. Kosareva, I.S. Golubtsov, W. Liu, A. Becker, N. Akozbek, C.M. Bowden and S.L. Chin , Appl. Phys. B **77**, 149 (2003).
34. V P Kandidov, O G Kosareva and A A Koltun, Quantum Electron. 33, 69 (2003).
35. A. Brodeur and S. L. Chin, Phys. Rev. Lett. 80, 4406 (1998).
36. A. Brodeur and S. L. Chin, J. Opt. Soc. Am. B 16, 637 (1999).
37. J. Kasparian, R. Sauerbrey and S. L. Chin, Appl. Phys. B 71, 877 (2000).

38. A. Becker, N. Aközbek, K. Vijayalakshmi, E. Oral, C.M. Bowden and S.L. Chin, Appl. Phys. B **73**, 287 (2001).
39. W. Liu, S. Petit, A. Becker, N. Aközbek, C. M. Bowden, S. L. Chin, Opt. Commun. **202**, 189 (2002).
40. N. Aközbek and C. M. Bowden, Phys. Rev. E **61**, 4540 (2000).
41. O. G. Kosareva, V. P. Kandidov, A. Brodeur and S. L. Chin, J. Nonlinear Opt. Phys. Mater. **6**, 485 (1997).
42. M. Mlejnek, E. M. Wright, J. V. Moloney, Opt. Lett. **23**, 382 (1998).
43. A. Chiron, B. Lamouroux, R. Lange, J.-F. Ripoche, M. Franco, B. Prade, G. Bonnaud, G. Riazuelo and A. Mysyrowicz, Eur. Phys. J. **D6**, 383 (1999).
44. A. Talebpour, S. Petit and S. L. Chin, Opt. Commun. **171**, 285 (1999).
45. A. Talebpour, J. Yang and S. L. Chin, Opt. Commun. **163**, 29 (1999).
46. N. Aközbek and C. M. Bowden and S. L. Chin, J. Mod. Opt. **49**, 475 (2002).
47. J. Kasparian, R. Sauerbrey, D. Mondelain, S. Niedermeier, J. Yu, J-P Wolf Y-B. André, M. Franco, B. Prade, S. Tzortzakis, A. Mysyrowicz, M. Rodriguez, H. Wille, L. Wöste, Opt. Lett. **25**, 1397 (2000).
48. S. L. Chin, A. Brodeur, S. Petit, O. G. Kosareva and V. P. Kandidov, J. Nonlinear Opt. Phys. Mater. **8**, 121 (1999).
49. O. G. Kosareva, V. P. Kandidov, A. Brodeur, C. Y. Chien and S. L. Chin, Opt. Lett. **22**, 1332 (1997).
50. A. L. Gaeta, Phys. Rev. Lett. **84**, 3582 (2000).
51. Spectra-Physics Inc. operation manuals for Mai-Tai™ and Spitfire™.
52. M. Falconieri, E. Palange, and H. L. Fragnito, J. Opt. A: Pure Appl. Opt. **4**, 404 (2002).
53. D. Narayana Rao, V. Nirmal Kumar, J. Mod. Opt. **41**, 1757 (1994).
54. C. Corsi, A. Tortora and M. Bellini, Appl. Phys. B **77**, 285 (2003).
55. V. P. Ryabukho and D. V. Lyakin, Optics and Spectroscopy **98**, 273 (2005).
56. G. A. Swartzlander and J. Schmit, Phys. Rev. Lett. **93**, 093901 (2004).
57. T. M. Apostol and M. Mnatsakanian, MONTHLY, **114**, 388 (2007).

CHAPTER 6

Conclusions & Future perspectives

6.1 Conclusions

So much literature available on the spectral anomalies such as spectral shifts and spectral switches around the singular phase points due to diffracted waves of spatially coherent polychromatic light. These spectral anomalies are due to either spatial coherence induced or diffraction induced effects. In the present thesis, we presented the temporal coherence induced spectral anomalies (spectral shifts and spectral switches) around the intensity minima of the output spectrum due to white-light illuminated Michelson interferometer operated in the spectral domain. When the OPD is increased from zero, where the output spectrum coincides with the input white-light spectrum, the spectrum shifts towards red splits into two spectral lines of equal intensity and then is blue shifted. The output spectrum with two peaks of equal intensity is referred as 'spectral switch'. At spectral switch position the spectral intensity at wavelength corresponding to lamp spectral maximum is zero. In order to measure the spectral shifts quantitatively, we define normalized spectral shift (NSS) as $\delta\lambda/\lambda_0 = (\lambda_0 - \lambda_1) / \lambda_0$, where λ_0 is the lamp spectrum maximum and λ_1's are the wavelength at which the spectral intensity has the highest value. Zero value of the NSS corresponds to the output spectrum resembling with the input lamp spectrum. If the NSS value is negative then the spectrum is red shifted and if it is positive then the spectrum is shifted to blue side with respect to the input peak wavelength. Also it is observed an unusual behavior in the number of spectral maxima with in the input lamp spectral bandwidth when the OPD is increased in steps of 10 nm.

It was noticed during our experiments that the spectral shifts around the spectral switch position are highly sensitive to the displacement of one of the mirrors M_2 of the Michelson interferometer. These spectral shifts around and crossing through the spectral switch can be used to measure the nano displacements. We propose two methods to measure the nano-displacements. The

first method deals with the spectral switch with the spectrum having two spectral fringes which occurs within the coherence length (l_c) of the source. The second method is demonstrated using the spectral switch with the spectrum having nine fringes which occurs far away from the coherence length of the source. To measure the nano displacement we define spectral switch amplitude (SSA) which is defined as the magnitude of the rapid transition around and crossing the spectral switch position which is different for different displacements of the mirror M_2. Once the SSA values are calculated for different displacements of the mirror M_2 for a given lamp spectrum, any unknown displacement can be inferred from the SSA values that are obtained. The proposed methods are compared in order to investigate the higher sensitivity of the methods for the measurement of the nano displacement. It is found that the method which deals with the spectrum with two spectral fringes occurring within the coherence length of the source has higher sensitivity than the other occurring far away from the coherence length.

The effect of the spectral characteristics such as spectral bandwidth, peak wavelength and symmetry of the input source spectrum on the spectral switch characteristics are investigated in detail. The spectral switch characteristics include spectral switch position, spectral switch amplitude and symmetry of the spectral switch with respect to the zero normalized spectral shifts. It is found that the switch amplitude and symmetry of the spectral switch increases with spectral bandwidth where as the switch position for a particular switch remains same for all the spectral bandwidths for a fixed peak wavelength. The spectral switch position is different for different peak wavelengths for a particular spectral switch. Though the variation of the spectral switch amplitude is small, the switch symmetry varies considerably for different peak wavelengths. The symmetry of the input spectrum with respect to the peak wavelength of the source shifts the spectral switches towards negative values (red side) of the normalized spectral shift due to high power spectral density in the red of the spectrum. It is also found that the spectral switch amplitude and switch positions are unaffected by the symmetry of the spectrum.

The generation of refocused filaments due to nonlinear propagation of the femtosecond laser pulses in a BK7 glass is studied as a function of input laser power. For each input power, the plasma luminescence of the filaments is imaged through a CCD, the output transmission spectrum is recorded using a spectrometer and the far-field spatial emission pattern is captured using a digital camera. The spatial anomalies (forklets) are observed in the far-field emission pattern due to three collinear filaments when the sample is rotated through an angle with respect to the input laser. These spatial anomalies are due to shear in one of the wavefronts of the three filaments. When the output power is adjusted to get the two filaments, we observe the spectral modulations in the output transmission spectrum. These spectral modulations are due to spectral interference of the white-light generated by the refocusing filaments. These spectral modulations are used to study the temporal separation of the collinear filaments by calculating the fringe period of the spectral modulations both in the lower wavelength and higher wavelength regions.

6.2 Future perspectives

There is a tremendous scope for the present work, both in theoretical and experimental aspects. It is interesting to see the effect of the material dispersion on the spectral shifts and spectral switches proposed in the current thesis. Though the procedure elaborated in this thesis to measure nano-scale displacements is to show that the method is new in comparison to the conventional methods, in practice the method can be implemented much more easily. The procedure could be made simple by using a fiber optic MI setup to probe the surfaces with a built in mini spectrometer, a program for peak location and arriving at the spectral switch position with two maxima using computer controlled nano-positioner. Once a calibrated reference data is acquired, the sample displacements can be easily measured by comparing with the reference. Software can be developed for easier and quicker measurements. As the spectral shifts around the spectral switches are highly sensitive to the optical path difference, they can be used to measure the thickness of the thin films accurately. These spectral shifts and

spectral switches can be extended to supercontinuum source to characterize the supercontinuum as the power spectral density of the supercontinuum depends on the material.

In the present thesis though we have discussed the experimental observation of the spatial anomalies present in the far-field spatial emission pattern due to collinear filaments and a simple model to explain them using computer calculations, theoretical work needs to be done on these spatial anomalies considering the dispersion effects. The spectral modulations observed in the output transmission spectrum can be used to estimate the nonlinear refractive index of the material. The effect of the polarization on the spectral modulations and spatial anomalies can be studied in detail which has not been discussed in the present thesis. One can also study the effect of birefringence of the material on the formation of the filaments and the spectral modulations in the output spectrum.

A

Five-frame phase calculation algorithm

Five-frame phase calculation algorithm has been suggested by Schwider *et al* [1].This phase calculation algorithm uses five intensity measurements, I_1, I_2, I_3, I_4 and I_5 corresponding to the additional phase steps of -2α, $-\alpha$, 0, $+\alpha$ and $+2\alpha$ respectively. Therefore

$$
\begin{aligned}
I_1 &= A+B+2(AB)^{1/2}\cos(\phi-2\alpha) \\
I_2 &= A+B+2(AB)^{1/2}\cos(\phi-\alpha) \\
I_3 &= A+B+2(AB)^{1/2}\cos(\phi) \\
I_4 &= A+B+2(AB)^{1/2}\cos(\phi+\alpha) \\
I_5 &= A+B+2(AB)^{1/2}\cos(\phi+2\alpha)
\end{aligned}
\tag{1}
$$

Here A and B are the intensities of two interfering beams and ϕ is the original phase difference between the two beams. Using the above equations we can write

$$
\frac{\sin\alpha\sin\phi}{(1-\cos 2\alpha)\cos\phi} = \frac{I_2 - I_4}{2I_3 - I_5 - I_1} \tag{2}
$$

When $\alpha = 90^0$, Eq. (2) reduces to

$$
\tan\phi = \frac{2(I_2 - I_4)}{2I_3 - I_5 - I_1} \tag{3}
$$

The phase step of the PZT can be ensured using four intensity values and can be calculated using [1]

$$
\cos\alpha = \frac{I_5 - I_1}{2(I_4 - I_2)} \tag{4}
$$

1. J. Schwider, R. Burow, K-E. Elssner, J. Grzanna, R. Spolaczyk and K. Merkel, Appl. Opt. **22**, 3421 (1983)

B

List of Publications

Refereed journals:

1. Maruthi M. Brundavanam, Nirmal K. Viswanathan and Narayana Rao Desai, *"Spectral anomalies due to temporal correlations in a White-light interferometer"*, Opt. Lett. **32**, 2279 (2007)
2. Maruthi M. Brundavanam, Nirmal K. Viswanathan and D. Narayana Rao, *"Nano displacement measurement using spectral shifts in a white light interferometer"*, Appl. Opt. **47**, 6334 (2008)
3. Maruthi M. Brundavanam, Nirmal K. Viswanatha and D. Narayana Rao, *"Effect of input spectrum on the spectral switch characteristics in a white-light Michelson interferometer"*, J. Opt. Soc. Am. A, **26**, 2592 (2009)
4. Maruthi M. Brundavanam, Nirmal K. Viswanatha and D. Narayana Rao, *"Measurement of the temporal correlation of the white light filaments in BK-7 glass using a femtosecond laser"*, (Manuscript in preparation)

Conference papers (national and international):

1. Maruthi M. Brundavanam, Nirmal K. Viswanathan, *"Wave front dislocations due to multiple filaments in a transparent medium using a femtosecond laser"*, National Laser Symposium-08, held at LASTEC, Delhi, January 7-10 (2009)
2. K.S. Alee, Maruthi M. Brundavanam, S.N.B. Bhaktha, A. Chiappini, M. Ferrari and D. Narayana Rao, "Effect of dye on the band gap of 3D polystyrene photonic crystals", Proc. Of SPIE, 7212, 72120R-1 (2009)
3. Maruthi M. Brundavanam, Nirmal K. Viswanathan and D. Narayana Rao, *" Effect of lamp spectrum on spectral shifts and switches in a white light interferometer"*, International conference on Fiber optics and Photonics-Photonics2008, IIT Delhi, Delhi, December 13-17 (2008)
4. Maruthi M. Brundavanam, Gopal K. Inavalli and Nirmal K. Viswanathan,*"Optical line singularity due to modal interference in tip modified optical fiber"*, International conference on Fiber optics and Photonics-Photonics2008, IIT Delhi, Delhi, December 13-17 (2008)
5. K.S.Alee, Maruthi M. Brundavanam, S.N.B. Bhaktha,A.Chiappini,M. Ferrari and D. Narayana Rao,*"Rhodamine B doped 3D polystyrene photonic crystals"*, International conference on Fiber optics and Photonics- Photonics 2008, held at IIT Delhi, Delhi, December 13-17 (2008)
6. B. Maruthi Manoj, Kalyan C. Rao, K. C. Vishnubhatla, Nirmal K. Viswanathan and D. Narayana Rao, *"Effect of dispersion on spectral changes in white-light interferometry"*, Eighth International Conference on Optoelectronics, Fiber optics and Photonics - Photonics2006, held at University of Hyderabad, Hyderabad, December 13-16 (2006)

resistant plants, 73 of 105 moderately resistant plants, 109 of 132 moderately susceptible plants, 85 of 110 susceptible plants and 20 out of 28 highly susceptible plants (Table 23) The marker was at a genetic distance of 13.6 cM away from the gene. The amplification pattern of RM23489 in a set of 32 F_2 plants was given in Figure 34.

Figure 34 : Segregation pattern of RM23489 in the F_2 population of the cross TN1 x Ajaya

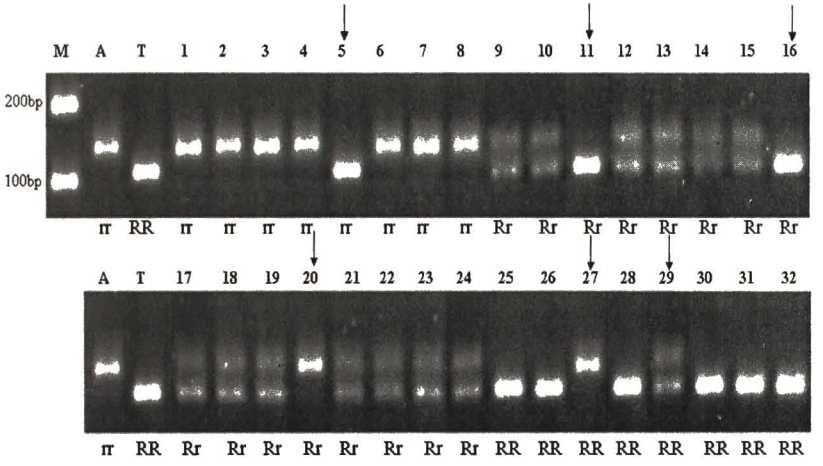

A-Ajaya, T-TN1, M-Molecular weight marker (100bp ladder). Number on top of the gel represents the F_2 plant number while the genotype of the plant (as deduced from progeny testing at $F_3$and marker genotype of RG556) is represented at the bottom of the gel. rr and RR indicate homozygous resistant and homozygous susceptible F_2 plants respectively, while Rr represents heterozygous susceptible plants. Arrows on top of the gel indicate recombinants

RM23496:

The marker displayed amplification of Ajaya specific fragment in homozygous fashion in 100 of 104 homozygous resistant F_2 plants, heterozygous amplification pattern in 192 of 188 heterozygous susceptible F_2 plants and TN1 specific fragment in homozygous condition in 108 of 108 homozygous susceptible F_2 plants in a typical Mendelian ratio of 1:2:1 (χ^2 = 0.96, P = 0.61). Based on the amplification pattern of the marker in combination with RG556 it was possible to predict the trait phenotype in 22 of 25 resistant plants, 82 of 105 moderately resistant plants, 96 of 132 moderately susceptible plants, 84 of 110 susceptible plants and 26 out of 28 highly susceptible plants (Table 23).The marker was at genetic distance of 12.2 cM away from the gene. The amplification pattern of RM23496 in a set of 32 F_2 plants was given in Figure 35.

Figure 35 : Segregation pattern of RM23496 in the F_2 population of the cross TN1 x Ajaya

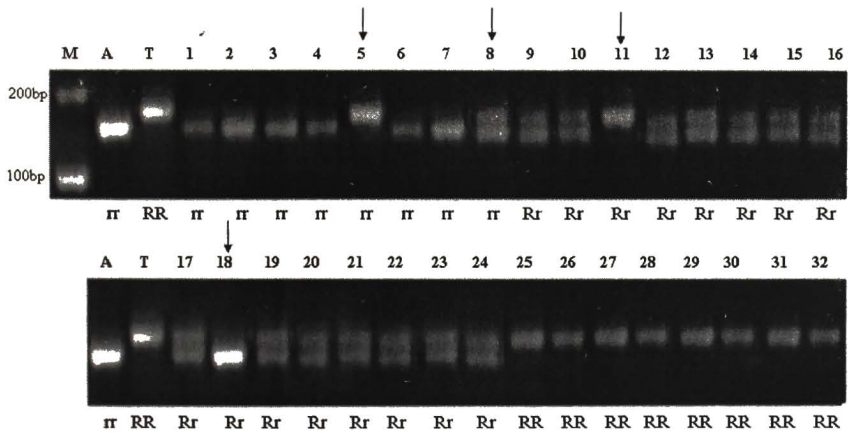

A-Ajaya, T-TN1, M-Molecular weight marker (100bp ladder). Number on top of the gel represents the F_2 plant number while the genotype of the plant (as deduced from progeny testing at $F_3$and marker genotype of RG556) is represented at the bottom of the gel. rr and RR indicate homozygous resistant and homozygous susceptible F_2 plants respectively, while Rr represents heterozygous susceptible plants. Arrows on top of the gel indicate recombinants

RMAFM2:

The marker displayed amplification of Ajaya specific fragment in homozygous fashion in 99 of 104 homozygous resistant F_2 plants, heterozygous amplification pattern in 192 of 188 heterozygous susceptible plants and TN1 specific fragment in homozygous condition in 109 of 108 homozygous susceptible plants in a typical Mendelian ratio of 1:2:1 (χ^2 = 1.14, P = 0.56). Based on the amplification pattern of the marker in combination with RG556 it was possible to predict the trait phenotype in 24 of 25 resistant plants, 97 of 105 moderately resistant plants, 102 of 132 moderately susceptible plants, 104 of 110 susceptible plants and 26 out of 28 highly susceptible plants (Table 23). The marker was at a genetic distance of 4.3 cM away from the gene. The amplification pattern of RMAFM2 in a set of 32 F_2 plants was given in Figure 36.

Figure 36 : Segregation pattern of RMAFM2 in the F_2 population of the cross TN1 x Ajaya

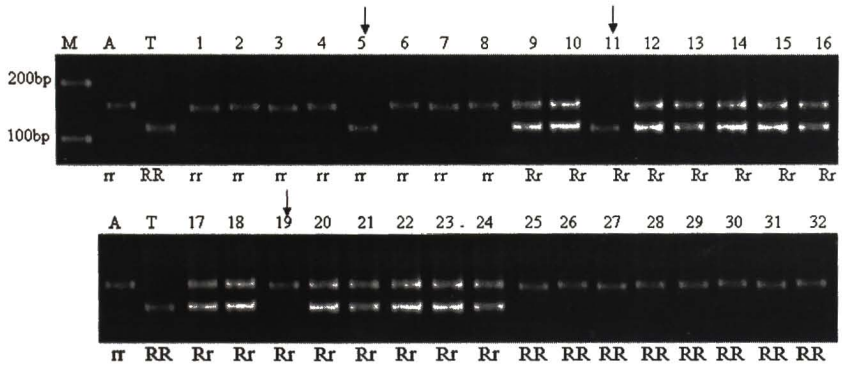

A-Ajaya, T-TN1, M-Molecular weight marker (100bp ladder). Numbers on top of the gel represent the F_2 plant while the genotype of the plant (as deduced from progeny testing at F_3 and marker genotype of RG556) is represented at the bottom of the gel. rr and RR indicate homozygous resistant and homozygous susceptible F_2 respectively, while Rr represents heterozygous susceptible plants. Arrows on top of the gel indicate recombinants

RMAFM1:

The marker displayed amplification of Ajaya specific fragment in homozygous fashion in 105 of 104 homozygous resistant F_2 plants, heterozygous amplification pattern in 184 of 188 heterozygous susceptible plants and TN1 specific fragment in homozygous condition in 111 of 108 homozygous susceptible F_2 plants in a typical Mendelian ratio of 1:2:1 (χ^2 = 2.74, P = 0.25). Based on the amplification pattern of the marker in combination with RG556 it was possible to predict the trait phenotype in 24 of 25 resistant plants, 102 of 105 moderately resistant plants, 127 of 132 moderately susceptible plants, 106 of 110 susceptible plants and 28 out of 28 highly susceptible plants (Table 23). The marker was at a genetic distance of 1.9 cM away from the gene. The amplification pattern of RMAFM1 in a set of 32 F_2 plants was given in Figure 37.

Figure 37 : Segregation pattern of RMAFM1 in the F_2 population of the cross TN1 x Ajaya

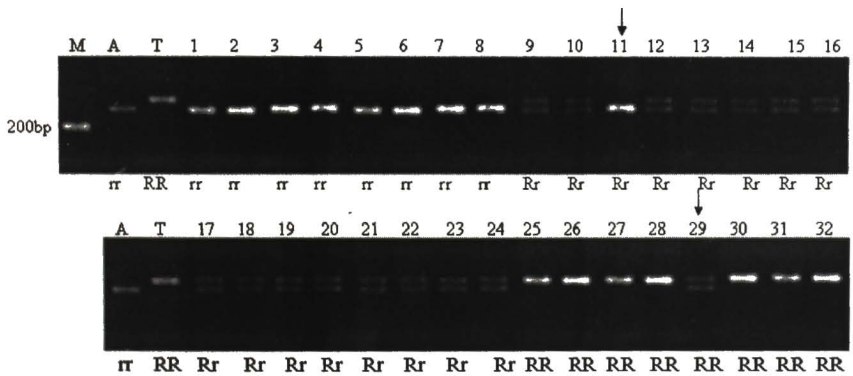

A-Ajaya, T-TN1, M-Molecular weight marker (100bp ladder). Numbers on top of the gel represent the F_2 plant while the genotype of the plant (as deduced from progeny testing at $F_3$and marker genotype of RG556) is represented at the bottom of the gel. rr and RR indicate homozygous resistant and homozygous susceptible F_2 respectively, while Rr represents heterozygous susceptible plants. Arrows on top of the gel indicate recombinants

RM447:

The marker displayed amplification of Ajaya specific fragment in homozygous fashion in 105 of 104 homozygous resistant F_2 plants, heterozygous amplification pattern in 187 of 188 heterozygous susceptible plants and TN1 specific fragment in homozygous condition in 108 of 108 homozygous susceptible plants in a typical Mendelian ratio of 1:2:1 (χ^2 = 1.73, P = 0.42). Based on the amplification pattern of the marker in combination with RG556 it was possible to predict the trait phenotype in 25 of 25 resistant plants, 103 of 105 moderately resistant plants, 131 of 132 moderately susceptible plants, 108 of 110 susceptible plants and 26 out of 28 highly susceptible plants (Table 23). The marker was at a genetic distance of 0.87 cM away from the gene. The amplification pattern of RM447 in a set of 32 F_2 plants was given in Figure 38.

Figure 38 : Segregation pattern of RM447 in the F_2 population of the cross TN1 x Ajaya

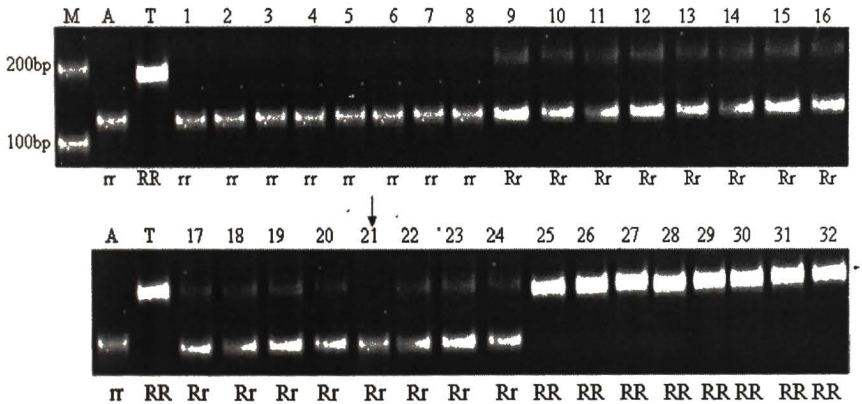

A-Ajaya, T-TN1, M-Molecular weight marker (100bp ladder). Numbers on top of the gel represent the F_2 plant while the genotype of the plant (as deduced from progeny testing at F_3 and marker genotype of RG556) is represented at the bottom of the gel. rr and RR indicate homozygous resistant and homozygous susceptible F_2 respectively, while Rr represents heterozygous susceptible plants. Arrows on top of the gel indicate recombinants

RMAFM4:

The marker displayed amplification of Ajaya specific fragment in homozygous fashion in 101 of 104 homozygous resistant F_2 plants, heterozygous amplification pattern in 191 of 188 heterozygous susceptible plants and TN1 specific fragment in homozygous condition in 108 of 108 homozygous susceptible plants in a typical Mendelian ratio of 1:2:1 (χ^2 = 1.05, P = 0.59). Based on the amplification pattern of the marker in combination with RG556 it was possible to predict the trait phenotype in 24 of 25 resistant plants, 97 of 105 moderately resistant plants, 123 of 132 moderately susceptible plants, 106 of 110 susceptible plants and 27 out of 28 highly susceptible plants (Table 23). The marker was at genetic distance of 3.1 cM away from the gene. The amplification pattern of RMAFM4 in a set of 32 F_2 plants was given in Figure 39.

Figure 39 : Segregation pattern of RMAFM4 in the F_2 population of the cross TN1 x Ajaya

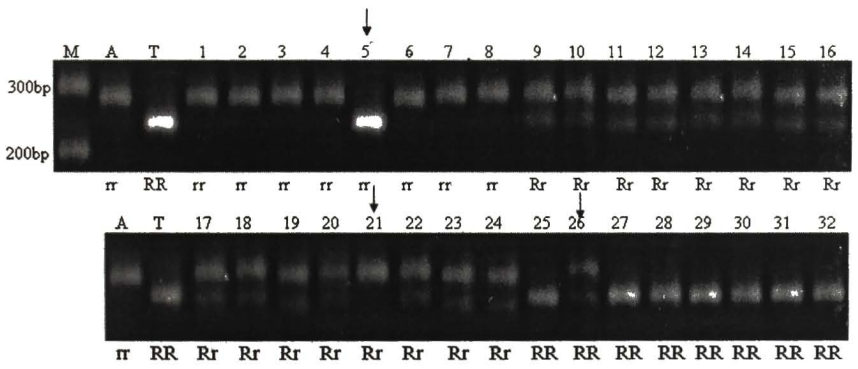

A-Ajaya, T-TN1, M-Molecular weight marker (100bp ladder). Numbers on top of the gel represent the F_2 plant while the genotype of the plant (as deduced from progeny testing at F_3 and marker genotype of RG556) is represented at the bottom of the gel. rr and RR indicate homozygous resistant and homozygous susceptible F_2 respectively, while Rr represents heterozygous susceptible plants. Arrows on top of the gel indicate recombinants

RMAFM5:

The marker displayed amplification of Ajaya specific fragment in homozygous fashion in 101 of 104 homozygous resistant F_2 plants, heterozygous amplification pattern in 184 of 188 heterozygous susceptible F_2 plants and TN1 specific fragment in homozygous condition in 115 of 108 homozygous susceptible plants in a typical Mendelian ratio of 1:2:1 (χ^2 = 3.54, P = 0.17). Based on the amplification pattern of the marker in combination with RG556 it was possible to predict the trait phenotype in 22 of 25 resistant plants, 93 of 105 moderately resistant plants, 118 of 132 moderately susceptible plants, 99 of 110 susceptible plants and 25 out of 28 highly susceptible plants (Table 23).The marker was at genetic distance of 6.2 cM away from the gene. The amplification pattern of RMAFM5 in a set of 32 F_2 plants was given in Figure 40.

Figure 40 : Segregation pattern of RMAFM5 in the F_2 population of the cross TN1 x Ajaya

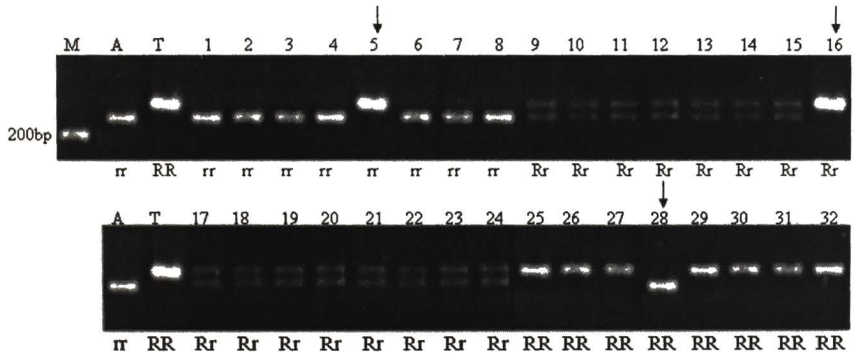

A-Ajaya, T-TN1, M-Molecular weight marker (100bp ladder). Numbers on top of the gel represent the F_2 plant while the genotype of the plant (as deduced from progeny testing at $F_3$and marker genotype of RG556) is represented at the bottom of the gel. rr and RR indicate homozygous resistant and homozygous susceptible F_2 respectively, while Rr represents heterozygous susceptible plants. Arrows on top of the gel indicate recombinants

RMAFM6:

The marker displayed amplification of Ajaya specific fragment in homozygous fashion in 88 of 104 homozygous resistant F_2 plants, heterozygous amplification pattern in 198 of 188 heterozygous susceptible plants and TN1 specific fragment in homozygous condition in 96 of 108 homozygous susceptible plants in a typical Mendelian ratio of 1:2:1 (χ^2 = 0.22, P = 0.89). Based on the amplification pattern of the marker in combination with RG556 it was possible to predict the trait phenotype in 21 of 25 resistant plants, 92 of 105 moderately resistant plants, 110 of 132 moderately susceptible plants, 97 of 110 susceptible plants and 20 out of 28 highly susceptible plants (Table 23). The marker was at genetic distance of 10.1 cM from the gene. The amplification pattern of RMAFM6 in a set of 32 F_2 plants was given in Figure 41.

Figure 41 : Segregation pattern of RMAFM6 in the F_2 population of the cross TN1 x Ajaya

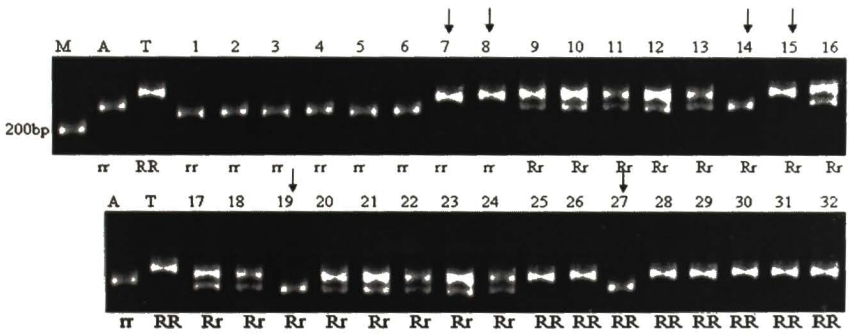

A-Ajaya, T-TN1, M-Molecular weight marker (100bp ladder). Numbers on top of the gel represent the F_2 plant while the genotype of the plant (as deduced from progeny testing at $F_3$and marker genotype of RG556) is represented at the bottom of the gel. rr and RR indicate homozygous resistant and homozygous susceptible F_2 respectively, while Rr represents heterozygous susceptible plants. Arrows on top of the gel indicate recombinants

RMAFM6:

The marker displayed amplification of Ajaya specific fragment in homozygous fashion in 88 of 104 homozygous resistant F_2 plants, heterozygous amplification pattern in 198 of 188 heterozygous susceptible plants and TN1 specific fragment in homozygous condition in 96 of 108 homozygous susceptible plants in a typical Mendelian ratio of 1:2:1 (χ^2 = 0.22, P = 0.89). Based on the amplification pattern of the marker in combination with RG556 it was possible to predict the trait phenotype in 21 of 25 resistant plants, 92 of 105 moderately resistant plants, 110 of 132 moderately susceptible plants, 97 of 110 susceptible plants and 20 out of 28 highly susceptible plants (Table 23). The marker was at genetic distance of 10.1 cM from the gene. The amplification pattern of RMAFM6 in a set of 32 F_2 plants was given in Figure 41.

Figure 41 : Segregation pattern of RMAFM6 in the F_2 population of the cross TN1 x Ajaya

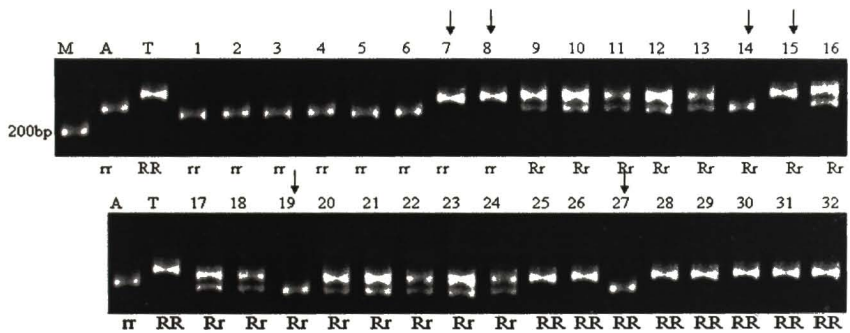

A-Ajaya, T-TN1, M-Molecular weight marker (100bp ladder). Numbers on top of the gel represent the F_2 plant while the genotype of the plant (as deduced from progeny testing at $F_3$and marker genotype of RG556) is represented at the bottom of the gel. rr and RR indicate homozygous resistant and homozygous susceptible F_2 respectively, while Rr represents heterozygous susceptible plants. Arrows on top of the gel indicate recombinants

Table 23: Segregation pattern of polymorphic markers in the F_2 population derived from TN1/Ajaya

S. No.	SSR marker	Physical position (Mb)	No. of plants showing amplification of Ajaya allele in homozygous condition i.e., r2r2	No. of plants showing heterozygous amplification i.e., R2r2	No. of plants showing amplification of TN1 allele in homozygous condition i.e, R2R2	Segregation ratio	Genetic distance (cM)
1	RM23489	26 401	82	213	105	1 2 1(λ=4 33, P=0 11)	13 6
2	RM23496	26 500	100	192	108	1 2 1(λ=0 96, P-0 61)	12 2
3	RMAFM2	26 607	99	192	109	1 2 1(λ=1 14, P=0 56)	4 3
4	RMAFM1	26 624	105	184	111	1 2 1(λ=2 74, P=0 25)	1 9
5	RM447	26 637	105	187	108	1 2 1(λ=1 73, P=0 42)	0 87
6	RMAFM4	26 643	101	191	108	1 2 1(λ=1 05, P=0 59)	3 1
7	RMAFM5	26 825	101	184	115	1 2 1(λ=3 54, P=0 17)	6 2
8	RMAFM6	26 914	88	198	96	1 2 1(λ=0 22, P=0 89)	10 1

The markers RM23489, RM23496, RMAFM2 and RMAFM1 were observed to be located on one side of the gene, while RM447, RMAFM4, RMAFM5 and RMAFM6 were located on the other side. The closest flanking SSR markers RM447 and RMAFM1 were observed to be located at a genetic distance of 0.87 and 1.9 cM respectively from the gene.

When the data obtained from the SSR markers used for fine mapping of the novel gene was analyzed using Mapmaker software, the markers RM23489, RM23496, RMAFM2 and RMAFM1 were observed to be located on one side of the gene at a genetic distance of 13.6 cM, 12.2 cM, 4.3 cM and 1.9 cM respectively , while RM447, RMAFM4, RMAFM5 and RMAFM6 were located on the other side of the gene at a genetic distance of 0.87 cM, 3.1 cM, 6.2 cM and 10.1cM respectively (Figure 42). RM447 and RMAFM1 were very close to the gene and flanking it.

Figure 42 :Genetic linkage map of the genomic region in the vicinity of *xa36t* on Chr.8

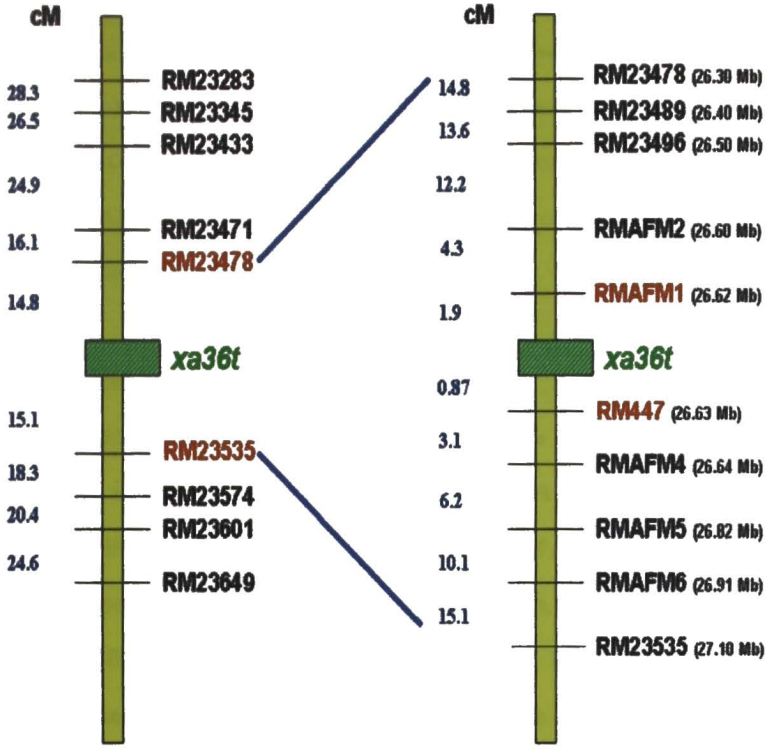

The SSR markers RM447 and RMAFM1 were found to be close to the gene and flanking the novel resistance gene *xa36t* at a genetic distance of 0.87 and 1.9cM respectively

4.3.9 Validation of the linked SSR markers in alternate mapping population

The *xa5* linked CAPS marker RG556 and the SSR markers identified to be closely linked to the resistance gene *xa36t* as observed in the F_2 population of the cross TN1/Ajaya were validated in a progeny-tested F_2 population consisting of 196 plants derived from the cross BPT5204/Ajaya. The closest marker RM447 was monomorphic between Ajaya and BPT5204. RG556 and the other closer and flanking polymorphic markers RMAFM1, RMAFM2, RMAFM4, and RMAFM5 were studied for their co segregation with respect to resistance/ susceptibility in the alternate population.

4.3.9.1 Genotyping at *xa5* locus with RG556:

The marker RG556 linked to *xa5* was amplified in the whole F_2 population of the cross BPT5204/Ajaya to study the segregation pattern. This marker amplified the resistant parent specific allele in homozygous condition (i.e. rr) in 42 F_2 plants, and both resistant and susceptible parent specific fragments (Rr) in 106 F_2 plants, and the susceptible parent (i.e. TN1) specific fragment in homozygous condition (i.e. RR) in 48 F_2 plants in a typical Mendelian ratio of 1:2:1 with respect to rr:Rr:RR ($\chi^2 = 1.67$, P=0.43). The marker amplified the resistant parent specific allele in homozygous condition (i.e. rr) in all the 10 resistant plants and homozygous susceptible allele in all the 16 highly susceptible plants indicating that *xa5* conditions resistance in the alternate population derived from the cross BPT5204/Ajaya (Figure 43). The marker amplified the resistant parent specific allele in homozygous condition in 20 of 38 moderately resistant plants and 17 of 89 moderately susceptible plants. It showed heterozygous specific amplification in 18 of 38 moderately resistant plants, 51 of 89 moderately susceptible plants and 23 of 43 susceptible plants. It

showed homozygous susceptible specific amplification in 21 of 89 moderately susceptible plants and 20 of 43 susceptible plants. This data along with the F_3 phenotypic data was used to predict the corresponding genotype at the second resistance gene locus of each of the individual plants constituting the alternate population.

Figure 43 :Analysis of the CAPS marker RG556 in the F_2 population of the cross BPT5204 x Ajaya

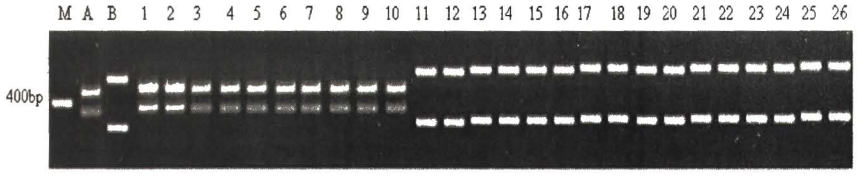

A-Ajaya, B-BPT5204, M-Molecular weight marker (100bp ladder). 1-10 are resistant F_2 plants, 11-26 are highly susceptible F_2 plants

4.3.9.2 Segregation of markers linked to *xa36t* on Chr8

RMAFM2:

The marker in combination with RG556 could predict the trait phenotype in eight of the ten resistant plants, 35 of 38 moderately resistant plants, 81 of 89 moderately susceptible plants, 42 of 43 susceptible plants and 14 out of 16 highly susceptible plants. The marker was observed to be at a genetic distance of 5.4 cM away from the gene.

RMAFM1:

The marker in combination with RG556 could predict the trait phenotype in nine of the ten resistant plants, 36 of 38 moderately resistant plants, 86 of 89 moderately susceptible plants, 42 of 43 susceptible plants and 15 out of 16 highly susceptible plants. The marker showed a linkage distance of 2.1 cM from the gene. The amplification pattern of RMAFM1 in a set of 32 F2 plants was given in Figure 44.

Figure 44 : Segregation pattern of RMAFM1 in the F_2 population of the cross BPT5204 x Ajaya

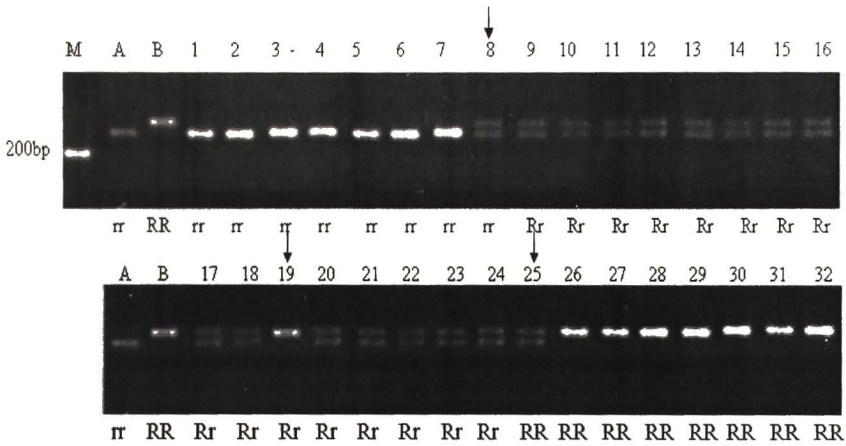

A-Ajaya, B-BPT5204, M-Molecular weight marker (100bp ladder). Numbers on top of the gel represent the F_2 plant while the genotype of the plant (as deduced from progeny testing at $F_3$and marker genotype of RG556) is represented at the bottom of the gel. rr and RR indicate homozygous resistant and homozygous susceptible F_2 respectively, while Rr represents heterozygous susceptible plants. Arrows on top of the gel indicate recombinants

RMAFM5:

The marker in combination with RG556 could predict the trait phenotype in seven of the ten resistant plants, 34 of 38 moderately resistant plants, 81 of 89 moderately susceptible plants, 39 of 43 susceptible plants and 13 out of 16 highly susceptible plants. The marker was at genetic distance of 7.5 cM away from the gene.

RMAFM4:

The marker in combination with RG556 could predict the trait phenotype in eight of the ten resistant plants, 34 of 38 moderately resistant plants, 87 of 89 moderately susceptible plants, 40 of 43 susceptible plants and 15 out of 16 highly susceptible plants. The marker was at genetic distance of 4.2 cM from the gene. The amplification pattern of RMAFM4 in a set of 32 F_2 plants was given in Figure 45.

Figure 45 : Segregation pattern of RMAFM4 in the F_2 population of the cross BPT5204 x Ajaya

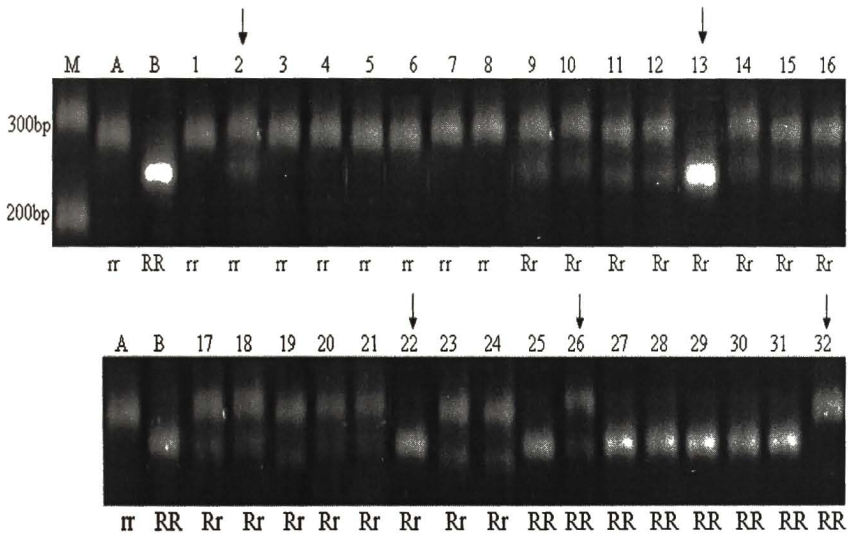

A-Ajaya, B-BPT5204, M-Molecular weight marker (100bp ladder). Numbers on top of the gel represent the F_2 plant while the genotype of the plant (as deduced from progeny testing at F_3 and marker genotype of RG556) is represented at the bottom of the gel. rr and RR indicate homozygous resistant and homozygous susceptible F_2 respectively, while Rr represents heterozygous susceptible plants. Arrows on top of the gel indicate recombinants

Table 24: Comparison of the recombination distances in the two populations

Marker	Recombination distance in TN1/Ajaya (cM)	Recombination distance in BPT5204/Ajaya (cM)
RMAFM2	4.3	5.4
RMAFM1	1.9	2.1
RMAFM4	3.1	4.2
RMAFM5	6.2	7.5

Linkage analysis of the marker segregation data in both the populations using Mapmaker software revealed similar marker order as well as recombination distances with the resistance gene (Table 24). Thus the above markers could effectively validate the gene in the alternate population and the gene could be precisely mapped in between the markers RMAFM1 and RMAFM4.

4.3.10 Analysis of amplification pattern of the novel gene linked SSR markers in a set of rice varieties

To examine whether the linked markers would be of use in introgression of the novel gene into other BLB susceptible cultivars, DNA samples from a set of nine high priority bacterial leaf blight susceptible cultivars (TN1, Samba Mahsuri (BPT5204), Swarna, MTU1001, MTU1010, Tellahamsa, Krishnahamsa, IR64 and Basmati370) along with the Ajaya, were amplified by PCR using the closest flanking markers RM447 and RMAFM1 and RMAFM4 (Table 25).

Table 25: Amplification pattern of the novel gene linked SSR markers in a set of parental lines

S. No.	Name of the Genotype	Fragment Size (bp)		
		RM447	RMAFM1	RMAFM4
1	Ajaya	110	160	290
2	TN1	130	170	270
3	Samba Mahsuri (BPT5204)	110	170	270
4	Swarna	110	180	270
5	MTU1001	130	180	270
6	MTU1010	110	160	270
7	Tellahamsa	110	180	270
8	Krishnahamsa	130	180	270
9	IR64	110	150	270
10	Basmati370	120	180	270

The marker RM447 amplified a fragment of size 110 bp in Ajaya while the nine susceptible genotypes yielded fragments (i.e. alleles) of size 110-130 bp. With respect to the marker RMAFM1, the susceptible cultivars amplified alleles in the size range 150-180 bp, while in case of Ajaya, a fragment of size 160 bp was observed to be amplified (Figure 46). The marker RMAFM4 amplified a fragment of size 300 bp in Ajaya and 290bp in all the nine susceptible genotypes. The flanking marker combination of RM447-RMAFM1 can be used for introgression of the gene from Ajaya in to susceptible cultivars TN1, MTU1001, Krishnahamsa and Basmati370. For introgression in to other susceptible cultivars Samba Mahsuri, Swarna, Tellahamsa and IR64 the marker combination of RMAFM1-RMAFM4 can be used. Since both the markers RM447 and RMAFM1 are monomorphic between Ajaya and MTU1010, the marker RMAFM4 can be used singly or in combination with the other relatively closer polymorphic markers for introgression of the gene from Ajaya.

Figure 46 :Analysis of flanking markers in a set of high priority BLB susceptible cultivars

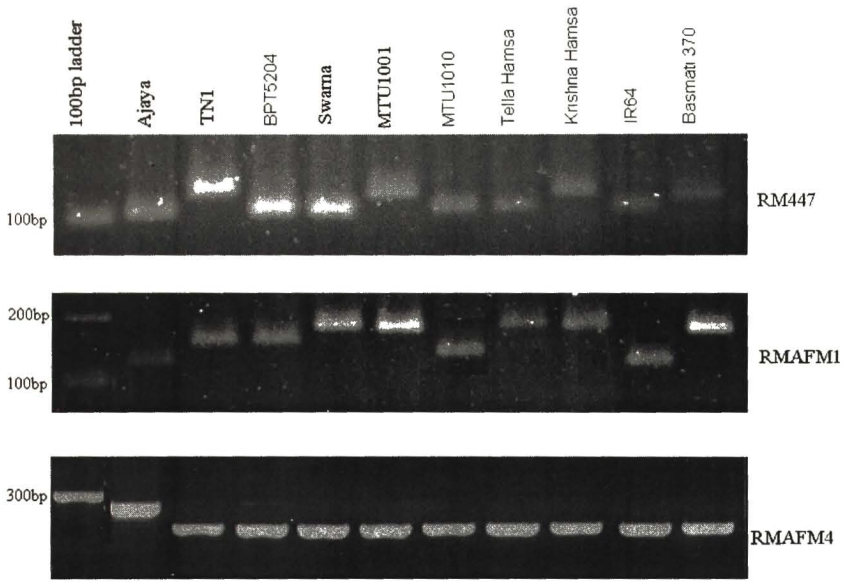

4.3.11 Analysis of genes present in the genomic region on Chromosome 1 flanked by SSR markers closely linked to the novel Bacterial leaf blight resistance gene

Based on fine structure linkage map, the SSR marker RM447 was located at a genetic distance of 0.87 cM on one side of the gene and RMAFM1 was located on the other side of the gene at a genetic distance of 1.9 cM (Figure 42). The forward primer of RMAFM1was observed to be physically located (start position) in the Japonica genome (http://rise.genomics.org.cn) at 26.624bp while the reverse primer of RM447 was physically located (end position) at 26.637 bp. The intervening genomic region consisting of 13 kb of sequence was downloaded from the Japonica genome sequence database (http://rise.genomics.org.cn) and analyzed for presence of putative genes using the

software Fgenes H (http://www.softberry.com). The functionality of the genes was analyzed using the BLAST tool (Altschul *et al* 1990) available online at http://www.ncbi.nlm.gov.in. A total of three genes were observed to be present in the genomic region flanked by RMAFM1 and RM447. The average gene density was one gene for every ~ 4.33 kb of sequence. Of the three genes identified in the region, one is Nodulin gene; one was SUA7 a yeast gene coding for the transcription factor TFIIB and the other was a gene belonging to plant peroxidase super family. The details of the list of the genes along with their size in base pairs, amino acids along with their putative function(s) were given in Table 26.

Table 26: List of genes present in the genomic region flanked by SSR markers RMAFM1 and RM447

Gene No.	Gene start (bp)	Gene end (bp)	Gene size (bp)	No. of amino acids	Putative function of protein encoded by the gene and proteins showing homology to the gene
1	26625582	26630530	1665	554	Nodulin gene
2	26630866	26633866	1722	573	SUA7,Transcription factor TFIIB
3	26635013	26637736	843	280	Plant peroxidase super family

Chapter 5

Discussion

Chapter V – Discussion

Bacterial leaf blight (BLB) of rice caused by *Xanthomonas oryzae* pv. *Oryzae* is one of the most destructive diseases of rice, particularly in the *kharif* season crop in India Since chemical control is ineffective, development and deployment of BLB resistant cultivars is the only practical strategy for managing the disease. However, large scale and long term cultivation of cultivars possessing single genes (*Xa3* in Japonica rice and *Xa4* in Indica rice) have resulted in the appearance of virulent strains which can overcome resistance. The breakdown of resistance to bacterial blight in the rice variety Asakaze in Japan is a famous example of the instability of major genes (Ezuka and Sakaguchi, 1978). In 1972, an isolate strain, designated "Isabela," from the northern part of the Philippines was found to cause breakdown of *Xa4* conferred resistance (IRRI, 1973) and in 1975, IRRI cultivars carrying the *Xa4* gene became susceptible to bacterial blight not only in the Philippines (Mew *et al.*, 1992) but also in many parts of India, Indonesia, and China (Huang *et al.*, 1997).

Resistance conferred by the major gene *Xa21* has also been reported to be overcome in some parts of India and Indonesia (Sirisha *et al.*, 2004; Goel *et al.*, 1998). One strategy to delay such breakdown of resistance is to provide a broad-spectrum of resistance by combining multiple genes having complementary resistance spectra, in a single plant genotype through the strategy of gene pyramiding (Babujee and Gnanamanickam, 2000). Gene pyramiding would thus result in development of genotypes with more durable resistance through individual gene action and quantitative complementation (Ogawa *et al.*, 1987; Yoshimura *et al.*, 1995b). The present study was therefore designed to identify, broad spectrum BLB resistance

genes from wild rice introgression lines of rice and durable BLB resistant cultivars, to tag and map them with tightly linked SSR markers

A total of 72 wild rice introgression lines carrying introgressions from the wild species *O. nivara* (8), *O rufipogon* (32),*O. longistaminata* (7), *O. glaberrima* (4), *O. officinalis* (9) and *O.brachyantha* (12), obtained from the International Rice Research Institute, Phillipines were screened for their resistance to BLB with seven hyper-virulent isolates of *Xanthomonas oryzae* pv. *oryzae*. One line carrying introgression from *Oryza brachyantha* (FF genome) i.e. IR-65483-141-2-4-4-2-5-B in the background of the *O. sativa* indica cultivar IR56 and the variety Ajaya (IET 8585) showed resistance reaction consistently with all the isolates tested under both the glasshouse and field conditions. Further IR-65483-141-2-4-4-2-5-B was observed to be superior in terms of BLB resistance when compared with NILs of IR24 carrying the single BLB resistance genes *xa5*, *xa13*, *Xa21* and was on par with respect to resistance reaction with the NILs of IR24 carrying four BLB resistance genes *Xa4*, *xa5*, *xa13* and *Xa21*. Ajaya showed higher average lesion length when compared to the NILs of IR24 possessing four BLB resistance genes *Xa4*, *xa5*, *xa13* and *Xa21* but was on par with NILs of IR24 possessing the individual genes *xa13* and *Xa21* and was significantly superior to the NIL of IR24 possessing *xa5* (Table 8). Based on these observations, it was hypothesized that these genotypes may possess one or more novel BLB resistance genes.

The introgression line IR-65483-141-2-4-4-2-5-B was developed from the cross of IR56 with101231 (an accession of *O. brachyantha*) by embryo rescue technique (Brar and Khush, 1997). Genetic analysis in the F_2 population derived from the cross IR-65483-141-2-4-4-2-5-B/TN1 revealed the action of a single dominant resistance gene

governing resistance. Out of the 296 F_2 plants screened for resistance, 225 plants were resistant, while 71were susceptible which fitted well in a segregation ratio of 3R:1S (χ^2= 0.16, P=0.68). Progeny testing of the 296 individuals revealed that the F_2 plants segregated in a classical Mendelian ratio of 1:2:1 (χ^2= 0.66, P=0.71) with respect to homozygous resistant, heterozygous resistant and homozygous susceptible individuals. The F_2 population consisting of 250 individuals of the cross IR-65483-141-2-4-4-2-5-B /BPT5204 also showed segregation in 3R:1S ratio (195 resistant and 55 susceptible) (χ^2= 1.2, P=0.27). Progeny testing of the F_2 lines, as observed earlier segregated in a ratio of 1:2:1, (χ^2= 2.37, P=0.30) with respect to homozygous resistant, heterozygous resistant and homozygous susceptible individuals. These results confirm the action of a single dominant gene in conferring resistance in IR-65483-141-2-4-4-2-5-B

In order to identify whether the dominant BLB resistance gene identified in IR-65483-141-2-4-4-2-5-B is allelic to any of the known, dominant BLB resistance genes, allelism tests were carried out with NILs of IR24 carrying known single dominant resistance genes, viz. *Xa1, Xa4, Xa7, Xa21* and *Xa26*. Similar allelism tests were conducted by Ogawa *et al.*, 1978, Ogawa and Yamamoto, (1986), Sidhu *et al.*, (1978; 1979), while studying inheritance and novelty of BLB resistance genes. The F_2 plants derived from the crosses of IR-65483-141-2-4-4-2-5-B with IRBB1, IRBB4, IRBB7, IRBB21 and IRBB26 segregated in a phenotypic ratio of 15R:1S indicating that the resistant gene is non-allelic to any of the above said dominant BLB resistance genes. However, since DRR, Hyderabad did not possess IR24 NILs carrying other known dominant resistance genes, the novelty of the gene in IR-65483-141-2-4-4-2-5-B, could not be confirmed with certainty. It was hypothesized that if the gene is novel, it

should be mapped to a genomic location, which is hitherto unreported for any known dominant BLB resistance genes. Hence, a molecular mapping analysis was carried out using SSR markers in order to identify the chromosomal location of the putatively novel BLB resistance gene in IR-65483-141-2-4-4-2-5-B and to identify markers closely linked to the gene for possible use in marker-assisted selection.

A total of 282 SSR markers were used for the survey of parental polymorphism in the preliminary coarse mapping analysis with coverage of ~ 23 markers per chromosome. Out of the 282 SSR markers analyzed, 106 displayed polymorphism between the resistant and susceptible parents (i.e. IR-65483-141-2-4-4-2-5-B and TN1) covering all the 12 chromosomes of rice, (8.8 markers per chromosome), giving an approximate coverage of one marker every 4 cM. The parental polymorphic SSR markers were then analyzed through the strategy of bulked-segregant analysis (BSA) for identification of markers displaying co-segregation with trait phenotype. The strategy of BSA has been used earlier for tagging and mapping of many agronomically important genes in rice like white back plant hopper resistance genes (Tan *et al.*, 2004), *Xa30t* (Cheema *et al.*, 2008) and QTLs associated with heat tolerance (Zhang *et al.*, 2009). In the present study also, the strategy of BSA was successful in identifying the tentative localization of the new BLB resistance on Chr. 1 using the SSR marker RM595.

While tagging and mapping the putatively novel BLB resistance gene present in, IR-65483-141-2-4-4-2-5-B progeny testing at F_3 generation under a stringent phenotyping procedure as described in materials and methods ensured correct identification of homozygotes and heterozygotes in F_2 with no escapes. The choice of a early segregating population like F_2, which was used in the present study for tagging

and mapping BLB resistance gene(s) is considered to be useful, as it saves time and resources in tagging and mapping compared to development and utilization of advanced generation populations like recombinant inbred lines and near isogenic lines, which take a lot of time for development (Michelmore *et al.*, 1991; Haley *et al.*, 1994; Biradar *et al.*, 2004).

In bulked-segregant analysis, RM595 showed association with trait phenotype. Any marker that assorts independently of resistance gene will display amplification of fragments specific for both resistant and susceptible parents in both resistant bulk (RB) as well as susceptible bulk (SB), whereas a co-dominant marker closely linked to the target gene will show only susceptible parent specific fragment in the SB, and only the resistant parent specific fragment in the RB. In the present study, based on the bulked-segregant analysis, it was hypothesized that the BLB resistance gene may be close to the marker RM595, since the marker showed clear bulk specific amplification pattern. This marker when analyzed in the entire mapping population, showed a linkage distance of 10.2 cM with the gene.

In order to identify the tentative map location of the putatively novel BLB resistance gene on Chr. 1, 20 SSR markers selected from the vicinity of the genomic region where RM595 is located were tested for parental polymorphism. Of these, seven were polymorphic. When these polymorphic SSRs were tested for their marker-trait segregation pattern in the F_2 mapping population, two markers *viz.,* RM10916 (15.052Mb) and RM11002 (17.805Mb) were observed to be the closest and flanking the BLB resistance gene at a genetic distance of 14cM and 15.2cM respectively. Even though these markers were not close enough to be used for marker-assisted selection

of the gene, the fact that these two markers flank the resistance gene helped to narrow down the gene to a physical region of 2.75Mb on Chr. 1 which served as a starting point for fine-mapping analysis.

For carrying out fine-mapping analysis, a set of nine hyper-variable RM series SSR markers (http://www.gramene.org) and eight newly designed SSR markers (RMCG1 to RMCG8) located in the genomic region spanned by RM10916 and RM11002 were used. The gene was mapped at a distance of 0.82 cM from the marker RM10975 and 1.8 cM away from RMCG6 with both these markers flanking the gene. The markers RM10920, RM10963, RMCG5, RM10974 and RM10975 were observed to be located on one side of the gene at a genetic distance of 9.4 cM, 7.5 cM, 6 cM 1.85 cM and 0.82cM respectively while RMCG6, RMCG7 and RMCG8 were located on the other side of the gene at a genetic distance of 1.8 cM, 5.6 cM, and 8.4 cM respectively.. Tan et al., (2004) reported a dominant BLB resistance gene *Xa29t* from the wild species *O. officinalis* and mapped it on Chr. 1 in the marker interval of two RFLP markers C904 (13.6MB) and R596 (15.4MB). Hence the gene identified in the present study spanned by the flanking markers RM10975 (16.952MB) and RMCG6 (16.968) was considered as novel and has been designated as *Xa35t.*

Even though the two closest flanking markers RM10975 (0.82cM) and RMCG6 (1.8cM) showed a few recombinants, they both are as such individually close enough for effective use in marker-assisted selection. Further, the fact that the two SSR markers flank the novel BLB resistance helps in accurate prediction of the presence of the gene with less than 1% error. If the selection accuracy (calculated based on recombination frequencies observed in F_2 population) while using RM10975 and RMCG6 individually to predict BLB is 99.2% and 98.2%, respectively, then based on

the product rule of probability, the combined use of the markers RM10975 and RMCG6 enhances the selection efficiency to 99.03%. Biradar et al., (2004), in their efforts to tag and map a major, dominant rice gall midge resistance gene, *Gm1* have highlighted the utility of flanking markers in marker-assisted selection (MAS) of *Gm1*.

The utility of the SSR markers linked to the novel BLB resistance gene was validated in an alternative F_2 mapping population derived from the cross IR-65483-141-2-4-4-2-5-B /Samba Mahsuri. It was observed that the map location and linkage distances of the SSR markers were identical to those observed in the F_2 mapping population derived from the cross IR-65483-141-2-4-4-2-5-B /TN1, thus validating the linkage and utility of the flanking SSR markers. Marker validation studies help in testing the efficacy of flanking markers in predicting the presence of gene of interest in a different genetic background. Biradar *et al.*, (2004), Rathour *et al.*, (2008) and Sheeba *et al.*, (2005) validated the presence of *Gm1* (a rice gall midge resistance gene), *Pi-z*, (a blast resistance gene) and Rf, (a fertility restorer gene), respectively in alternate populations using SSR markers. Such validations are necessary for successful utilization of linked markers in marker-assisted breeding programs.

The present study relied on utilization of rice SSR markers for tagging and mapping of the new BLB resistance gene from the *Oryza brachyantha* introgression line (IR-65483-141-2-4-4-2-5-B). SSR markers have been widely used in tagging and mapping of the disease resistance genes in rice. A dominant gall midge resistance gene was tagged and mapped on Chr. 9 by using SSR markers (Biradar *et al.*, 2004). In addition to being helpful in tagging and coarse mapping, SSR markers are highly useful in fine

mapping also as demonstrated in the present study. Blair *et al.*, (2003) used SSR markers for fine mapping of the bacterial blight resistance gene *xa5* while Chu *et al.*, (2006a) used these markers for fine mapping *xa13* and recently Cheema *et al* , (2008) used these for fine mapping *Xa30(t).* In rice, so far more than 20,000 SSR markers have been identified and been mapped, both genetically and physically (IRGSP, 2005), giving an average saturation of one marker per 19.2 kb or one marker per ~0.1 cM. This coverage should be sufficient for fine mapping and map based cloning of agronomically important genes in rice. In fact, the genes *xa5* (Iyer and Mc Couch., 2004) and *xa13* (Chu *et al.*, 2006b) were cloned based on information derived from fine mapping analysis using SSR markers.

As on date, a total of 31 BLB resistance genes have been identified and most of these have been mapped on the rice genome using molecular markers (Laha *et al.,* 2009). In the present study, the new gene identified from *O. brachyantha* introgression line IR-65483-141-2-4-4-2-5-B has been mapped on Chr. 1 in the genomic region flanked by the two SSR markers, RM10975 (16.952Mb) and RMCG6 (16.968Mb).

In order to utilize the novel BLB resistance gene *Xa35t* effectively through marker-assisted breeding, it is imperative to study the amplification pattern of the flanking markers RM10975 and RMCG6 in a set of high priority bacterial leaf blight susceptible recipient lines into which the novel gene can be introgressed. With this objective, the amplfication pattern of the flanking markers RM10975 and RMCG6 was tested in a set of eight high priority, BLB susceptible rice varieties in order to assess the polymorphism of the two markers. Both RM10975 and RMCG6 displayed unique polymorphism between resistant donors and susceptible rice varieties and

hence can be considered highly useful either singly or in combination for marker-assisted introgression of *Xa35t* into high priority BLB susceptible rice cultivars.

In addition to tagging and fine mapping of *Xa35t*, in the present study, an attempt was made to analyze the genomic region flanked by the closest SSR markers RM10975 and RMCG6 for putatively expressed candidate genes through an *in-silico* approach. Such an *in-silico* approach was earlier used by Sharma *et al.*, (2005) for identification of the candidate gene involved in $Pi\text{-}k^h$ mediated resistance to blast. The genomic region of Japonica rice genome flanked by the closely linked SSR markers RM10975 and RMCG6 (spanning 16kb region) was downloaded and analyzed for putative candidate genes. A total of four genes were identified in the region analyzed of which two genes belonged to a No apical meristem super family, one was a hypothetical protein and one gene PTZoo265, a multidrug resistance gene. The No apical meristem gene can be assumed to be most probable candidate responsible for resistance in IR-65483-141-2-4-4-2-5-B based on its physical position and the segregation pattern of the closely linked markers RM10975 and RMCG6. The No apical meristem gene belongs to the NAC domain super family, the members of which are known to code for transcription factors (Ren *et al.*, 2000; Xie *et al.*, 1999; Duval *et al.*, 2002). NAC proteins are involved in transcriptional control of a variety of plant developmental processes, including formation of the shoot apical meristem, floral organs and lateral shoots (Souer *et al.*, 1996; Aida *et al.*, 1997; Xie *et al.*, 2000) as well as in plant hormonal control and in defense responses against stress and viral infections (Xie *et al.*, 1999; Ren *et al.*, 2000; Collinge and Boller, 2001; Nakashima *et al.*, 2007). Several NAC domains containing proteins have been reported to have plant resistance function in species like Chillies, Potato, Turnip and Rice (Ren *et al.*, 2000;

Collinge and Boller, 2001; Oh *et al.*, 2005; Lin *et al.*, 2007b). A NAC domain containing protein has been identified as the putative candidate for BLB resistance mediated by BLB resistance gene *Xa7* (Chen *et al.*, 2008) and for another gene reported to be allelic to *Xa7* in a japonica restorer line Zhenhui 084 (Zhang *et al.*, 2009).

Till date five BLB resistance genes have been identified from five wild rice species of rice namely *Xa21* identified from an accession of *O. longistaminata* (Khush *et al.*, 1990), *Xa23* from *O.rufipogon* (Zhang *et al.*, 1998), *Xa27* from *O. minuta* (Gu *et al.*, 2004), *Xa29* from *O.0fficinalis* (Tan *et al.*, 2004) and recently another gene, *Xa30t*, identified from the wild rice *O. nivara* (Cheema *et al.*, 2008). Similar to these efforts, through the present study, a novel BLB resistance gene, *Xa35t* has been identified from an introgression line of *O. brachyantha* (IR-65483-141-2-4-4-2-5-B), tagged and fine mapped on Chr. 1 using SSR markers. A set of putatively expressed genes, which could be candidate(s) for *Xa35t* and a set of very closely linked flanking SSR markers have been identified paving the way for marker-assisted introgression of the gene into elite rice varieties.

Identification and mapping of novel BLB resistance gene(s) from Ajaya :

In addition to the introgression line of *O. brachyantha* (IR-65483-141-2-4-4-2-5-B), in which a novel BLB resistance gene was identified through the present study, the popular BLB resistant check variety, Ajaya, which was released for cultivation by the Directorate of Rice Research was also observed to be resistant to most of the BLB isolates tested in the present study. The cultivar Ajaya is a medium duration (130-135 days) variety released for cultivation under irrigated ecosystems. Since its release in

1992, by the central varietal release committee it has performed well in the coordinated trials conducted by AICRIP and has been used as a national and an international check for screening the germplasm. Hence an effort was made to study the inheritance of BLB resistance in Ajaya and to identify, tag and map the resistance gene(s) present in Ajaya.

In order to study the inheritance of BLB resistance in Ajaya it was crossed with two BLB susceptible cultivars TN1 and Samba Mahsuri (BPT5204). The F_1s of both the crosses were observed to be intermediate to both the parents with respect to average lesion length indicating the involvement of incompletely dominant gene(s) in governing resistance. In the F_2 generation of the cross TN1/Ajaya consisting of 400 F_2 plants screened for BLB resistance, 25 were resistant (avg. lesion length < 4 cm), 105 were moderately resistant (avg. lesion length 4-8 cm), 132 were moderately susceptible (avg. lesion length 8-12 cm), 110 were susceptible (avg. lesion length 12-16 cm) and 28 were highly susceptible (avg. lesion length >16 cm). This fitted well in a segregation ratio of 1:4:6:4:1 (χ^2= 4.15, P=0.68) with respect to resistance , moderate resistance, moderate susceptibility, susceptibility and high susceptibility indicating the possible action of two incompletely dominant resistance genes with equal effects interacting additively (Figure 25). This can be considered as a case of quantitative inheritance of resistance governed by two loci. The classical example explaining such an interaction was grain color in Wheat by Nilsson-Ehle. On crossing two wheat genotypes possessing dark red and white grain colour, the F_1 showed light red grain colour and the F_2 segregated in the ratio of 1dark red:4medium red:6light red:4pale red :1white (Nilsson-Ehle 1909). Such interactions were also reported in case of inheritance of tolerance to high concentration of soil Boron in pea (Bagheri *et*

al., 1996), inheritance of palmitic acid content in soya bean (Erickson *et al.*, 1988) and inheritance of ray floret length in *Senecio cambrensis* (Ruth Ingram and Noltie, 1984).

Two earlier studies on inheritance of BLB resistance in Ajaya reported the action of two independently segregating dominant genes (Saini *et al.*, 1996) and a single recessive gene (Kameswara Rao *et al.*, 2003). However in our study the additive interaction between two incompletely dominant resistance genes was observed to condition resistance in Ajaya which was also validated in an alternate population. Additive /dosage effects has been reported between the BLB resistance genes *Xa1* and *Xa3* in Java14 (Kaku, 1997) and between *Xa1* and *Xa4* in the cultivar IR20 (Kaku, 1999). The increased level of resistance conferred by more than one gene governing resistance to a single pathogen race has been described as quantitative complementation (Sanchez *et al.*, 2000). The increased level of resistance of pyramided lines expressed as reduced lesion length has been reported in several gene-pyramiding studies on BLB resistance (Yoshimura *et al.*, 1995b; Huang *et al.*, 1997; Sanchez *et al.*, 2000; Singh *et al.*, 2001; Joseph *et al.*, 2004; Sundaram *et al.*, 2008; 2009). This increased resistance has been hypothesized to be due to synergistic action and/or complementation between the resistant genes used in the pyramid lines.

According to the pedigree of Ajaya (Figure 25), BLB resistance is thought to be contributed by one its parental line BJ1, a landrace reported to possess two resistance genes *xa5* and *xa13* (Ogawa and Yamamoto, 1986). Since genetic analysis in the F_2 mapping population revealed the action of two genes in conferring resistance in Ajaya, its allelic status was tested with respect to the *xa5* linked marker RG556 (Blair

and Mc Couch, 1997) and a functional marker for *xa13*, *xa13*-prom , (chu *et al.*, 2006b) along with two susceptible varieties TN1 and BPT5204. PCR Analysis with RG556 showed resistant allele specific amplification in Ajaya similar to IRBB5 while TN1 and BPT5204 amplified the susceptible allele indicating that *xa5* could be one of the genes conferring resistance in Ajaya. Davierwala *et al.*, (2001) predicted the possible presence of *xa5* in Ajaya and several other rice varieties based on PCR analysis with RG556. Analysis with *xa13*-prom primer showed amplification of susceptibility specific allele in Ajaya similar to TN1 and BPT5204 indicating that the second resistance gene in Ajaya is not *xa13*. Based on these observations, it can be assumed that while Ajaya may possess *xa5* gene inherited from BJ1, it certainly does not possess *xa13*, since the functional marker for the gene, *xa13*-prom did not reveal amplification of the resistance linked allele in Ajaya.

In order to confirm the presence of *xa5* in Ajaya, allelism test was carried out with IR24 NIL carrying recessive resistance genes *xa5*. The F_2 population derived from the cross Ajaya/IRBB5 was uniformly resistant and did not segregate for susceptibility indicating that *xa5* is one of the genes conferring resistance in Ajaya. In case of the gene *xa5*, the functional polymorphism specific for resistance was due to a 2-bp pair substitution, i.e. TC (susceptible genotypes) to AG (resistant genotypes) in the exon-2 of the candidate gene for *xa5*, Transcription factor IIAγ, leading to a change in a single amino acid i.e. Valine (susceptible) to Glutamic acid (resistant) as reported by Iyer and Mc Couch *et al.*, (2004). Sequence analysis of the 260 bp fragment amplified in this functional polymorphic region of the second exon of *xa5* in Ajaya showed AG substitution while the susceptible genotypes TN1 and BPT5204 showed TC

substitution. Thus from the results of the present study, it is conclusively clear that one of BLB resistance genes in Ajaya is *xa5*.

In an earlier study Kameswara Rao *et al.*, (2003) reported presence of a gene, which is non-allelic to *xa5* to be responsible for resistance in Ajaya and mapped it on the long arm of Chr. 5 between the markers RM39 (14.5cM from the gene) and RM31 (17.7cM from the gene), while *xa5* was mapped on the short arm of Chr. 5 (Blair and McCouch, 1997). However in the present study, through all the three approaches followed, i.e. marker analysis with RG556, allelism tests with IRBB5 and sequence analysis of the functional polymorphic region of *xa5* proved that *xa5* is indeed one of the candidate genes in Ajaya. The better level of resistance shown by Ajaya (displaying avg. lesion length of 3.87 cm) when compared to IRBB5 (a NIL harboring *xa5*, which displayed avg. lesion length of 7.08 cm) is because of the additive effect of the second resistance gene as evident from the F_2 genetic analysis. The recessive nature of resistance conferred by *xa5* was reported by Murthy and Khush, (1972), Olufowote *et al.*, (1977) and Blair *et al.*, (2003). However in the present study, *xa5* exhibited incomplete dominance confirming the results as obtained by Li *et al.*, (2001), who also observed incomplete dominance of *xa5*.

Since one of the resistance genes in Ajaya was identified to be *xa5*, and the interaction between the two resistance genes was observed to be additive, the genotype of each of the 400 F_2 individuals with respect to the second resistance locus was predicted based on both the F_3 segregation data and marker genotype at *xa5* locus as under

- The 25 resistant plants in the F_2 population of the cross TN1/Ajaya were assumed to have the genotype r1r1r2r2 (as they were uniformly resistant and

showed no segregation in the F_3) and were predicted to be homozygous (r2r2) at the second resistance locus as they showed homozygous resistant (r1r1) amplification at *xa5* locus

- The 50 moderately resistant plants whose genotype was assumed to be r1r1R2r2/R1r1r2r2 (as their F_3 segregated in the ratio of 1R:2MR:1S) were supposed to be heterozygous at the second locus (R2r2), as they were homozygous resistant (r1r1) with respect to *xa5* locus
- The second set of 55 moderately resistant plants whose genotype was assumed to be R1r1r2r2 were supposed to be homozygous resistant (r2r2) at the second locus as they were heterozygous with respect to *xa5* (R1r1)
- The 20 moderately susceptible plants whose F_3 progeny lines were uniformly moderately susceptible with out any segregation in the F_3 were assumed to be homozygous at both the loci and supposed to have the genotype r1r1R2R2. Their genotype at the second resistance locus was predicted to be homozygous susceptible(R2R2) as they showed homozygous resistant (r1r1)amplification with respect to *xa5*
- The 24 moderately susceptible plants whose F_3 progeny lines were uniformly moderately susceptible with out any segregation in the F_3 were assumed to have the genotype R1R1r2r2 and their corresponding second resistance locus was predicted to be homozygous resistant (r2r2) as they were homozygous susceptible (R1R1) at *xa5* locus
- The 88 moderately susceptible plants whose F_3 progeny lines segregated in1R:4MR:6MS:4S:1HS ratio were assumed to be heterozygous at both the genic loci and supposed to have the genotype R1r1R2r2. Their second

resistance locus was predicted to be heterozygous (R2r2) as they showed heterozygous susceptible amplification (R1r1) with respect to *xa5*

- The 50 Susceptible plants whose F_3 progeny lines segregated in1HS:2S:1MS ratio were assumed have the genotype R1r1R2R2/R1R1R2r2 and were predicted to be heterozygous (R2r2) as they were homozygous susceptible (R1R1) at *xa5* locus
- The second set of 60 susceptible plants were assumed have the genotype R1r1R2R2/R1R1R2r2 and were predicted to be homozygous susceptible (R2R2) at the second resistance locus as they were heterozygous susceptible (R1r1) at *xa5* locus
- All the 28 highly susceptible plants whose progeny was uniformly susceptible and showed no segregation in the F_3 were assumed to be homozygous at both the resistance loci and their genotype was supposed to be R1R1R2R2. Their genotype with respect to the second resistance locus was predicted to be homozygous susceptible (R2R2) as they were homozygous susceptible (R1R1) with respect to *xa5*

The genotype of each of the individual F_2 plants of the population of the cross TN1/Ajaya with respect to the second resistance locus as predicted from the F_3 segregation and marker data at *xa5* locus (RG556) was used for mapping the second resistance in Ajaya

In order to study the precise location of the second resistance gene in Ajaya, a parental polymorphism survey was carried out with a set of 282 SSR markers covering the 12 chromosomes of rice. Out of 282 primers tested, only 77 were observed to be polymorphic. The marker RM23476 located at 26.26 Mb on Chr. 8 showed bulk specific amplification and when checked in the whole mapping

population, was observed to be at a linkage distance of 15.1 cM In order to identify the map location of the second resistance gene in Ajaya on Chr. 8, 30 SSR markers in the vicinity of RM23476 were tested for parental polymorphism, of which, 10 were polymorphic. When these polymorphic SSRs were then tested for their marker-trait segregation pattern in the F_2 mapping population, two markers *viz.*, RM23478 and RM23535 were observed to be the closest and flanking the novel gene at a genetic distance of 14.8 and 15.1 cM respectively. These two markers helped to narrow down the gene to a physical region of 800 Kb on Chr. 8, thus serving as a starting point for fine-mapping analysis. Fine-mapping analysis was carried out with a set of nine hyper-variable SSR markers and six newly designed SSR markers (RMAFM1 to RMAFM6) located in the genomic region spanned by RM23478 and RM23535. The gene was mapped in the marker interval of RM447 and RMAFM1 with both of them flanking it. This gene, which has been mapped approximately at a distance of 100 Kb from another gene on Chr.8 i.e. *xa13* can be considered as novel, since no other BLB resistance gene has been reported in this region and hence it was designated as *xa36(t)*. The markers RM23489, RM23496, RMAFM2 and RMAFM1 were observed to be located on one side of the gene at a genetic distance of 13.6 cM, 12.2 cM, 4.3 cM and 1.9 cM respectively, while RM447, RMAFM4, RMAFM5 and RMAFM6 were located on the other side of the gene at a genetic distance of 0.87 cM, 3.1 cM, 6.2 cM and 10.1cM respectively. The closest flanking markers RM447 and RMAFM1 span a physical distance of 13 kb which could serve as the starting point for *in-silico* identification of putative candidates for *xa36t* and possibly, map based cloning of the gene.

There were only four recombinants out of 400 F_2 plants analyzed with respect to the marker RM447 while five recombinants were observed with respect to the marker RMAFM1. Even though the two markers showed a few recombinants, their flanking nature helps them for effective use in marker-assisted selection. The selection efficiency of the marker RM447 was observed to be 99.2% as it is at a genetic distance of 0.8 cM from the gene while that for RMAFM1, it was 98.2% as it is 1.8cM from the gene. The combined use of the flanking markers RM447 and RMAFM1 enhances the selection efficiency to 99.03%, based on the product rule of probability (Biradar et al., 2004). In fact, in the present study, a total of 102 F_2 plants possessed Ajaya specific allele for both RM447 and RMAFM1 in homozygous condition and all these plants were observed to be homozygous resistant, indicating the utility of flanking markers in screening for resistance trait. Since RM447 was monomorphic between Ajaya and BPT5204 the other closely linked markers RMAFM2, RMAFM1, RMAFM4 and RMAFM5 were validated in the alternative F_2 mapping population derived from the cross Samba Mahsuri/Ajaya. It was observed that the map location and linkage distances of the SSR markers were identical to those observed in the F_2 mapping population derived from the cross TN1/Ajaya , thus validating the linkage and utility of the flanking SSR markers.

In the present study, the new gene identified from Ajaya and fine mapped on Chr. 8 at a distance of ~100 kb from *xa13* has been tentatively named as *xa36t*. The utility of the flanking markers identified, for marker assisted introgression of the *xa 36t* gene was evaluated by studying their amplification pattern in a set of high priority bacterial leaf blight susceptible recipient lines into which the novel gene can be introgressed. The flanking marker combination of RM447-RMAFM1 can be used for introgression

of the gene from Ajaya in to susceptible cultivars TN1, MTU1001, Krishnahamsa and Basmati370 as these markers were polymorphic between the Ajaya and the recipient parents. Since the marker RM447 was monomorphic between Ajaya and BPT5204, Swarna, MTU1010, Tellahamsa and IR64, the flanking marker combination of RMAFM1 and RMAFM4 is suggested for marker-assisted introgression of this gene to the above mentioned susceptible rice cultivars. Since both the markers RM447 and RMAFM1 were monomorphic between Ajaya and MTU1010, the marker RMAFM4 can be used singly or in combination with the other relatively closer polymorphic markers for introgression of *xa36t*.

The genomic region flanked by the closest SSR markers RM447 amd RMAFM1was analysed for putative candidate genes through an *in-silico* approach. The genomic region of Japonica rice genome flanked by the the markers RM447 amd RMAFM1 (~ 13Kb) was downloaded and analyzed for putative candidate genes. A total of three genes were identified in the region analyzed. Gene density within this region is about one gene every 4.3 kb, against the published predictions of one gene every 9.9 kb (International Rice Genome Sequencing Project 2005). One of the genes identified in this genomic region belonged to Nodulin super family. The candidate gene for *xa13* has been identified to be a nodulin gene, which are usually expressed in the root nodules of plants belonging to leguminosae family (chu *et al.*, 2006b). Nodulin related genes are found in several species like nematodes, insects, and animals, although the biochemical functions of their proteins are unknown. Yang *et al.*, (2006) reported about 17 nodulin related genes distributed all over the rice genome. It is hypothesized that the nodulin gene identified in the present study, which is mapped at a distance of about 100kb away from *xa13* could be one of the candidates for *xa36t*. The second

gene which was observed to be the most probable candidate for *xa36t* based on the segregation of the closely linked flanking markers was SUA7, a gene from *Sacharomyces cerevisiae* (yeast), which codes for the general transcription factor TFIIB which is involved in the transcription of genes in interaction with the enzyme RNA Polymerase II. A related factor of TFIIB called the BRF1 acts as a subunit and of the yeast transcription factor TFIIIB and plays a role in RNA Polymerase III initiation analogous to the role played by TFIIB for RNA polymerase II in its interaction with TATA Box Binding protein (Colbert and Hahn, 1992). The other gene identified in the genomic region of interest was a plant peroxidase gene. Peroxidases are involved in lignin biosynthesis whose accumulation was observed in the resistance mediated by BLB resistance genes *xa5, Xa7*, and *Xa10* (Reimers and Leach, 1991). Although the role for peroxidases in defense responses has not been clearly demonstrated, increases in peroxidase activity have been correlated with infection in many plant species. Peroxidases are involved in production of active oxygen species, which may play various roles in reduction of pathogen viability and spread (Mehdy *et al.*, 1996; Tenhaken *et al.*, 1995). In rice, induction of specific peroxidases has been correlated with resistance to BLB (Chittoor *et al.*, 1997; Hilaire *et al.*, 2001). Cloning and sequencing of the above said putative candidate genes for *xa36t* may help in precisely identifying and characterizing the candidate gene associated with resistance controlled by *xa36t.*

In general, the 'R' proteins are predicted to act as receptors to bind specifically to a pathogen produced ligand, which is produced directly or indirectly by the *avr* gene present in the pathogen. This direct interaction of the 'R' protein and *Avr* ligand results in activation of the plant defense response, which ultimately results in the expression

of resistance. Therefore, the function of the 'R' gene depends on the presence of a recognizable *Avr* ligand in the pathogen. The *Avr* ligands, which may be interacting with *Xa35t and Xa36t,* need to be identified through intensive host-pathogen interaction studies

Out of the five dominant BLB resistance genes identified from five wild rice species i.e. *Xa21* from *O.longistaminata*, *Xa 23* from *O rufipogon*, *Xa27t* from *O minuta, Xa 29t* from *O.officinalis* and *Xa30t* from *O.nivara*, *Xa21* is the most effective and the most deployed resistance gene in rice genotypes. The gene has been introgressed into many elite rice varieties like PR106 (Singh *et al.*, 2001), Pusa Basmati1 (Joseph *et al*, 2004), Samba Mahsuri (Sundaram *et al.*, 2008), Swarna and IR64 and many hybrid rice parental lines like Minghui 63 (Chen *et al.*, 2000), Zhenshan 97A (Zhang *et al.*, 2002). Recently, *Xa30t* identified from an *O. nivara* accession (Cheema *et al.*, 2008) was introgressed into the variety PR114. The novel resistance gene, *Xa35t* identified from an introgression line of *O. brachyantha* in the present study could complement the resistance mediated by *Xa21* in hybrid rice. The genes *Xa35t* and *xa36t* can be deployed either singly or in combination with other major BLB resistance genes *xa5*, *xa13* and *Xa21* to obtain broad spectrum resistance against BLB. The tightly linked flanking markers developed in the present study can be used to track the introgression of these genes in to elite backgrounds. The, putatively expressed genes, which could be candidates for *Xa35t* and *xa36t*, could help in Map based cloning and functional dissection of the novel genes identified.

Chapter 6

Summary & conclusions

VI – Summary and Conclusions

Bacterial leaf blight of rice caused by *Xanthomonas oryzae* pv *oryzae* is one of the most destructive diseases of rice in majority of the rice growing countries especially in Asia. Since chemical control of the disease is not economical, cultivation of rice varieties possessing one or more bacterial blight resistance genes has been recommended. So far 31 Bacterial leaf blight resistance genes have been identified. Extensive cultivation of varieties containing single resistance genes has resulted in frequent breakdown of resistance due to emergence of virulent strains of the disease across many locations in India. Therefore there is a need for continuous search for the new/novel sources of resistance and their introgression along with major BLB resistance genes in to elite varieties to achieve durable resistance. The present study was thus carried out with the objective of identification and mapping of novel bacterial leaf blight (BLB) resistance gene(s) in rice.

The results obtained from the present study are summarized as follows:

- 72 wild rice introgression lines carrying introgressions from the wild species *O. nivara*, *O. rufipogon, O. longistaminata*, *O. glaberrima*, *O. officinalis* and *O. brachyantha* obtained from International Rice Research Institute and the international BLB resistant check variety Ajaya were screened for bacterial leaf blight resistance with seven hyper virulent isolates collected from different parts of India. One *O. brachyantha* introgression line namely IR-65483-141-2-4-4-2-5-B, and the elite variety Ajaya were found to be resistant consistently with all the

isolates tested when compared with susceptible checks, i.e., TN1, Samba Mahsuri (BPT5204), Swarna and MTU1010.

- Genetic analysis in the F_2 population of both the crosses TN1/ IR-65483-141-2-4-4-2-5-B and BPT/ IR-65483-141-2-4-4-2-5-B revealed the action of a single dominant gene in governing resistance in IR-65483-141-2-4-4-2-5-B
- In order to assess whether the resistance gene in IR-65483-141-2-4-4-2-5-B was allelic to any of the known dominant BLB resistance genes, it was crossed with near isogenic lines of IR24 possessing known single dominant BLB resistance genes, *viz.*, IRBB1, IRBB4, IRBB7, IRBB21 and IRBB26. The F_1s derived from these crosses segregated for BLB resistance in a typical ratio of 15:1 (resistant: susceptible) indicating that the resistance gene in IR-65483-141-2-4-4-2-5-B was different from *Xa1, Xa4, Xa7, Xa21* and *Xa26* and could be novel.
- In order to tag and map the dominant BLB resistance gene in IR-65483-141-2-4-4-2-5-B bulked-segregant analysis was carried out at F_2 generation using 106 parental polymorphic SSR markers spread across the 12 rice chromosomes.
- The SSR marker RM595 located on chromosome 1, showed bulk specific amplification. This marker when tested with the individuals constituting the bulks and the remaining individuals of the F_2 mapping population for cosegregation, showed a linkage distance of 10.2cM from the gene.
- Since no other previous study has reported presence of any dominant BLB resistance gene on Chr. 1 and since the BLB resistance gene identified in IR-65483-141-2-4-4-2-5-B was non-allelic to the known dominant BLB resistance genes, it was assumed that the gene is novel and was tentatively named as *Xa35t.*

- Linkage analysis with, a set of 37 SSR markers in the vicinity of RM595 mapped *Xa35t* in the marker interval of RM10975 (0.82cM) and RMCG6(1.8cM). The markers RM10920, RM10963, RMCG5 RM10974 and RM10975 were observed to be located on one side of the gene at a genetic distance of 9.4 cM, 7.5 cM, 6 cM 1.85 cM and 0.82cM respectively while RMCG6, RMCG7 and RMCG8 were located on the other side of the gene at a genetic distance of 1.8 cM, 5.6 cM, and 8.4 cM respectively
- In order to validate the linkage distances of the identified markers, they were analyzed for their segregation pattern in a progeny tested alternate mapping population consisting of 250 F_2 individuals derived from the cross BPT5204/ IR-65483-141-2-4-4-2-5-B. The linkage distances of the closely linked markers were observed to be identical to those observed in the mapping population derived from the cross TN1/ IR-65483-141-2-4-4-2-5-B thus validating these markers.
- The amplification pattern of the closest markers RM10975 and RMCG6 was analyzed in a set of high priority BLB susceptible rice varieties along with IR-65483-141-2-4-4-2-5-B. Both RM10975 and RMCG6 displayed polymorphism between BLB resistant and susceptible genotypes indicating the possibility of using these markers either individually or together in marker-assisted transfer of *Xa35t* into elite rice varieties.
- The physical interval flanked by the closest markers RM10975and RMCG6 was analyzed *in silico* for putatively expressed candidate genes. A set of four genes were identified in this interval of which a gene encoding a No apical meristem protein appears to be the best candidate for *Xa35t*.

- A study on the inheritance of resistance in Ajaya using the F_2 populations of the crosses TN1/Ajaya and BPT/Ajaya revealed an additive interaction between two incompletely dominant genes with equal effects
- According to the pedigree of Ajaya its resistance was conferred by 2 genes, *xa5* and *xa13* contributed by one its parental line BJ1. The allelic status of Ajaya was therefore tested with respect to linked markers to *xa5* (RG556) and *xa13* genes (*xa 13* prom). PCR analysis with RG556 showed resistant specific amplification in Ajaya as in IRBB5 while analysis with xa13 promoter primer showed susceptible specific amplification as in TN1 and BPT5204. This indicated that one of the two resistance genes in Ajaya could be allelic to *xa5* and the other non allelic to *xa13.*
- In order to further assess whether Ajaya possessed *xa5*, allelism test was conducted with a near isogenic line of IR24 possessing the BLB resistance gene *xa5* (IRBB5). The F_2 progeny of the cross Ajaya /IRBB5 was uniformly resistant with out any segregation indicating that one of the resistance genes in Ajaya is *xa 5.* Sequence analysis of the functional polymorphic region in the second exon of *xa5* in Ajaya further proved the presence of *xa5.*
- The 400 F_2 individuals of the population of the cross TN1/Ajaya were genotyped with respect to RG556 and this data was used along with the F_3 segregation data to predict the genotype at the second resistance locus.
- Bulked-segregant analysis carried out using 77 parental polymorphic SSR markers spread across the 12 rice chromosomes revealed the linkage of the second

resistance gene in Ajaya with an SSR marker RM23476 located on Chromosome 8 (26. 26Mb) which showed a genetic distance of 15.1cM.

- Linkage analysis with, a set of 45 SSR markers in the vicinity of RM23476 mapped the gene in the marker interval of RMAFM1 and RM447. The markers RM23489, RM23496, RMAFM2 and RMAFM1 were observed to be located on one side of the gene at a genetic distance of 13.6 cM, 12.2 cM, 4.3 cM and 1.9 cM respectively , while RM447, RMAFM4, RMAFM5 and RMAFM6 were located on the other side of the gene at a genetic distance of 0.87 cM, 3.1 cM, 6.2 cM and 10.1cM respectively
- Since RM447 was monomorphic between the parents Ajaya and BPT5204. The other closer and flanking markers RMAFM1, RMAFM2, RMAFM4, and RMAFM5 were checked for their validity in the alternate population of the cross BPT5204/Ajaya. These markers showed similar marker order and identical linkage distances with the gene as in the main population of the cross TN1/Ajaya and the gene could be precisely mapped in between the markers RMAFM1 and RMAFM4.
- The utility of the flanking markers identified, for marker assisted introgression of the *xa 36t* gene was evaluated by studying their amplification pattern in a set of high priority bacterial leaf blight susceptible recipient lines into which the novel gene can be introgressed. The flanking marker combination of RM447-RMAFM1 can be used for introgression of the gene from Ajaya in to susceptible cultivars TN1, MTU1001, Krishnahamsa and Basmati370 as these markers were polymorphic between Ajaya and the recipient parents. Since the marker RM447

was monomorphic between Ajaya and BPT5204, Swarna, MTU1010, Tellahamsa and IR64, the flanking marker combination of RMAFM1 and RMAFM4 is suggested for marker-assisted introgression of this gene to the above mentioned susceptible rice cultivars. Since both the markers RM447 and RMAFM1 were monomorphic between Ajaya and MTU1010, the marker RMAFM4 can be used singly or in combination with the other relatively closer polymorphic markers for introgression of *xa36t.*

- The physical interval flanked by the closest markers RM447 and RMAFM1 was analyzed *in silico* for putatively expressed candidate genes. A set of three genes were identified in this interval of which a gene from yeast, SUA7 encoding the transcription factor TFIIB appears to be the best candidate for *xa36t.*

To conclude, from the present study, two novel BLB resistance genes *Xa35t,* a dominant gene from an introgression line of *O. brachyantha* i.e. IR-65483-141-2-4-4-2-5-B, tagged and fine mapped on Chr.1 and *xa36t,* an incompletely dominant gene from Ajaya, tagged and fine mapped on Chr.8 using SSR markers were identified. Further, putative candidate genes which could be possibly associated with *Xa35t* and *xa36t* mediated resistance have also been identified.

Chapter 7

List of References

Chapter VII – List of References

Abenes MLP, Angeles ER, Khush GS and Huang N. Selection of bacterial blight resistant rice plant in the F_2 generation via their linkage to molecular markers. **Rice Genet Newsl**. 10: 120–3, 1993

Adhikari TB, Vera Cruz CM, Zhang Q, Nelson RJ Skinner DZ, Mew TW and Leach JE. Genetic diversity of *Xanthomonas oryzae* pv. *oryzae* in Asia. **Appl Environ. Microbiol** 61: 966–971, 1995

Aida M, Ishida T, Fukaki H, Fujisawa H and Tasaka M. Genes involved in organ separation in Arabidopsis: an analysis of the cup-shaped cotyledon mutant. **Plant Cell** 9: 841–857, 1997

Altschul SF, Gish W, Miller W, Myers EW and Lipman DJ. Basic local alignment search tool. **J Mol Biol** 215: 403-410, 1990

Amante-Bordeos A, Sitch LA, Nelson R, Dalmacio RD, Aswindinoor H and Leung H. Transfer of bacterial blight and blast resistance from the tetraploid wild rice *Oryza minuta* to cultivated rice *Oryza sativa*. **Theor. Appl. Genet**.84: 345-354, 1992

Ardales EY, Leung H, Vera Cruz CM, Mew TW, Leach JE and Nelson RJ. Hierarchical analysis of spatial variation of the rice bacterial leaf blight pathogen across diverse agro-ecosystems in the Philippines. **Phytopathology** 86: 241-252, 1996

Arumuganathan K and Earle ED. Nuclear DNA content of some important plant species. **Plant Mol. Biol. Rep**. 9: 208–218, 1991

Babujee L and Gnanamanickam SS. Molecular tools for characterization of rice blast pathogen (*Magnaporthe grisea*) population and molecular marker-assisted breeding for disease resistance. **Curr Sci** 78: 248-257, 2000

Bagheri A, Paull JG and Rathjen AJ. Genetics of tolerance to high concentrations of soil boron in peas (Pisum sativum L.) **Euphytica** 87(1): 69-75, 1996

Bhapkar DG, Kulkarni NB and Chavan VM 1960. Bacterial blight of paddy. **Poona Agricultural College Magazine** 51: 36-46.

Biradar SK, Sundaram RM, Thirumurugan T, Bentur JS, Amudhan S, Shenoy VV, Mishra B, Bennett J and Sarma NP. Identification of flanking SSR markers for a

major rice gall midge resistance gene *Gm1* and their validation. **Theor Appl Genet** 109: 1468–1473, 2004

Blair MW and McCouch SR. Microsatellite and sequence tagged site markers diagnostic for the rice bacterial blight resistance gene xa5. **Theor Appl Genet** 95: 174-185, 1997

Blair MW, Garris AJ, Iyer AS, Chapman B, Kresovich S and McCouch SR. High resolution genetic mapping and candidate gene identification at the xa5 locus for bacterial blight resistance in rice (Oryza sativa L.). **Theor Appl Genet** 107: 62–73, 2003

Brar DS and Khush GS. Alien introgression in rice. **Plant Mol. Biol**. 35: 35-47, 1997

Brinda Priyadarsini V and Gnanamanickam SS. Occurrence of a subpopulation of *Xanthomonas oryzae* pv. *oryzae* with virulence to rice cultivar IRBB21 in Southern India. **Plant Dis**. 83: 781, 1999

Cheema KK, Grewal NK, Vikal Y, Sharma R, Lore JS, Das A, Bhatia D, Mahajan R, Gupta V, Bharaj TS and Singh K. A novel bacterial blight resistance gene from *Oryza nivara* mapped to 38 kb region on chromosome 4 and transfered to *Oryza sativa* L. **Genetical Research** 90: 1-11, 2008

Chen H, Wang S and Zhang Q. New gene for bacterial blight resistance in rice located on chromosome12 identified from Minghui 63, an elite restorer line. **Phytopathology** 92: 750–754, 2002

Chen S, Huang Z, Zeng L, Yang J, Liu Q and Zhu X. High-resolution mapping and gene prediction of Xanthomonas Oryzae pv. Oryzae resistance gene Xa7.**Mol Breeding** 22: 433–441, 2008

Chen S, Lin XH, Xu CG and Zhang QF. Improvement of bacterial blight resistance of Minghui 63 an elite restorer line of hybrid rice, by molecular marker-assisted selection. **Crop Sci** 40: 239–44, 2000

Chen X, Temnykh S, Xu Y, Cho Y G and Mc Couch SR. Development of a microsatellite frame work map providing genome wide coverage in rice (*Oryza sativa* L.). **Theor Appl Genet 95**: 553-567, 1997b

Chen XW, Shang JJ, Chen DX, Lei CL, Zou Y, Zhai WX, Liu GZ, Xu C, Ling ZZ, Ma BT, Wang YP, Zhao XF, Li SG and Zhu LH. A B-Jectin receptor kinase gene conferring rice blast resistance. **Plant.** 46: 794- 804, 2006

Chittoor JM, Leach JE and White FF. Differential inductionof a peroxidase gene family during infection of rice by *Xanthomonasoryzae* pv. *oryzae*. **Mol. Plant-Microbe Interact**. 10: 861-871, 1997

Cho YG, Eun MY, McCouch SR and Chae YA. The semi-dwarf gene, *sd-1*, of rice (*Oryza sativa* L.). II. Molecular mapping and marker-assisted selection. **Theor Appl Genet** 89: 54-59, 1994

Chu Z, Fu B, Yang H, Xu C, Li Z, Sanchez A, Park YJ, Bennetzen JL, Zhang Q and Wang S. Targeting *xa13*, a recessive gene for bacterial blight resistance in rice. **Theor Appl Genet** 112: 455-461, 2006a

Chu Z, Yuan M, Yao J, Ge X, Yuan B, Xu C, Li X, Fu B, Li Z, Bennetzen JL, Zhang Q and Wang S. Promoter mutations of an essential gene for pollen development result in disease resistance in rice. **Genes and Dev** 20: 1250-1255, 2006b

Colbert T and Hahn S. A yeast TFIIB-related factor involved in RNA polymerase III transcription. **Genes Dev** 6: 1940-1949, 1992

Collinge M and Boller T. Differentiation induction of two potato genes, Stprx2 and StNAC, in response to infection by Phytophthora infestans and to wounding. **Plant Mol Biol** 46: 521–529, 2001

Davierwala AP, Reddy APK, Lagu MD, Ranjekar PK and Gupta VS. Marker Assisted Selection of Bacterial Blight Resistance Genes in Rice. **Biochemical genetics** 39 (7): 261-278, 2001

Deragon JM and Landry BS. RAPD and other PCR-based analyses of plant genomes using DNA extracted from small leaf discs. **PCR Methods Appl** 1: 175-180, 1992

Duval M, Hsieh TF, Kim SY and Thomas TL. Molecular characterization of AtNAM: a member of the Arabidopsis NAC domain superfamily. **Plant Mol Biol** 50: 237–248, 2002

Erickson EA,. Wilcox JR, and Cavins JF. Inheritance of Altered Palmitic Acid Percentage in Two Soybean Mutants. **Journal of heredity** 79(6):465-468, 1988

Ezuka A and Sakaguchi S. Host-Parasite relationship in bacterial leaf blight of rice caused by *Xanthomonas oryzae. Rev.* **Plant Protect. Res.** 11: 93-118, 1978

Flor H. Current status of the gene-for-gene concept. **Annu Rev Phytopathol** 9: 275-296, 1987

Fujita D, Doi K, Yoshimura A, Yasui H. Molecular mapping of a novel gene Grh5 conferring resistance to rice green leaf hopper (*Nephotettix cincticeps* Uhler) in rice. Oryza sativa L. **Theor. Appl. Genet.** 113: 567-573, 2006

Gao DY, Xu ZG, Chen ZY, Sun LH, Sun QM, Lu F, Hu BS, Liu YF and Tang LH. Identification of a new gene for resistance to bacterial blight in a somaclonal mutant HX-3 (indica). **Rice Genet Newsl** 18: 66–68, 2001

George MLC, Bustamam M, Cruz WT, Leach JE and Nelson RJ. Movement of *Xanthomonas oryzae* pv. *oryzae* in Southeast Asia Detected Using PCR-Based DNA Fingerprinting. **Phytopathol** 87(3): 302-309, 1997

Gnanamanickam SS, Pryiyadarasani V, Narayanan NN, Vasudevan P and Kavitha D. An overview of bacterial blight disease of rice and strategies for management. **Current Science** 77: 1435-1444, 1999

Goel RK, Kaur L and Saini RG. Effectiveness of different *Xa* genes against *Xanthomonas oryzae* pv. *oryzae* population causing bacterial blight of rice in Punjab (India). **Rice Genet Newsl** 15: 131–133, 1998

Gomez and Gomez. Statistical procedures for agricultural research. *John Wiley and Sons* 458-477, 1976

Goto M. Kresek and pale yellow leaf systemic symptoms of bacterial leaf blight of rice caused by Xanthomonas oryzae (Uyeda and Ishiyama). **Plant Disease Reporter** 48: 858-861, 1964a

Gu K ,Tian D, Yang F , Wu C , Sreekala C, Wang GL and Wang Z Y. High-resolution genetic mapping of Xa27(t), a new bacterial blight resistance gene in rice, Oryza sativa L. **Theoretical and applied genetics** 108: 800-807, 2004

Gu K, Yang B, Tian D, Wu L, Wang D, Sreekala C, Yang F, Chu Z, Wang G, White FF and Yin Z. R gene expression induced by a type-II effector triggers disease resistance in rice. **Nature** 435: 1122-1125, 2005

Gupta AK, Sharma SC and Saini RG. Variation in pathogenesity of some Indian isoaltes of *Xathomonas compestris* pv. *Oryzae*. **Phytopathology** 776: 881-883, 1986

Gupta VS, Ramakrishna W, Rawat SR and Ranjekar PK. (CAC)5 detects DNA fingerprints and sequences homologous to gene transcripts in rice. **Biochemical Genetics** 32: 1-8, 1994

Haley SD, Afandor LK, Miklas PN, Stavely JR and Kelly JD. Heterogenous inbred populations are useful as a source of near isogenic lines for RAPD marker locations. **Theor Appl Genet** 88: 337-342, 1994

Hilaire E, Young SA, Willard LH, McGee JD, Sweat T, Chittoor JM, Guikema J and Leach JE. Vascular defense responses in rice: Peroxidase accumulation in xylem parenchyma cells and xylem wall thickening. **Mol. Plant-Microbe Interact.** 14: 1411-1419, 2001

Himabindu K, Sundaram RM, Neeraja CN, Mishra B and Bentur JS. Flanking SSR markers for allelism test for the Asian rice gall midge (*Orseolia oryzae*) resistance genes. **Euphytica** 157: 267–279, 2007

Hittalmani S, Foolad M, Mew T, Rodriguez R and Huang N. Identification of blast resistance gene, *Pi*-2t in rice plants by flanking DNA markers. **Rice Genet Newsl** 11: 144-146, 1994

Hittalmani S, Kumar GK, Kulkarni N and Sashidhar HE. DNA markers assist in reducing the number of generations of backcrosses in breeding for blast resistance in rice. *In: Proceedings of the International Program on Rice Biotechnology, Sept 20-24, Phuket, Thailand.* 21, 1999

Hittalmani S, Parco A, Mew TV, Zeigler RS and Huang N. Fine mapping and DNA marker-assisted pyramiding of the three major genes for blast resistance in rice. **Theor Appl Genet** 100: 1121-1128, 2000

Holt BF, Boyes DC, Ellerstrom M, Siefers N and Wiig A. An evolutionarily conserved mediator of plant disease resistance gene function is required for normal Arabidopsis development. **Dev. Cell** 2: 807–817, 2002

Hopkins CM, White FF, Choi SH, Guo A, Leach JE. A family of avirulence genes from Xanthomonas oryzae pv oryzae. **Mol Plant-Microbe Interact** 5: 451–9, 1992

Huang N, Angeles ER, Domingo J, Magpantay G, Singh S, Zhang G, Kumaravadivel N, Bennett J and Khush GS. Pyramiding of bacterial blight resistance genes in rice: marker assisted selection using RFLP and PCR. **Theor Appl Genet** 95: 313-320, 1997

IRGSP. The map based sequence of the rice genome. **Nature** 436: 793-800, 2005

IRRI. International Rice Research Institute. *Annual Report* for 1972, Los Banos, Philippines. 127-132, 1973

Ishiyama S. Studies on the white leaf disease of rice plants. Report of the Agricultural Experiment Station, Tokyo. 45: 233-251, 1922

Iyer AS and McCouch SR. The rice bacterial blight resistance gene *xa5* encodes a novel form of disease resistance. **Mol Plant Microbe Interact** 17: 1348–1354, 2004

Jena KK and Khush GS. Introgression of genes from *Oryza officinalis* Well ex Watt to cultivated rice, *O. sativa* L. **Theor. Appl. Genet.** 80: 737-745, 1990

Jeung JU, Kim BR, Cho YC, Han SS, Moon HP, Lee YT and Jena KK. A novel gene, *Pi40*(t), linked to the DNA markers derived from NBS-LRR motifs confers broad spectrum of blast resistance in rice. **Theor Appl Genet** 115(8): 1163-77, 2007

Jia Y, Wang Z and Singh P. Development of dominant rice blast Pi-ta resistance gene markers. **Crop Sci** 42: 2145–2149, 2002

Joseph MS, Gopalakrishnan RK, Sharma VP, Singh AK, Singh NK and Mohapatra T. Combining bacterial blight resistance and Basmati quality characteristics by phenotypic and molecular marker-assisted selection in rice. **Mol. Breeding** 00: 1–11, 2004

Kaku H. The additive effect of bacterial blight resistance genes *Xa1* and *Xa4* in rice. **Rice Genet. Newsl.** 17: 25-27, 1999

Kaku H. The dosage effect of bacterial blight resistance genes *Xa*-1 and *Xa*-3 in rice. **Rice Genet. Newsl.** 14: 64–67, 1997

Kameswara Rao K, Jena KK and Lakshminarasu M. Molecular tagging of a new bacterial blight resistance gene in rice using RAPD and SSR markers. **International Rice Research Newsletter** 20 : 16–17, 2003

Katiyar SK, Tan Y, Huang B, Chandel G, Xu Y, Zhang Y, Xie Z and Bennett J. Molecular mapping of gene *Gm-6(t)* which confers resistance against four biotypes of Asian rice gall midge in China. **Theor Appl Genet** 103: 953-961, 2001a

Kauffman HE, Reddy APK, Hsieh SPY and Merca SD. An improved technique for evaluating resistance of rice varieties to *Xanthomonas oryzae*. **Plant Disease Rep**. 56: 537-541, 1973

Kelemu S and Leech J. Cloning and characterization of an avirulence gene from Xanthomonas campestris pv oryzae. **Mol Plant-Microbe Interact** 3: 59–65, 1990

Khush GS and Angeles ER. A new gene for resistance to race 6 of bacterial blight in rice, Oryza sativa L. **Rice Genet Newsl** 16: 92-93, 1999

Khush GS and Virmani SS. Breeding rice for disease resistance. *In: Progress in Plant Breeding-I, London* 239-279, 1985

Khush GS, Bacalanglo E and Ogawa T. A new gene for resistance to bacterial blight from O. longstaminata. **Rice Genet News L**7*:* 121–122, 1990

Khush GS, Brar DS, Zapata FJ, Nelson R, McCouch S and Bottrell DG. Biotechnology for rice improvement. In: *Proceedings of the Tenth Australian Plant Breeding*

Conference, April 18-23, Vol. 1. *Focused Plant Improvement· Towards Responsible and Sustainable Agriculture,* 1993

Khush GS, Mackill DJ and Sidhu GS. Breeding rice for resistance to bacterial blight. Bacterial Blight of Rice. *Proceedings of the International Workshop on Bacterial Blight Rice, IRRI, Manila, Philippines*. 207-17, 1989

Khush GS. Origin, dispersal, cultivation and variation of rice. **Plant Mol Biol** 35: 25-34, 1997

Kosawang C, Smitamana P, Toojinda T, Nilpanit N and Sirithunya P. Amplified Fragment Length Polymorphism fingerprinting differentiates genetic diversity of *Xanthomonas oryzae pv. oryzae* from Northern Thailand. **Journal of Phytopathology** 154 (9): 550 – 555, 2006

Kunnel BN. A useful weed put to work: generic analysis of disease resistance in Arabidopsis thaliana. **Trends Genet** 12: 63–8, 1996

Laha GS, Reddy CS, Krishnaveni D, Sundaram RM, Srinivas Prasad M, Ram T, Muralidharan K and Viraktamath BC. Bacterial blight of rice and its management. *DRR Technical Buletine No. 41. Directorate of Rice Research (ICAR), Rajendranagar, Hyderabad*: 1-37, 2009

Lander ES, Green P, Abrahamson J, Barlow A, Daly MG, Lincoln SE and Newburg L. MAPMAKER: an interactive computer package for constructing primary genetic maps of experimental and natural populations. **Genomics** 1: 174–181, 1987

Leach JE, Rhoads ML, Vera Cruz CM, White FF, Mew TW and Leung H. Assessment of DNA element. **Appl. Environ. Microbiol.** 58: 2188-2195, 1992

Lee KS, Angeles ER and Khush GS. Inheritance of resistance to race 6 of bacterial blight in rice. **Rice Genet News L** 17: 73–4, 2001

Lee KS, Rasabandith S, Angeles ER and Khush GS. Inheritance of resistance to bacterial blight in 21 cultivars of rice. **Phytopathology** 93: 147-152, 2003

Lee SY, Ahn JH, Cha YS, Yun DW, Lee MC, Ko JC, Lee KS and Eun MY. Mapping QTLs related to salinity tolerance of rice at the young seedling stage. **Plant Breed.** 126: 43-46, 2007

Li J, Xiao J, Grandillo S, Jiang L, Wan Y, Deng Q, Yuan L and McCouch SR. QTL detection for rice grain quality traits using an interspecific backcross population derived from cultivated Asian (*O. sativa* L.) and African (*O. glaberrima* S.) rice. **Genome** 47: 697–704, 2005

Li ZK, Sanchez A, Angeles E, Singh S, Domingo J, Huang N. and Khush GS. Are the dominant and recessive plant disease resistance genes similar? A case study of rice R genes and Xanthomonas oryzae pv. oryzae races. **Genetics** 159: 757–765, 2001

Lin RM, Zhao WS, Meng XB, Wang M, Peng YL. Rice gene OsNAC19 encodes a novel NAC-domain transcription factor and responds to infection by Magnaporthe grisea. **Plant Sci** 172: 120–130, 2007b

Lou Q, Chen L, Sun Z, Xing Y. Li J, Xu X, Mei H. and Luo L. A major QTL association with cold tolerance at seedling stage in rice *(Oryza sativa*L.). **Euphytica** 158: 87-94, 2007

Mehdy MC, Sharma YK, Sathasivan K and Bays NW. The role of activated oxygen species in plant disease resistance. **Physiol. Plant.** 98: 365-374, 1996

Mew TW, Vera Cruz CM and Medalla ES. Changes in race frequency of *Xanthomonas oryzae pv. oryzae* in response to rice cultivars planted in the Philippines. **Plant Diseases** 76: 1029–1032, 1992

Mew TW. Current status and future prospects of research on bacterial blight of rice. **Annu. Rev. Phytopathol.** 25: 359–382, 1987

Michelmore RW, Paran I and Kasseri RV. Identification of markers linked to disease resistance genes by bulked segregant analysis: a rapid method to detect markers in specific genomic regions using segregating populations. **Proc Natl Acad Sci USA** 88: 9828-9832, 1991

Mohan M, Nair S, Bhagwat A, Krishna TG, Yano M, Bhatia CR and Sasaki T. Genome mapping, molecular markers and marker-assisted selection in crop plants. **Mol Breed** 3: 87-103, 1997a

Mundt CC. Probability of mutation to multiple virulence and durability of resistance gene pyramids. **Phytopathol** 80: 221-223, 1990

Murty VVS and Khush GS. Studies on the inheritance of resistance to bacterial blight in rice varieties. In: Rice breeding. International Rice Research Institute, Los Banos, Philippines, pp 301–305, 1972

Murty VVS, Khush GS and Jensen NF. Inheritance of resistance to bacterial leaf blight, *Xanthomonas oryzae* (Uyeda et Ishiyama) Dowson, in rice. I. Allelic relationships of resistance genes in donor varieties. *Japanese Journal of Breeding* 23: 325-329, 1973

Nair S, Bentur JS, Prasada Rao U and Mohan M. DNA markers tightly linked to a gall midge resistance gene (*Gm2*) are potentially useful for marker-aided selection in rice breeding. **Theor Appl Genet** 91: 68-73, 1995a

Nair S, Kumar A, Srivastava MN and Mohan M. PCR-based DNA markers linked to a gall midge resistance gene, *Gm4t* has potential for marker-aided selection in rice. **Theor Appl Genet** 92: 660-665, 1996

Nakai H. Induced mutations for resistance to bacterial leaf blight in rice. *Institute of Radiation Breeding, National Institute of Agrobiological Resources, Ministry of Agriculture, Forestry and Fisheries, Japan. Gamma Field Symp.* 27: 49-70, 1988

Nakashima K, Tran LSP, Nguyen DV, Fujita M, Maruyama K, Todaka D, Ito Y, Hayashi N, Shinozaki K and Yamaguchi- Shinozaki K. Functional analysis of a NAC-type transcription factor OsNAC6 involved in abiotic and biotic stress-responsive gene expression in rice. **Plant J** 51: 617– 630, 2007

Neeraja CN, Rodriguez RM, Pamplona A, Heuer S, Collard BCY, Septiningsih EM Vergara G, Sanchez D, Xu K and Ismail AM. A marker-assisted backcross approach for developing submergence-tolerant rice cultivars. **Theor Appl Genet** 93: 232-242, 2007

Nelson RJ, Baraoidan MR, Vera Cruz CM, Yap IV, Leach JE, Mew TW and Leung H. Relationship between phylogeny and pathotype for the bacterial blight pathogen of rice. **Appl.Environ. Microbiol**. 60: 3275-3283, 1994

Nilsson-Ehle H. Kreuzungsuntersuchungen an Hafer und Weizen. Lunds Univ.Aarskr. N. F. *5* (2): 1-122, 1909

Nino-Liu DO, Ronald PC and Bogdanove AJ. *Xanthomonas oryzae pathovars*: model pathogens of a model crop. **Molecular Plant Pathology** 7: 303–324, 2006

Ogawa T and Yamamoto T. Inheritance of resistance to bacterial blight in rice. Bacterial Blight of Rice, published by *IRRI, Manila, Philippines*. 471-479, 1986

Ogawa T, Morinaka T, Fujii K and Kinura T. Inheritance of resistance of rice varieties Kogyoku and Java 14 to bacterial group V of *Xanthomonas oryzae*. **Annals of the Phytopathological Society of Javan** 44: 137-141, 1978

Ogawa T, Yamamoto I, Khush GS and Mew TW. Relationship among *Xu-3*, *XA-4* and *Ya-4'* resistant genes to rice bacterial leaf blight. **Jpn. J. Breed**. 37 (Suppl. 1): 176-177, 1987b

Ogawa T. Gene symbols for resistance to bacterial leaf blight. **Rice Genet. Newsl**. 4: 35-37, 1987

Oh SK, Lee S, Yu SH and Choi D. Expression of a novel NAC domain-containing transcription factor (CaNAC1) is preferentially associated with incompatible interactions between chili pepper and pathogens. **Planta** 222: 876–887, 2005

Olufowote JO, Khush GS and Kauffman HE. Inheritance of blight resistance in rice. **Phytopathology** 67: 772-775, 1977

Ou SH. A Handbook of Rice Diseases in the Tropics. Los Baños: International Rice Research Institute, 1973

Paterson AH. Genome Mapping in Plants. Austin, TX: *Landes*. 330, 1996

Petpisit V, Khush GS and Kauffman HE. Inheritance of resistance to bacterial blight in rice. **Crop Sci** 17: 551–4, 1977

Porterer BW, Chittoor JM, Yano M, Sasaki T and White FF. Development and mapping of markers linked to the rice bacterial blight resistance gene Xa7. **Crop Sci.** 43: 1484–1492, 2003

Preece TF, Rhodes ME and Skinner FA. Progression of bacterial disease within plants. *Bacteria and plants, eds Acadamic Press, London*, Pg: 71-83, 1982

Priyadarisini BV and Gnanaminckam SS. Occurrence of a Subpopulation of *Xanthomonas oryzae* pv. *oryzae* with Virulence to Rice Cv. IRBB21 (*Xa21*) in Southern India. **Plant Disease** 83: 781-783, 1999

Ramakrishna W, Chowdari KV, Lagu MD, Gupta VS and Ranjekar PK. DNA fingerprinting to detect genetic variation in rice using hypervariable DNA sequences. **Theor Appl Genet** 90: 1000-1006, 1995

Ramakrishna W, Lagu MD, Gupta VS and Ranjekar PK. DNA fingerprinting in rice using oligonucleotide probes specific for simple repetitive DNA sequences. **Theor Appl Genet** 88: 402-406, 1994

Rao PS and Kauffman HE. A new Indian host of *Xanthomonas oryzae*, incitant of bacterial leaf blight of rice. **Curr. Sci.** 40: 271-272, 1971

Rathour R, Chopra M and Sharma TR. Development and validation of microsatellite markers linked to the rice blast resistance gene Pi-z of Fukunishiki and Zenith. **Euphytica** 163: 275-282, 2008

Reddy APK and Kauffman HE. Multiplication and movement of *Xanthomonas oryzae* in susceptible and resistant hosts. **Plant Dis. Reptr.** 57: 784-787, 1973

Reddy APK and Kauffman HE. Loss of virulence associated with aging of *Xanthomonas oryzae* cultures. **Indian Phytopathol.** 30: 106-111, 1977

Reddy MTS and Reddy APK. Occurrence of pathotypes of *X. campestris pv oryzae* in India. **Indian J Mycol Plant Pathol** 22: 205–6, 1992

Reimers PJ and Leach JE. Race specific resistance of Xanthomonas oryzae pv oryzae conferred by bacterial blight resistance gene Xa-10 in rice (Oryza sativa L) involves accumulation of lignin like substance in host tissues. **Physiol Mol Plant Pathol:** 38:39–55, 1991

Reimers PJ, Guo A and Leach JE. Increased activity of a cationic peroxidase associated with an incompatible interaction between Xanthomonas oryzae pv oryzae and rice (Oryza sativa L). **Plant Physiol** 99: 1044–50, 1992

Ren T, Qu F and Morris TJ. HRT gene function requires interaction between a NAC protein and viral capsid protein to confer resistance to turnip crinkle virus. **Plant Cell** 12: 1917–1925, 2000

Ronald PC, Albano B, Tabien R, Abenes L, Wu K, McCouch SR and Tanksley SD. Genetic and physical mapping of the rice bacterial blight resistance locus *Xa-21*. **Mol. Gen. Genet.** 236: 113-120, 1992

Ruth Ingram and Noltie HJ. Ray Floret Morphology and the Origin of Variability in Senecio cambrensis Rosser, a Recently Established Allopolyploid Species. **New phytologist** 96(4): 601-607, 1984

Saini RS, Goel, RK and Sharma SC. Genetic analysis of resistance to bacterial leaf blight (*Xanthomonas oryzae* pv. *oryzae* Ishiyama) in some rice (*Oryza sativa*L.) lines. **Indian Journal of Genetics and Plant Breeding** 56: 178-181, 1996

Sanchez AC, Brar DS, Huang N, Li Z and Khush GS. Sequence Tagged Site Marker-Assisted Selection for Three Bacterial Blight Resistance Genes in Rice. **Crop Science** 40: 792–797, 2000

Sanchez AC, Hog LL, Yang D, Brar DS, Ausubel F, Khush GS, Yano M, Sasaki T and Huang N. Genetic and physical mapping of Xa-13, a recessive bacterial blight resistance gene in rice. **Theor Appl Genet** 98: 621–32, 1999

Sebastian LS, Ikeda R, Huang N, Imbe T, Coffmann WR and Mc Couch SR. Molecular mapping of resistance to rice tungro spherical virus and green leaf hopper. **The American Phytopathol. Soc.** 86(1): 25, 1996

Shanti ML, George MLC, Vera Cruz CM, Bernando M, Nelson RJ, Leung H, Reddy JN and Sridhar R. Identification of resistance genes effective against rice bacterial blight pathogen. **Plant Disease** 85: 506-512, 2001

Sharma TR, Madhav MS, Singh BK, Shanker P, Jana TK and Dalal V. High- resolution mapping, cloning and molecular characterization of the *Pi-k* (*h*) gene of rice, which confers resistance to *Magnaporthe grisea*. **Mol Genet Genomics** 274: 569– 578, 2005

Sheeba NK, Viraktamath BC, Gangashetti MG and Pawan khera. **International Rice research Notes** 32(1): 25, 2005

Sidhu GS and Khush GS. Dominance reversal of a bacterial blight resistance gene in some rice cultivars. **Phytopathology** 68: 461–463, 1978

Sidhu GS, Khush GS and Mew TW. Genetic analysis of bacterial blight resistance in sevent-four cultivars of rice, *Oryza sativa* L. **Theor Appl Genet** 53: 105-111, 1978

Sidhu GS, Khush GS and Mew TW. Genetic analysis of resistance to bacterial blight in seventy cultivars of rice, Oryza sativa L. from Indonesia. **Crop Improv.** 6: 19-25, 1979

Singh K, Foley RC and Onate-Sanchez L. Transcription factors in plant defense and stress responses. **Curr Opin Plant Biol** 5: 430–6, 2002.

Singh RJ, Khush GS and Mew TW. A new gene for resistance to bacterial blight in rice. **Crop Sci.** 23: 558-560, 1983

Singh S, Sidhu JS, Huang N, Vikal Y, Li Z, Brar DS, Dhaliwal HS and Khush GS. Pyramiding three bacterial blight resistance genes (*xa-5, xa-13 and Xa-21*) using marker-assisted selection into indica rice cultivar PR-106. **Theor Appl Genet** 102: 1011-1015, 2001

Sirisha C, Reddy JN, Mishra D, Das KM, Bernardo MA, Vera Cruz CM, Leung H and Sridhar C. Susceptibility of IRBB 21 carrying the resistance gene *Xa21* to bacterial blight. **Rice Genetics News Letter** 21: 74-75, 2004

Sivamani E, Anuratha CS and Gnanamanickam SS. Toxicity of Pseudomonas fluorescens towards bacterial plant pathogens of banana (Pseudomonas solanacearum) and rice (Xanthomonas campestris pv. oryzae). **Curr.Sci.**56: 547–548, 1987

Song WY, Wang GL, Chen L, Zhai W, Kim HS, Holsten T, Zhu L and Ronald PC. The receptor kinase like protein encoded by the rice disease resistance gene *Xa-21.* **Science** 270: 1804–6, 1995

Souer E, van Houwelingen A, Kloos D, Mol J, and Koes R. The No Apical Meristem gene of petunia is required for pattern formation in embryos and flowers and is expressed at meristem and primordia boundaries. **Cell 85**: 159–170, 1996

Srinivasan B and Gnanamanickam S. Identification of a new source of resistance in wild rice, *Oryza rufipogon* to bacterial blight of rice caused by Indian strains of *Xanthomonas oryzae pv. Oryzae.* **Current Science**. 88 (8): 25-27, 2005

Srivastava DN, Rao YP and Durgapal JC. Can Taichung Native-1 stand up to Bacterial blight ?. **Indian Farming** 16 (2): 15, 1966

Sun X, Cao Y, Yang Z, Xu C, Li X, Wang S, Zhang Q. *Xa26*, a gene confering resistance to *Xanthomonas oryzae pv oryzae* in rice, encodes a LRR receptor-like kinase protein. **Plant Journal** 37: 517-527, 2004

Sundaram RM, Priya MRV, Laha GS, Shobha Rani N, Srinivasa Rao P, Balachandran SM, Ashok Reddy G, Sarma NP and Sonti RV. Introduction of bacterial blight resistance into Triguna, a high yielding, mid-early duration rice variety by molecular marker assisted breeding. **Biotechnology Journal** 4: 400-407, 2009

Sundaram RM, Vishnupriya MR, Biradar SK, Laha GS, Reddy AG, Rani NS, Sarma NP and Sonti RV. Marker assisted introgression of bacterial blight resistance in Samba Mahsuri, an elite indica rice variety. **Euphytica** 160: 411–422, 2008

Suparyono, Sudir and Suprihanto. Pathotype profile of *Xanthomonas* oryzae pv oryzae isolates from the rice ecosystem in Java. **Indonesian Journal of Agricultural Science** 5(2): 63-69, 2004

Tan GX, Ren X, Weng QM, Shi ZY, Zhu LL and He GC. Mapping of a new resistance gene to bacterial blight in rice line introgressed from *Oryza officinalis*. **Yi Chuan Xue Bao**, 31: 724–729 (in Chinese), 2004

Tanksley SD and McCouch SR. Seed banks and molecular maps: unlocking genetic potential from the wild. **Science** 277: 1063-66, 1997

Tanksley SD. Mapping polygenes. **Annu Rev Genet** 27: 205-233, 1993

Tenhaken R, Levine A, Brisson LF, Dixon RA and Lamb C. Function of the oxidative burst in hypersensitive disease resistance. **Proc Natal Acad Sci USA** 92: 4158–4163, 1995

Vera Cruz CM, Ardales EY, Skinner DZ, Talag J, Nelson RJ, Louws FJ, Leung H, Mew TW and Leach JE. Measurement of haplotypic variation in *Xanthomonas oryzae pv. oryzae* within a single field by rep-PCR and RFLP analyses. **Phytopathology** 86: 1352-1359, 1996

Vikal Y, Goel RK, Singh R and Singh K. Molecular characterization of some bacterial blight resistantrice germplasm lines using STS markers linked to *Xa4, xa5, xa13* and *Xa21*. **Plant Disease Research** 19: 25–30, 2004

Wang C, Wen G, Lin X, Liu X and Zhang D. Identification and fine mapping of the new bacterial blight resistance gene, *Xa31*(t), in rice. **Eur J Plant Pathol** 123: 235-240, 2008

Wang GL, Wing RA and Paterson AH. PCR amplification from single seeds, facilitating DNA marker-assisted breeding. **Nucl Acids Res** 21: 25-27, 1993

Wang S, Wang J, Jiang J and Zhang Q. Mapping of centromeric regions on the molecular linkage map of rice (*Oryza sativa* L.) using centromere-associated sequences. **Mol Gen Genet** 263: 165-172, 2000

Xie Q, Frugis G, Colgan D and Chua NH. Arabidopsis NAC1 transduces auxin signal downstream of TIR1 to promote lateral root development. **Genes Dev** 14: 3024–3036, 2000

Xie Q, Sanz-Burgos AP, Guo H, Garcýa JA and Gutie´rrez C. GRAB proteins, novel members of the NAC domain family, isolated by their interaction with a geminivirus protein. **Plant Mol Biol** 39: 647–656, 1999

Yang B, Sugio A and White FF. Os8N3 is a host disease susceptibility gene for bacterial blight of rice. **Proc Natl Acad Sci** 103: 10503–10508, 2006

Yang Z, Sun X, Wang S and Zhang Q. Genetic and physical mapping of a new gene for bacterial blight resistance in rice. **Theoretical and applied genetics** 106-1467-1472, 2003

Yencho GC, Cohen MB and Byrne PF. Applications of tagging and mapping insect resistance loci in plants. **Annu Rev Entomol.** 45: 393-422, 2000

Yoshimura A, Mew TW, Khush GS, Omura T. Inheritance of resistance to bacterial blight in rice cultivar Cas 209. **Phytopathology:** 73:1409–12, 1983

Yoshimura S, Umehera Y, Kurata N, Nagamura Y, Sasaki T, Minobe Y and Iwata N. Identification of a YAC clone carrying the *Xa-1* allele, a bacterial blight resistance gene in rice. **Theor Appl Genet** 93: 117–122, 1996

Yoshimura S, Yamanouchi U, Katayose Y, Toki S, Wang ZX, Kono I, Kurata N, Yano M, Iwata N and Sasaki T. Expression of *Xa1* a bacterial blight-resistance gene in rice is induced by bacterial inoculation. **Proc Natl Acad Sci** 95: 1663-1668, 1998

Yoshimura S, Yoshimura A, Iwata N, McCouch SR, Abenes MN, Baraoidan MR, Mew TW and Nelson RJ. Tagging and combining bacterial blight resistance genes using RAPD and RFLP markers. **Mol Breed**1: 375–87, 1995b

Yoshimura S, Yoshimura A, Nelson RJ, Mew TW and Iwata N. Tagging Xa-1, the bacterial blight resistance gene in rice, by using RAPD markers. **Jpn. J. Breed. 45: 81-85, 1995a**

Zhai W, Lu C, Zhu L, Yang W and Zhang Q. PCR analysis of half-seeds of cereal crops and its application in marker-assisted selection and breeding. **Chin J Biotechnol** 12: 249-255, 1996

Zhang G, Chen L, Xiao G, Xiao Y, Chen X and Zhang S. Bulked segregant analysis to detect QTL related to heat tolerance in rice (*Oryza sativa* L.) using SSR markers. **Agr. Sci. in China** 8, 4: 482-487, 2009

Zhang Q, Lin SC, Zhao BY, Wang CL, Yang WC, Zhou YI, Li DY, Chen CB and Zhu LH. Identification and Tagging a new gene for resistance to bacterial blight (*Xanthomonas oryzae* pv *oryzae*) from *O. rufipogon* **Rice Genet. Newslett** 15: 138-141, 1998

Zhang Y, Wang J, Pan J, Gu Z, Chen X, Jin Y, Liu F, Zhang H and Ma B. Identification and molecular mapping of the rice bacterial blight resistance gene allelic to *Xa7* from an elite restorer line Zhenhui 084. **Eur J Plant Pathol** online version vol 125, 2009b

Zhang Q, Wang C, Zhao K, Zhao Y, Caslana V, Zhu XD and Jiang Q. The effectiveness of advanced rice lines with new resistance gene *Xa23* to rice bacterial blight. **Rice Genet. Newslett**. 18: 71, 2001

Zhang Q, Wang CL, Zhao YL, Jiang QX and Zhu XD. *In International Rice Congress,* 16–20, 2002

Zheng K, Huang N, Bennett J and Khush GS. PCR-based marker assisted selection in rice breeding. IRRI Discussion Paper Series No. 12. International Rice Research, 1995

Zheng K, Subudhi PK, Domingo J, Maopanty G and Huang N. Rapid DNA isolation for marker assisted selection in rice breeding. **Rice Genet Newsl** 12: 255-258, 1995

(29)

quoted in the ref Missing in Ta

quoted in the (5)

text missing in the ref